SCUOLA DI DOTTORATO

UNIVERSITÀ DEGLI STUDI DI MILANO-BICOCCA

Department of

Scienze dell'Ambiente e della Terra (DISAT)

PhD program in **Marine Sciences, Technology and Management** (MTM)

Cycle **XXXVIII**

Advanced Sustainable Materials to Protect and Heal Reefs from Coral Bleaching Events

Surname **Rinaldi** Name **Camilla**

Registration number **815758**

Tutor: **Contardi Marco**

Co-tutor: **Montano Simone**

Supervisor: **Athanassiou Athanassia**

Coordinator: **Galli Paolo**

ACADEMIC YEAR 2024/2025

Table of Contents

Abstract

Climate change, particularly the rise in sea surface temperatures, is causing severe degradation of coral reefs. One of the main threats to reef ecosystems worldwide is coral bleaching, primarily driven by oxidative stress and excessive production of reactive oxygen species (ROS). In recent decades, thermal stress events have increased in both frequency and intensity, resulting in increasingly severe bleaching episodes. This process disrupts the symbiosis between corals and their resident microscopic algae, the zooxanthellae, activating several intracellular molecular cascades that can ultimately lead to coral mortality. Following the alarming outcomes of the fourth global bleaching event reported by NOAA in 2024 and the projected loss of 70–90% of coral reefs worldwide by mid-century, there is an urgent need for active therapeutic interventions to mitigate coral bleaching.

The main goal of this PhD research was to develop an efficient, eco-friendly, and biodegradable drug delivery system capable of providing controlled and sustained release of natural antioxidant compounds to scavenge ROS produced during heat stress events.

In the first part of the work, curcumin was selected as the antioxidant candidate, and two different materials were developed and tested: an underwater three-layered film system and protein-based microparticles for coral application.

Bio-based polymers derived from marine sources and green fabrication techniques were utilized to obtain the desired multilayered film, engineered to enable the tunable, continuous, and directional release of curcumin through a curcumin–β–cyclodextrin complex nanocarrier. Morphological, chemical, and mechanical analyses confirmed its structural integrity, water absorption capacity, and hydrogel-like behavior - key features for underwater applications.

Similarly, curcumin-loaded silk-based microparticles (cur-silk MPs) were developed to mitigate thermal stress and enhance coral resilience. The MPs' morphology, physicochemical properties, release kinetics, and compatibility with corals were thoroughly evaluated. Ingestion studies using *Heliofungia fralinae* confirmed that MPs enter the gastric cavity and release curcumin locally.

After the complete characterization of both systems, the second part of the PhD focused on *in vivo* testing on *Stylophora pistillata* corals under a four-phase bleaching simulation experiment conducted at the Genoa Aquarium. Coral nubbins were exposed to 31 °C for one week to induce oxidative stress, and both materials were applied to evaluate their efficacy in enhancing coral thermal tolerance.

Without requiring direct contact, the film system effectively mitigated oxidative stress, as evidenced by higher chlorophyll content, greater Symbiodiniaceae density, and reduced lipid peroxidation in treated corals compared to controls. The film's gradual degradation supported sustained curcumin release without adverse effects on coral health.

Similarly, corals treated with cur-silk MPs showed significantly higher chlorophyll content and Symbiodiniaceae density than untreated controls, indicating improved stress tolerance.

These results highlight the potential of both materials as novel, biocompatible, and sustainable therapeutic platforms to enhance coral resilience against thermal stress. Their versatility and ease of application make them promising candidates for scalable use in both controlled aquaria and natural reef environments, offering a valuable strategy to mitigate coral bleaching.

In the third part of the PhD, conducted during a six-month research period at the Scripps Institution of Oceanography, the two previously developed systems were combined into a single integrated drug delivery platform. Using a scalable 3D bioprinting technique, new natural antioxidant compounds and biopolymers were used to encapsulate microparticles directly within

a hydrogel-like matrix, achieving a higher level of controlled release. Together with the microparticles, *Breviolum psygmophilum* symbiodiniaceae algae were also encapsulated within the hydrogel scaffold to mimic the internal structure of coral–algae symbiosis. The system was characterized and successfully tested *in vivo* for its ability to prevent oxidative stress.

This final therapeutic system not only represents the culmination of this PhD project but also provides valuable insights for post-bleaching treatments, offering a promising technological approach to support global coral conservation strategies.

Chapter 1: Introduction

1.1 Coral Reef Ecosystems Under Environmental Changes

Coral reefs are among the most productive and biologically diverse ecosystems on Earth, providing habitat for a vast array of marine organisms [1–3]. In addition to their ecological role, they deliver critical ecosystem services, including fisheries, coastal protection, and tourism, that support millions of people globally, with an estimated total economic value exceeding US$10 trillion [4,5].

From a geological perspective, coral reefs can be considered biogenic structures, formed over millions of years by the accumulation of calcium carbonate secreted by the coral skeleton through the process of calcification [6].

Reef-building corals sustain this process through a long-standing mutualistic relationship with photosynthetic dinoflagellates of the family Symbiodiniaceae – commonly referred to as zooxanthellae – that live as endosymbionts within the tissues of coral polyps, providing most of the coral's energy [7]. Algae benefit from a protected habitat, access to inorganic nutrients, and a continuous supply of carbon dioxide, while the corals – besides the enhancement of the calcification process – receive photosynthetically derived organic compounds and improved waste removal [8]. Because this symbiosis depends on light, coral reefs are confined to the euphotic zone - the uppermost layer of the ocean where water clarity ensures sufficient light for algal photosynthesis - and thrive in regions where seawater temperatures range between 23 and 29°C, such as tropical and subtropical ones. Given these strict environmental requirements, coral reefs are extraordinarily sensitive to changes in their surroundings. Indeed, being subjected to multiple natural, human-induced, and human-mediated stressors, these ecosystems are increasingly threatened and experiencing a serious decline [9,10]. The causes of this deterioration lie in a broad spectrum of human activities such as overfishing, coastal development, and mass

tourism, exacerbated by large-scale environmental changes such as shifts in temperature, sea level, and pH [11–13].

Stressors acting on coral reefs may be broadly categorized as “global threats” – climatic or large-scale environmental phenomena beyond the control of local management, and “local threats” – referring to direct human impacts that can, in principle, be regulated or mitigated. Currently, around 75% of the world’s reefs are considered threatened when local stressors are coupled with global ones, and this proportion continues to rise [13]. While predicting the overall impacts of climate change on marine ecosystems remains challenging, there is strong evidence that rising temperatures directly trigger coral bleaching and facilitate disease outbreaks [14,15].

Understanding the factors influencing this decline is therefore crucial for the conservation and management of these vital ecosystems.

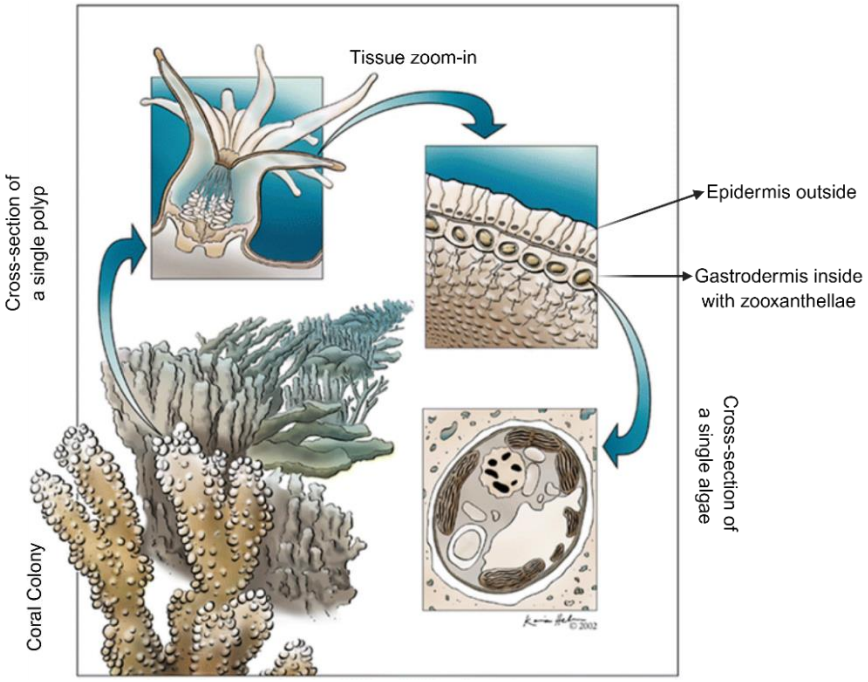

Figure 1.1 Graphic description of coral polyp – zooxanthellae symbiosis. (Figure adapted from *Muller Parker et al. 2015* [8]).

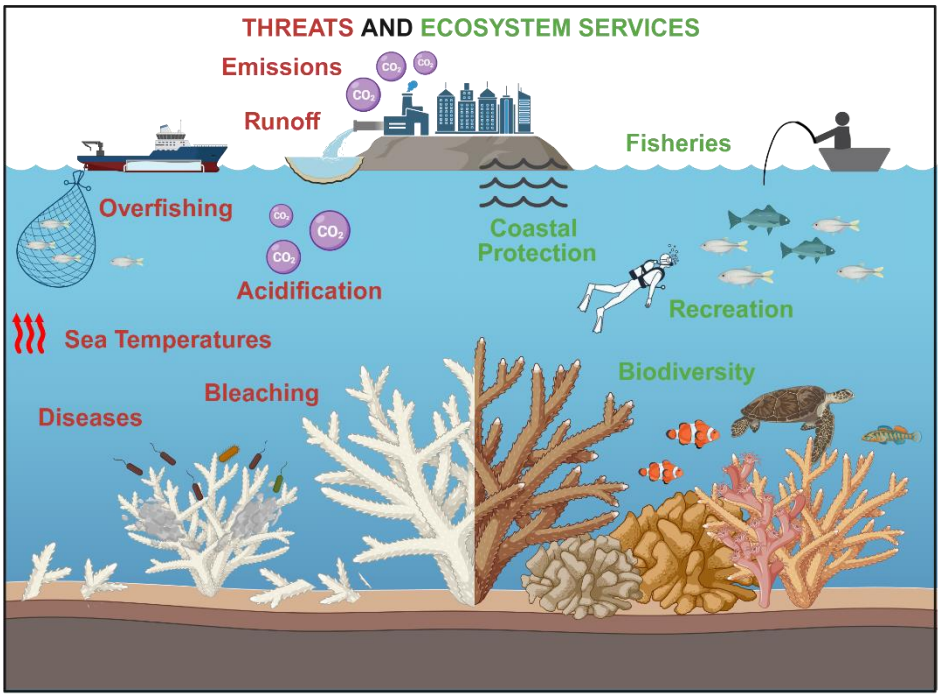

Figure 1.2 Schematic representation of major threats to coral reef ecosystems and main ecosystem services provided by these habitats. (Figure adapted from *Comte & Pendleton 2018* [16])

1.2 Causes and Description of Coral Bleaching Events

Human activities have led to a rapid increase in greenhouse gas concentrations in the atmosphere, resulting in elevated air and seawater temperatures. As a result, thermal or light stress can damage the photosynthetic system of zooxanthellae, potentially disrupting the symbiotic relationship between reef-building corals and their Symbiodiniaceae algae [17,18]. When this occurs, the symbionts may be expelled or die, causing the coral to lose its characteristic yellow-brown pigmentation and turn white, typical of coral bleaching phenomena [19,20].

Although corals can feed heterotrophically on small prey, ranging from bacteria to mesozooplankton (0.5 μm – 2 mm), while waiting to regain zooxanthellae under favorable conditions, they cannot survive for prolonged periods without their symbionts. Delayed recovery, therefore, poses a significant risk of coral mortality [21].

Coral bleaching results from a set of complex processes that can be initiated by numerous independent triggers, which can be divided into "physical condition" – such as heat or light – and "biogeochemical conditions" – such as hypoxia, nitrogen enrichment, or bacterial infections [22–24]. Even if heat is widely recognized as the primary trigger of bleaching events globally, naturally occurring bleaching is often the result of a combination of stresses from multiple triggers. For example, the most severe bleaching events typically occur when water temperatures are elevated on days with clear water and minimal cloud coverage, resulting in a co-occurrence of light stress and high heat [25]. Prolonged exposure to stressors such as elevated temperatures and UV radiation can activate various biomolecular cascades within the coral cell, ultimately leading to symbiosis breakdown. Coral bleaching is one of the most studied yet debated phenomena affecting reefs, with multiple hypotheses proposed to explain its underlying mechanisms [24]. Among these, the oxidative stress and carbon limitations hypotheses, as well as an integration and overlapping of

these two, are the most widely supported explanations [24,26,27]. Specifically, according to the oxidative theory of coral bleaching, reactive oxygen and nitrogen species (ROS and RNS) are overproduced through the activity of the damaged photosynthetic system in the symbionts under heat and light stress [22,26,28]. ROS and RNS are reactive molecules that, in normal conditions, are scavenged through the cells' antioxidant systems - such as catalase (CAT), superoxide reductase (SOD), glutathione enzymes - but that can be over-accumulated during stressful situations when these antioxidant capacities are overwhelmed. In the absence of sufficient degradation, ROS and RNS can leak into the host cell, damaging cellular components such as DNA, proteins, and lipids, triggering stress and/or immune response, ultimately resulting in coral dysbiosis and bleaching [28]. No hypotheses can account for all occurrences of bleaching, but what is clear is that continued exposure to stressful conditions can also impair coral immunity and increase pathogen virulence, linking bleaching events and disease outbreaks. Estimates indicate that mass bleaching events and coral diseases have already decimated 20% of the world's coral reefs, with 24% facing imminent collapse and another 26% being at serious risk of irreparable damage [10]. Notably, these figures do not account for the catastrophic impacts of the most recent Fourth Global Coral Bleaching Event, officially confirmed by the National Oceanic and Atmospheric Administration (NOAA) and International Coral Reef Initiative (ICRI) on April 25^{th,} 2024, suggesting that the current threat to coral reef ecosystems may be even more severe than previously estimated [29,30]. Considering the intensity of coral bleaching events, even under the most optimistic scenario of a 1.5°C rise in global temperatures, a loss of 70-90% of coral reefs worldwide is expected by mid-century. As the frequency and severity of mass bleaching events continue to rise with ongoing ocean warming, coral bleaching has become a pressing concern [31,32]. This urgency has intensified research efforts aimed at unraveling the underlying

mechanisms of bleaching and developing rapid, effective strategies for mitigation and reef conservation.

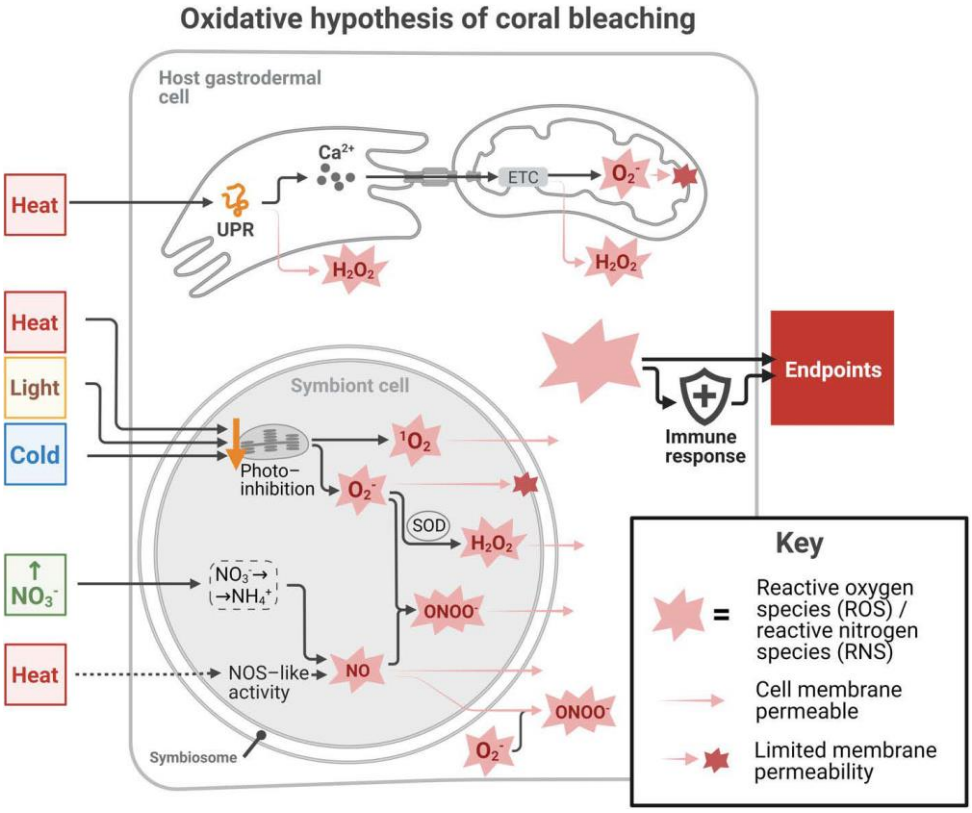

Figure 1.3 Overview of the oxidative hypothesis of coral bleaching, indicating the principal triggers addressed by this hypothesis and their downstream effects on pathway cascades in both the host gastrodermal and algal symbiont cells. (Figure adapted from *Helgoe et al. 2024* [24]).

1.3 Coral Bleaching Mitigation Strategies: State of The Art

A wide range of actions has been implemented worldwide to tackle and mitigate coral reef degradation, spanning from governance measures and the reduction of local stressors to active restoration efforts. One preventive approach is the marine cloud brightening (MCB) technique, a geoengineering technology that seeks to enhance the reflectivity (albedo) of low-lying, ice-free marine stratocumulus clouds by seeding them with fine particles, thereby cooling ocean surface temperatures in coral reef regions [33].

A more post-bleaching intervention, instead, is the coral reef restoration, defined as the active process of assisting the recovery of ecosystems that have been degraded, damaged, or destroyed [34,35], representing a key strategy to combat dramatic coral cover declines worldwide [36]. Coral restoration techniques include nurseries, spider frames, Biorock®, and 3D-printed structures that allow corals to be out-planted into natural environments, with encouraging results in repopulating damaged reef areas [37–40]. Nevertheless, both preventive and restorative approaches remain largely passive, offering limited capacity to address the increasing frequency and severity of bleaching events. To overcome this limitation, human-assisted biological solutions have been developed. These include selective breeding to enhance coral genetic resilience and manipulation of the microbiome. In particular, the isolation and reintroduction of beneficial microorganisms – known as Beneficial Microorganisms for Coral (BMCs) – are being tested as environmental probiotics capable of improving coral resistance during marine heat waves [41]. Although experimental outcomes have been promising, demonstrating that microbial-based therapies can restore coral health, large-scale and long-term application remains challenging due to high costs, the need for specialized personnel, and uncertainties regarding broader impacts on local microbial communities. Finally, the administration of trace elements, such as manganese, has

shown beneficial effects on coral physiology, increasing overall thermal tolerance and offering an additional avenue of mitigation [42,43].

1.4 Use of Antioxidant Compounds in Coral Bleaching Treatment: The Importance of an Effective Drug Delivery System

In pharmaceutical research, drug delivery systems have been developed to ensure controlled and sustained release of therapeutic agents into a specific target [44]. Inspired by this approach, underwater drug delivery systems have been designed to treat coral bleaching, and they are emerging as a new, effective underwater therapy. Administering drugs at a specific rate, ensuring a slow and targeted delivery of the compound, represents one of the main advantages of these therapeutic approaches.

However, the marine environment poses unique challenges: being vast and dynamic, it requires delivery methods that are both highly controlled and environmentally compatible, ensuring the active compound reaches the target site without dispersing into the surroundings.

Recent advances in material science, pharmaceutics, and micro/nanotechnologies have introduced novel approaches for controlled drug delivery in the marine environment. Moreover, antioxidant molecules are gaining attention as a potential therapy for coral bleaching, owing to their ability to neutralize harmful reactive oxygen species within coral tissues.

Two pioneering studies exemplify this emerging strategy. Roger *et al.* [45] administered antioxidant nanoceria particles to free-living Symbiodiniaceae algae – commonly found in corals and anemones - and demonstrated their effectiveness in reducing oxidative stress in anemones.

Subsequently, Contardi *et al*. [46] developed a prototype of underwater material for the release of antioxidants directly into corals, showing that curcumin-loaded hydrogel films helped prevent bleaching in *Stylophora pistillata* corals.

However, nanoceria have not yet been tested in corals, and a significant portion of the curcumin in the hydrogel system was lost to dispersion and remained unused. These outcomes highlight the need to enhance material performance, optimize drug delivery efficiency, and investigate specific molecular targets of bleaching within corals to better understand the mechanisms of action of antioxidant therapies.

1.5 Aims of the study

To advance the development of effective therapies for coral bleaching, it is essential to move beyond current approaches, primarily *in vitro* or passive diffusion, and toward targeted technologies capable of delivering therapeutic agents directly to corals. Therefore, this study aims to design and validate an innovative drug delivery system specifically tailored for application in coral reef environments.

The system was developed to be as eco-friendly as possible, adopting a circular-economy approach and relying on natural, biobased, and predominantly marine-derived materials to guarantee environmental compatibility.

Its therapeutic potential lies in the encapsulation of natural antioxidant compounds, chosen for their ability to scavenge reactive oxygen species and mitigate oxidative stress, one of the main drivers of coral bleaching.

Moreover, by exploiting the intrinsic properties of the used biopolymers, the system was engineered to ensure a continuous and prolonged release of the drug, possibly achieving different

levels of control over the delivery process. In this way, the therapeutic action can be sustained throughout the treatment period and directed precisely to the coral tissue.

A further objective was to design a technology that is effective and practical: the use of low-cost materials and simple fabrication techniques makes the system easy to develop, scalable, and suitable for large-scale application in real reef environments. All the materials were tested *in vivo* to validate their efficacy in mitigating bleaching events and to assess their potential for wider use in reef conservation strategies.

Finally, this work is aligned with the United Nations 2030 Agenda for Sustainable Development, as it contributes simultaneously to the protection of marine ecosystems (SDG 14: Life Below Water), the safeguarding of water quality (SDG 6: Clean Water and Sanitation), and the promotion of sustainable and renewable material use (SDG 12: Responsible Consumption and Production).

Chapter 2: Underwater Antioxidant Film System

2.1 Directional and Tunable Underwater Release of Curcumin Through a Three-layered Film System to Enhance Thermal Stress Resistance in Corals

Although treatment of corals with natural antioxidant compounds is one of the most promising strategies for first-aid therapy in combating heat wave events nowadays, few studies have focused on antioxidant-based approaches. A novel three-layered, free-standing film system designed for underwater, directional, and sustained release of curcumin is presented here to address this gap. The ultimate application of this system is in real marine environments, specifically in aquaria and open ocean field settings for coral treatment. This requires the use of natural compounds and materials, as well as environmentally friendly fabrication techniques. To address this, among the several drugs available in nature, curcumin - a natural antioxidant well-known for its anti-inflammatory and antioxidant properties [47,48]- derived from the *Curcuma longa* plant, was selected. Green solvents (water, ethanol, and DMSO), diverse techniques, and different biobased polymers were involved in the fabrication of this system, which resulted in a very versatile material. Based on the literature, an underwater film configuration was chosen as optimal to achieve the desired properties [49,50], allowing both direct application onto the coral skeleton or placement near the organisms. This ensures sustained curcumin release over time, thereby enhancing heat resistance. Each layer was specifically engineered to perform a distinct function by playing with the polymeric composition: a carrageenan-pectin monolayer for initial burst release, a chitosan-based second layer as a drug reservoir enabling slower release, and an outer zein protein shield for unidirectional delivery. These natural, biodegradable polymers – sourced respectively from seaweed [51], citrus peel [52], crab shells [53], and maize [54] – ensure

biocompatibility alongside tunable release of the drug. Due to curcumin's low solubility in water, it was encapsulated in 2-hydroxypropyl β-cyclodextrins – cyclic oligosaccharides derived from starch with a hydrophobic cavity and hydrophilic exterior – forming a complexed nanocarrier (cur-βCD) [55–57]. This nanocarrier was integrated into the first two layers to promote uniform dispersion of curcumin during the release. The material was extensively characterized in terms of its physicochemical properties, release kinetics, water resistance, and coral biocompatibility. Its efficacy was tested in a 30-day thermal bleaching model using *in vivo* and *in vitro* assays. Results demonstrated that cur-βCD-loaded system significantly mitigated bleaching effects, preserving coral morphology, chlorophyll content, Symbiodiniaceae density, and reducing oxidative stress markers such as Superoxide Dismutase (SOD), Glutathione Reductase (GR), Glutathione S-transferase (GST), Catalase (CAT), and Lipid Peroxidation (LPO). Overall, the system offers a promising, biodegradable antioxidant platform for enhancing coral resilience to thermal stress, which can be applied underwater in real-world scenarios on different infrastructures for restoration (nurseries, reefs, etc.) and as a free-standing material in aquaria, contributing to global coral conservation strategies.

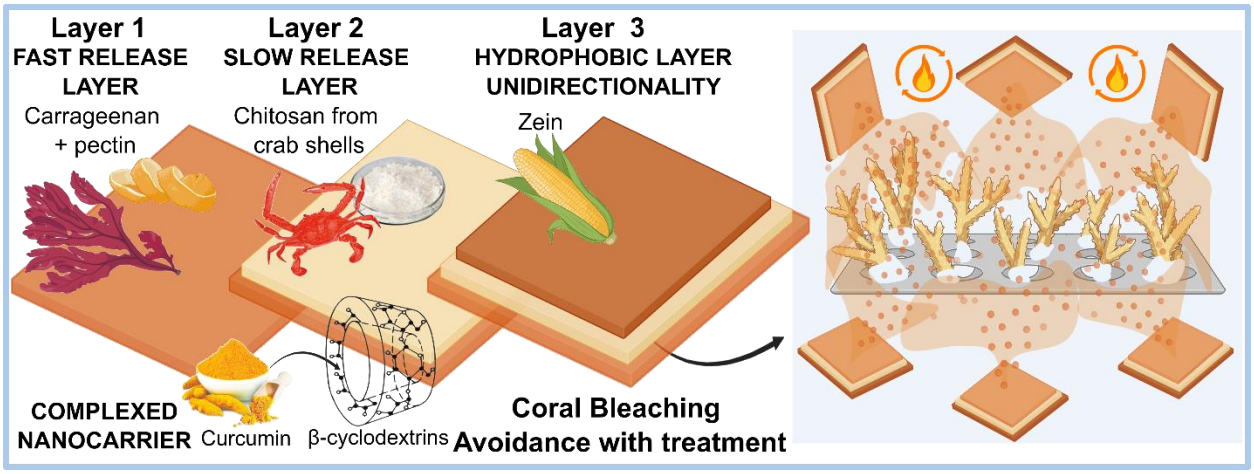

Figure 2.1 Schematic representation of three-layer film system composition and final application in coral bleaching treatment.

2.2 Materials and Methods

2.2.1 Materials

Pectin from citrus peel (galacturonic acid ≥ 74.0%) (dried basis), carrageenan, polyvinylpyrrolidone (PVP) (M_W = ~1,300,000 kDa), curcumin from *Curcuma longa* (turmeric) powder (Mw = 368,38 g/mol), (2-Hydroxypropyl)-β-cyclodextrin (Mw = ~1,460 Da), chitosan from crab shells (Mw = 600 kDa), Zein powder (average M_W = 20 kDa), ethanol, dimethyl sulfoxide (99,9%) and acetic acid (≥ 99.8%) were purchased from Sigma-Aldrich. Polyglycerine-6 was provided by SPIGA-NORD.

2.2.2 Preparation of Films

To prepare layer 1, 288 mg of polyglycerine-6 (~10% w/w with respect to the total weight of pectin, carrageenan, and PVP) was dissolved in 56 mL of MilliQ water under stirring on a 60°C hot plate for 10 minutes. 140 mg of pectin powder was added to the glycerin solution and stirred for another 10 minutes at 60°C. Decreasing the temperature to 50°C, 2660 mg of carrageenan and 200 mg of PVP were added to the solution under stirring for no more than 2 hours.

Meanwhile, a 5 mL ethanol solution with a 1:2 w/w ratio of curcumin and (2-Hydroxypropyl)-β-cyclodextrin powders (175 mg of curcumin – 350 mg of βCD) was prepared and added to the original solution. After 2 hours, the solution was poured into 12 x 12 cm square plastic Petri dishes covered with PDMS and kept in the dark under an aspirated hood (20-23°C, 40-44% R.H.) overnight to eliminate solvents.

For layer 2 preparation, 525 mg of chitosan and PVP were dissolved in 35 mL of an acidic aqueous solution (4% v/v acetic acid) and left under stirring at 70°C overnight (16 hours). Meanwhile, a 5 mL ethanol solution with a 1:2 w/w ratio of curcumin (2-Hydroxypropyl)-β-cyclodextrin powders (175 mg of curcumin – 350 mg of βCD) was prepared and added to the original solution. At least 35 mL of layer 2 solution was poured onto a well-dried layer 1 by using a Rod-coater system (model EZ coater EC-200; ChemInstruments) and left to dry overnight under the hood at room temperature to eliminate solvents. Considering the total amount of solutions used to obtain the complete bilayer (56 mL from layer 1 and ~35 mL from layer 2), it can be assumed that each bilayer has a total amount of curcumin of ~ 320 mg.

For layer 3, 250 mg of Zein was dissolved first in 400 µL of DMSO, and then 2.3 mL of methanol and water were added to this solution and left under stirring for 1-2 hours. A 5% w/v zein solution was sprayed onto the bilayer system under a chemical hood using a dual-action commercial airbrush (Mecafer) supplied with compressed air at a pressure of 2 bar [58,59]. 10 mL of solution was deposited at a substrate-nozzle distance of 5 cm, flow rate of 1mL/min. For clarity, layer 1 is here called “monolayer”, layer 1 + layer 2 is referred to as “bilayer system”, and layer 1 + layer 2 + layer 3 as “three-layer system”.

2.2.3 Scanning electron microscopy and energy-dispersive X-ray Spectroscopy

The morphology of the obtained films was analyzed by Scanning Electron Microscopy (SEM), using a variable pressure JOEL JSM-649LA (JEOL, Tokyo, Japan) microscope equipped with a tungsten thermionic electron source and working in high vacuum mode, with an acceleration voltage of 5 kV. The specimens were coated with a 10 nm thick film of gold utilizing a Cressington Sputter Coater – 208 HR (Cressington, Watford, UK).

Parallelly, to better highlight the differences between layer 1 and layer 2 in the bilayer, SEM-EDS (Scanning Electron Microscopy with Energy Dispersive X-ray Spectroscopy) analysis was performed. Measurements were conducted separately for layer 1 and layer 2, as well as for the bilayer. To maintain the integrity of the system and ensure a good quality of results, the ethanol-water dehydration treatment was followed before the fixation of the material.

2.2.4 Curcumin - (2-Hydroxypropyl)-β-cyclodextrin Complexation

To confirm the inclusion of curcumin within the 2-Hydroxypropyl-β-cyclodextrin hydrophobic cavity, solutions of ethanol with a 1:2 w/w ratio of curcumin and βCD and ethanol with just curcumin inside were left under stirring overnight. 1 mL of both solutions was added to an aqueous solution, and absorbance was measured with a Varian Cary 6000i Scan UV-visible spectrophotometer (Walnut Creek, California, USA).

2.2.5 Attenuated Total Reflection-Fourier Transform Infrared (ATR-FTIR) Spectroscopy

Infrared spectra of the different layers of the system were acquired by using an ATR accessory (MIRacle ATR, PIKE Technologies) with a diamond crystal coupled to an FTIR spectrometer (Vertex 70v FTIR, Bruker). All spectra were recorded between 4000 and 600 cm^{-1}, with a resolution of 4 cm^{-1}, accumulating 64 scans. ATR-FTIR measurements were collected for

monolayer, bilayer, and three-layer samples on both sides to better appreciate the successful overlap of each layer onto the other.

2.2.6 Mechanical Properties

The mechanical properties of the different systems were determined by uniaxial tension tests on a dual-column universal testing machine Instron 3365 (Instron, Norwood, Massachusetts, USA). Films were cut into dog bone specimens (n = 10) with a width of 4 mm and an adequate length of 25 mm. Displacement was applied at a rate of 10 mm min^{-1}. Young's modulus, tensile stress at maximum load, and elongation at break were calculated from the stress-strain curves for the monolayer, bilayer, and three-layer. Before mechanical testing, dog-bone specimens were conditioned for 24 hours at 24 °C and 44% relative humidity (RH) in an Espec SH-262 environmental chamber.

2.2.7 Rheological Tests

An Anton Paar Modular Compact Rheometer (MCR 302) was used to measure rheological properties. Viscoelastic measurements were conducted on hydrated films using stress-controlled Rheometers equipped with a 40 mm PEEK plate, at a temperature of 28 ± 0.1 °C. Prior to analysis, a 5 mm diameter disk of monolayer, bilayer, and three-layer systems was immersed in salty water for 3 hours, then placed onto the rheometer plate. Tests were then repeated on samples immersed in salty water for 24 hours to evaluate the behavior of biofilms as hydrogels.

Amplitude sweep tests were conducted to determine the Linear Viscoelastic Region of each sample using a shear strain range from 10^{-4} to 1 at an angular frequency of 10 rad/s. Subsequently, frequency sweep tests were performed on each sample within an angular frequency range of 0.1 to 1 rad/s, at a fixed shear strain of 10^{-3}.

2.2.8 Swelling Properties

The films' aqueous liquid absorption and erosion behaviors were evaluated by placing a 1 x 1 cm square of the samples (n = 5) in 12 mL of MilliQ water as well as salty water to mimic the underwater condition in terms of pH, salts, and composition. Samples were weighed at time zero and after 20 minutes, 40 minutes, 60 minutes, 2, 4, 6, and 24 hours, and the excess water was removed by placing the samples on filter paper. The swelling degree (SD, %) was calculated by using eq 1:

$$SD(\%) = \frac{(Wt - Wi)}{Wi} x100$$

where Wt corresponds to the weight of the swollen sample at time t and Wi is the initial dry weight. Measurements were performed in triplicate.

2.2.9 Gel Fraction Properties

To evaluate the level of cross-linking, samples resulting from the swelling test (n = 5, 24 hours immersed in seawater) were dried under the hood overnight and weighed the day after. The percentage of gel fraction was calculated by using eq 2:

$$GF(\%) = \frac{Wi}{Wf} x100$$

Where Wi is the initial dry weight and Wf is the final one after being dried overnight. Measurements were performed in triplicate.

2.2.10 Drug Release Studies

The curcumin-βCD complexed nanocarrier release from each system was measured using a Varian Cary 6000i Scan UV–Visible spectrophotometer (Walnut Creek, California, USA). Curcumin in both MilliQ and Salty water has a characteristic UV absorbance peak at 426 nm. A curcumin

calibration curve was constructed using both MilliQ and salty water to extrapolate the molar extinction coefficient, leading to $\varepsilon = 1800\ cm^{-1}\ M^{-1}$. At time zero, t = 0 s, square samples of 1 × 1 cm were placed on the top part of a 6.5 mm Transwell with 8.0 μm pore polycarbonate membrane insert, TC-treated, w/lid, sterile, 48/cs immersed in 4 mL of salty water. Measurements were performed at specific time intervals. 2.5 mL of solution was taken out and replaced with the same amount of fresh medium at each time point (20 min, 40 min, 1h, 2h, 4h, 6h, 8h, 24h, 32h, 48h, 56h, 120h, 128h, 144h, 152h, 168h, 176h). All measurements were taken so that sinking conditions were maintained, and the validity of the Beer-Lambert law was reassured. The experiments were carried out in triplicate, and the data were expressed as a cumulative percentage. The entire Transwell Petri was sealed with Parafilm tape to avoid water evaporation.

2.2.11 Unidirectionality Drug Release Studies

A unidirectional drug release study was performed to verify the capacity of the complete three-layered film system to provide a good unidirectionality of cur-βCD toward the direction of the corals. Transwells were used to mimic the condition. The transwell structures were filled with 6.0 mm film disks, and 0.25 mL of salty water was then added. After this, the transwell was placed inside another well, firstly filled with 1.00 mL of salty water. The bottom part simulated the environment, while the top part simulated the coral's skeleton. The cur-βCD release from the system was measured using a Varian Cary 6000i Scan UV–Visible spectrophotometer (Walnut Creek, California, USA). Each volume from the two different compartments was collected at each time point (20 min, 40 min, 1h, 2h, 4h, 6h, 8h, 24h, 32h, 48h, 56h, 120h, 128h, 144h, 152h, 168h, 176h) and diluted to the total volume of 2.5 mL. The absorption peak at 426 nm was used to control the diffusion of curcumin. The experiments were carried out in triplicate.

2.2.12 ABTS Free Radical Cation Scavenging Assay

An ABTS (2,2′-azino-bis(3-ethylbenzothiazoline-6-sulfonic acid)) free radical cation scavenging assay was performed as described in Fadda *et al*. [60]. ABTS radical cation (ABTS·+) was generated by the reaction between 7 mM ABTS water solution with 2.45 mM potassium persulfate solution in the dark at room temperature for 12–16 h. The ABTS·+ solution was diluted with water to obtain an absorbance of 0.80 a.u. at 734 nm. After that, 1x1 cm squares of each layer were cut and added to 3 mL of diluted ABTS·+ solution. The decrease in absorbance was determined at 734 nm with a Varian Cary 6000i Scan UV–visible spectrophotometer (Walnut Creek, California, USA) at different times. All measurements were carried out in triplicate, and the results were averaged to obtain a mean value. Radical scavenging activity (RSA) was expressed as the inhibition percentage of free radicals of the sample and calculated by using eq 3:

$$radical\ scavenging\ activity\ (\%) = \frac{A0 - A1}{A0} x100$$

where A0 is the absorbance value of the control radical cation solution and A1 is the absorbance value of the sample at different time points.

2.2.13 Biochemical Oxygen Demand

Biochemical oxygen demand (BOD) was performed to evaluate the biodegradability of the samples. Samples were cut into small pieces, and according to their composition, about 25 mg of material was added to 432 mL of seawater. Since BOD operates on the principle that microorganisms consume oxygen while decomposing organic substances present within the water, seawater collected from Old Harbor (Porto Antico) of Genoa was chosen as a liquid medium. Microbial consortia and saline nutrients required for their establishment were already present, mimicking authentic natural circumstances. The experiment was conducted at room temperature

to encourage microbial decomposition within amber glass bottles with a volume of 510 mL, hermetically closed with the OxiTop® measuring heads. Sodium hydroxide tablets were added as a CO_2 scavenger to sequester carbon dioxide produced during biodegradation. Biotic consumption of the oxygen present in the free volume of the system was measured as a function of the decrease in pressure.

Samples were tested in triplicate. After 30 days, raw oxygen consumption data (mg O_2/L) were corrected by subtracting the mean values of the blanks obtained by measuring the seawater's oxygen consumption without any test material. After this subtraction, values were normalized on the mass of the individual samples and referred to 100 mg of material (mg O_2/100 mg material). The BOD is calculated as the difference between the initial and final dissolved oxygen concentrations expressed as milligrams of oxygen per liter (mg/L) of water. Finally, the means of the triplicates were calculated and plotted vs time.

2.2.14 Film application on corals

Following the experiment by Santoro *et al.* [41], a new coral bleaching setup was developed to evaluate the efficacy of the complete three-layered film system in enhancing coral tolerance to heat stress. The coral bleaching model was divided into four distinct phases: acclimation (A), heat stress (HS) (where the temperature was increased by 0.5°C daily), bleaching (B) (corals were maintained at 31°C for one week), and recovery (R) (temperature was gradually reduced by 1°C daily until reaching the original 25°C). Physicochemical parameters were continuously monitored and controlled, while water temperature was precisely adjusted using a 500W Aquamedic heater equipped with an external thermostat, maintaining a variation within ±0.1°C**.** A total of 24 coral fragments were acclimated and distributed between two tanks (12 fragments per tank) and the two experimental groups (untreated control group n = 12; film-treated group n = 12). The entire

experiment was conducted using a water bath setup, where twenty-liter coral tanks were placed inside a larger 500-liter tank under a 13-hour light and 11-hour dark cycle at 250 PAR. Each small tank was aerated individually, and a 40% water change was performed three times per week.

In one tank, coral fragments were surrounded by ~5 x 5 cm pieces of a three-layer substrate while the control tank received no treatment. As mentioned above, each bilayer comprises 350 mg of curcumin distributed in 144 cm^2 of area. Assuming that the drug was homogeneously distributed within the system, each 5x5 cm cut piece with a total area of 25 cm^2 had a quantity of curcumin equal to ~70 mg. After the acclimation phase, during which corals were kept at 25°C, the temperature increased by 0.5°C per day until reaching a maximum of 31°C. The corals were then maintained at this temperature for a week before entering the recovery phase, where the temperature gradually decreased. To prevent excessive algal growth, water changes were performed every two days. Change of film pieces was conducted once every two weeks since their integrity was tough. Finally, at the end of each phase, three coral fragments, both from the treated and untreated groups, were collected for molecular analyses. The experiment was designed to induce thermal stress in corals strong enough to observe potential molecular differences between corals treated with the three-layered film system and untreated controls without causing mortality. To prevent complete bleaching, the temperature was reduced after seven days of exposure to 31 °C (bleaching phase), initiating the recovery phase.

Molecular Analysis

2.2.15 Quantification of Chlorophyll *a* and *c2*

Coral tissue was extracted from frozen fragments using a 1000 µL pipette tip connected to a benchtop air pressure valve via a rubber hose, delivering airflow in combination with 5 mL of ice-cold phosphate-buffered saline (PBS) [61]. The resulting tissue slurry was then homogenized and

centrifuged at 3600g for 4 minutes. After discarding the supernatant, the pellet was incubated in 100% acetone for 24 hours at 4 °C in dark. Post-incubation, the sample underwent another centrifugation at 3600g for 4 minutes, and the supernatant was collected to measure Chl a and c2 concentrations. Fluorescence readings at 630, 663, and 750 nm were applied to dinoflagellate-specific equations [62] and normalized to the coral surface area.

The remaining coral skeletons, after tissue removal, were treated with a 10% bleach solution and allowed to dry for 48 hours. To determine the surface area of each fragment, the paraffin wax dipping method was used [63]. The weight change of the wax-coated skeletons was compared to a standard curve generated with clay cylinders of known surface area, enabling the calculation of the skeletal surface area for each fragment.

2.2.16 Symbiodiniaceae density

Samples previously fixed in 4 % formalin were used to count Symbiodiniaceae cells from six independent hemocytometer (Improved Newbauer) counts under an optical microscope (Leica Company, France), as previously described [64]. Cell density was calculated by normalizing the surface area of respective fragments [65].

2.2.17 Oxidative Stress Analysis

Protein Extraction

Coral fragments were ground using a pre-chilled mortar and pestle, then transferred to tubes and homogenized in 750 µL of lysis buffer (50 mM Tris-HCl, pH 7.4, 150 mM NaCl, 10% glycerol, 1% NP-40 detergent, 5 mM EDTA) containing 1 mM phenylmethylsulphonyl fluoride (PMSF; Sigma-Aldrich). An initial centrifugation at 3000 rpm for 5 minutes was carried out to separate the skeletal material. The resulting samples were subjected to a second centrifugation (14,000 rpm, 4 °C, 15 minutes), and the supernatant was collected and promptly frozen at −80 °C for future

analysis. Protein concentration in each sample was determined using the Bradford assay, with bovine serum albumin (BSA) used to create the calibration curve.

Superoxide Dismutase Activity Assay

Superoxide dismutase (SOD) activity was measured following the method of Vance *et al*. [66]. SOD activity is determined by its ability to compete with ferricytochrome c for superoxide radicals (O_2^-) generated by the xanthine/xanthine oxidase system, inhibiting the reduction of ferricytochrome c. The reaction mixture included the following reagents (Sigma-Aldrich): 0.01 mM ferricytochrome c, 0.1 mM EDTA, 0.01 mM xanthine, and 0.0061 U xanthine oxidase, prepared in a final volume of 1 mL. Various sample volumes were added to the reaction mixture to achieve 50% inhibition of the reaction rate. The reduction of ferricytochrome c was monitored spectrophotometrically at 550 nm and 25 °C using a Varian Cary 50 Scan Spectrophotometer (Agilent Technologies). Under these conditions, one unit of SOD activity was defined as the amount of enzyme required to inhibit the reduction of ferricytochrome c by 50%. Results are reported as units (U) of enzyme activity per milligram of protein.

Catalase Activity Assay

Catalase (CAT) activity was assessed using its peroxidation function, following the method described by Bergmeyer and Graßl [67]. The assay measured the enzyme-driven breakdown of hydrogen peroxide (H_2O_2). The reaction mixture, prepared in a 1 mL cuvette, included 50 mM sodium phosphate buffer (pH 7.5) and 12 mM H_2O_2, to which varying sample volumes were added. The decrease in H_2O_2 concentration was tracked spectrophotometrically at 240 nm using a Varian Cary 50 Scan spectrophotometer (Agilent Technologies). Enzyme activity was expressed as units

(U) per milligram of protein, where one unit (U) corresponds to the first-order rate constant (min^{-1}), as outlined in reference [68].

Glutathione S-transferase activity assay

GST activity was assessed by considering the reaction of the enzyme with the 1-Chloro-2,4-dinitrobenzene (CDNB) substrate, according to Hayes and Strange [69]. The reaction solution (containing 200 mM potassium phosphate buffer pH 6.5, 20 mM CDNB dissolved in 95 % ethanol, and 20 mM reduced glutathione) was mixed in a 1 mL cuvette with different volumes of samples, and the formation of CDNB-oxidized glutathione conjugate was followed spectrophotometrically at 340 nm (Varian Cary 50 Scan spectrophotometer, Agilent Technologies). GST activity is expressed as units (U) of enzyme per mg of protein and is proportional to the increase in absorbance caused by conjugated product formation.

Glutathione reductase activity assay

The enzymatic assay of glutathione reductase (GR) was performed according to Wang *et al*. [70]. The activity of GR was evaluated through the spectrophotometric detection of the absorbance at 340 nm (Varian Cary 50 Scan spectrophotometer, Agilent Technologies) of NADPH oxidation to NADP+ reaction, which occurs in conjunction with the glutathione reduction, and is proportional to the decrease in absorbance over time. NADPH reaction was initially measured in the reaction mix (containing 0.1 M potassium phosphate buffer pH 7.6, 0.16 mM NADPH, 1 mg ml^{-1} BSA and 4.6 mM oxidized glutathione) and subsequently adding different volumes of the sample. GR activity was obtained from the difference of the two absorbance values. One unit of GR activity is defined as the oxidation of 1 nmol NADPH/min at 25°C. Results are expressed as units (U) of enzyme per mg of proteins.

Lipid Peroxidation

Lipid peroxidation levels were evaluated by measuring malondialdehyde (MDA) concentrations using a commercially available assay kit (Bioxytech LPO-586, Oxis International, USA). This method relies on the reaction between MDA and the chromogenic reagent N-methyl-2-phenylindole at 45 °C. Coral apex samples (~1 g each) were pulverized using a pre-chilled mortar and pestle and then homogenized in 1 mL of 20 mM phosphate buffer (pH 7.4). To prevent oxidation during processing, 10 µL of 0.5 M butylated hydroxytoluene in acetonitrile was added to each 1 mL homogenate. The homogenates were centrifuged at 3,000 × g for 10 minutes at 4 °C, and the supernatant was collected for protein quantification using the Bradford method.

The assay was performed following the hydrochloric acid solvent procedure provided by the kit's manufacturer. The absorbance of the resulting blue product was measured at 586 nm, as described by Gérard-Monnier *et al.* (1998) [71]. Results are expressed as µmol of MDA per µg of protein.

2.2.18 Statistics

Statistical analyses were performed using OriginPro software (OriginLab Corporation, Northampton, MA, USA). Data normality was verified using the Shapiro-Wilk test, and when assumptions were violated, appropriate transformations were applied. A one-way ANOVA test was applied to evaluate differences among experimental groups. When significant differences were detected, a Tukey post-hoc test was used to determine pairwise comparisons between the control and microparticle-treated samples. A p-value < 0.05 was considered statistically significant and highlighted by (*) in the graphs.

2.3 Results

2.3.1 Morphological analysis

A schematic representation of the film's three-layer preparation, along with photographs of each layer, is shown in **Figure 2.2**. The first layer, composed of carrageenan, pectin, and PVP, loaded with Cur-βCD, was fabricated using the solvent casting method and exhibits a reddish color, as shown in **Figure 2.2A**. In **Figure 2.2B**, the preparation of the second layer, which is composed of chitosan and PVP, loaded with Cur-βCD, and was deposited on the first layer by the rod coating method, is reported. Finally, the third layer was obtained by spraying a Zein solution on the bilayer (see **Figure 2.2C**). For the matter of clarity, a terminology legend is provided in the supporting information section.

SEM images of the top and cross-section views of the monolayer, bilayer, and three-layer systems were acquired to study the morphology of the samples and are reported in **Figures 2.3A, B,** and **C**. The first layer showed a quite rough surface, while the second and the third layers presented a smoother surface, most likely due to their different preparation methods. Cross-section images are shown in **Figures 2.3D, E,** and **F**. The separation between the two layers of the bilayer was just slightly evident because of their similar polymeric composition, mostly based on PVP and polysaccharides, and is indicated by the orange dashed line in **Figure 2.3E**. The cross-section of the three-layer system is reported in **Figure 2.3F**, where the different morphology of the third layer with respect to the other two is evident due to a composition based on zein protein. Here, the separation between layer 1 and layer 2 is highlighted in orange, while the blue lines indicate the separation between the bilayer and layer three. A difference in thickness was observed between the different layers when comparing the monolayer (≈180 ± 10 μm), the bilayer (≈280 ± 20 μm), and the three-layer (≈330 ± 35 μm), indicating that the second layer and the third layer had a thickness

of ≈100 ± 10 μm and ≈50 ± 15 μm, respectively. Thickness was evaluated using ImageJ software combined with the measurements using a digital caliper, and the results for all the samples are reported in **Table 2.1**.

Finally, SEM-EDX analysis was performed on the bilayer system to further distinguish the first two layers by tracing the sulfur (S) and other elements present only in the carrageenan, and thus in the first layer. Indeed, sulfur was observed in the first layer as the main element (**Figure 2.4**), whereas the second layer did not show a significant presence of this element and was mostly composed of carbon.

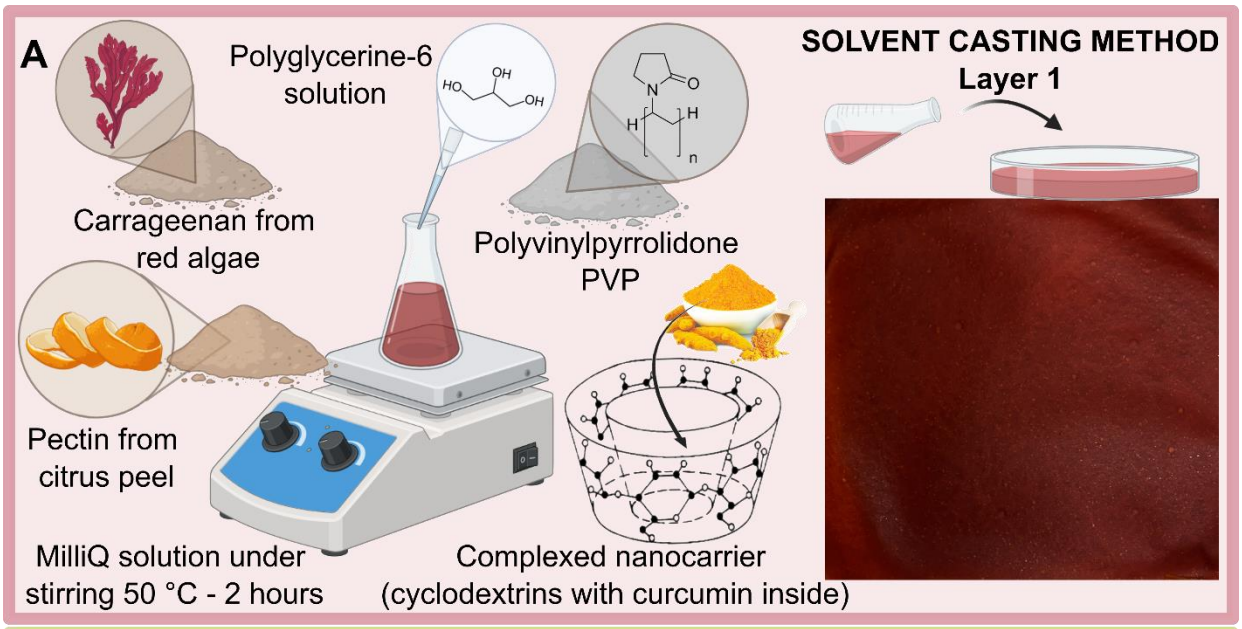
A
Polyglycerine-6
solution
SOLVENT CASTING METHOD
Layer 1
Carrageenan from
red algae
Polyvinylpyrrolidone
PVP
Pectin from
citrus peel
MilliQ solution under
stirring 50 °C - 2 hours
Complexed nanocarrier
(cyclodextrins with curcumin inside)

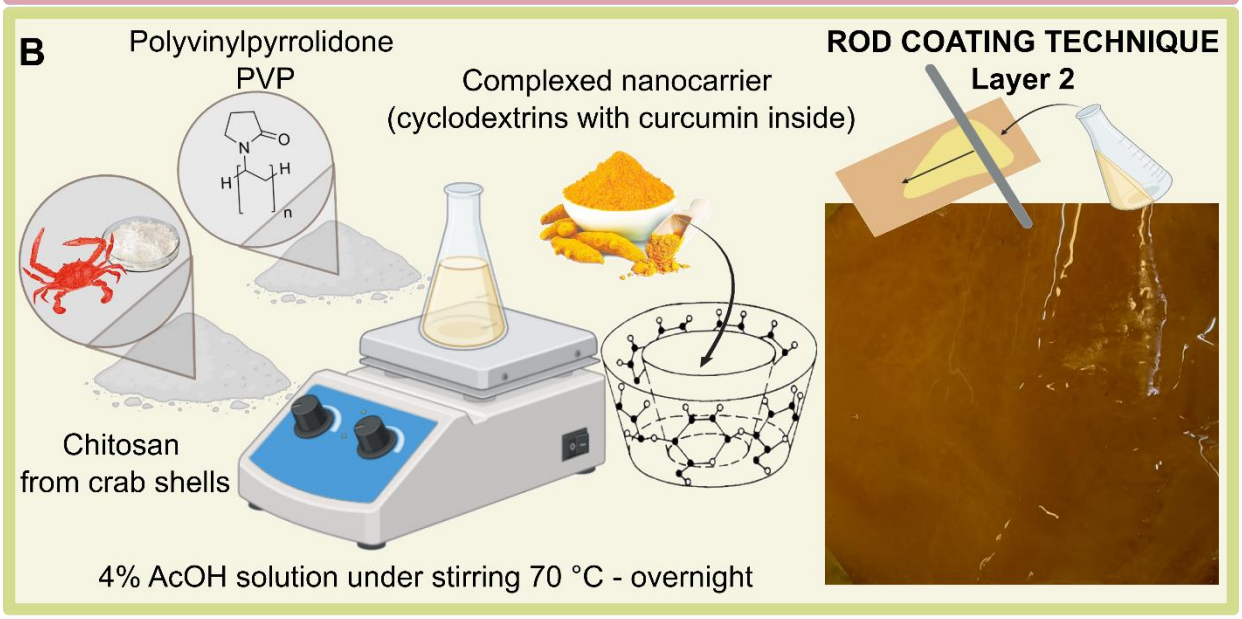
B
Polyvinylpyrrolidone
PVP
Complexed nanocarrier
(cyclodextrins with curcumin inside)
ROD COATING TECHNIQUE
Layer 2
Chitosan
from crab shells
4% AcOH solution under stirring 70 °C - overnight

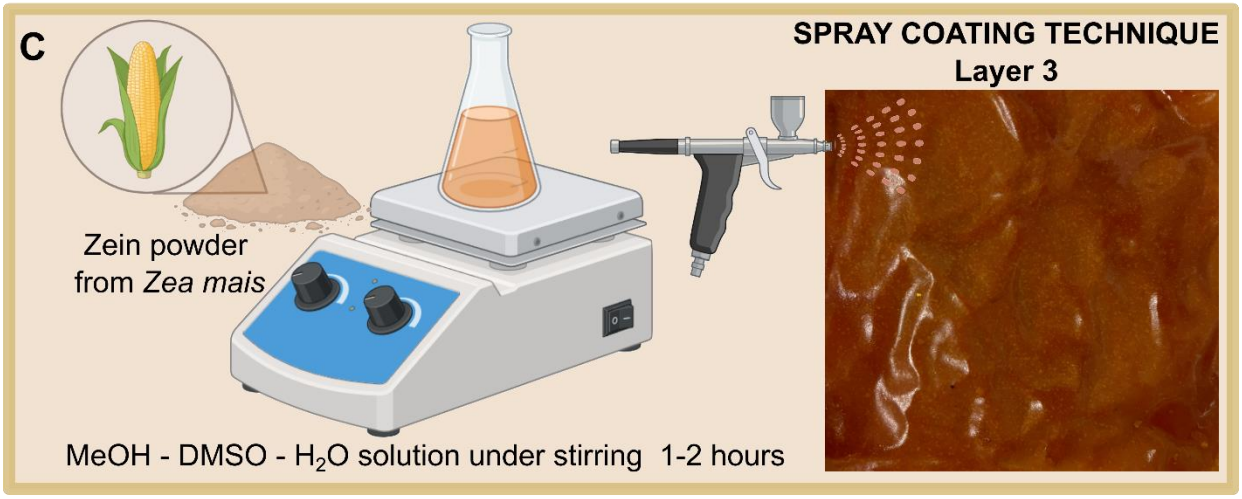
C
SPRAY COATING TECHNIQUE
Layer 3
Zein powder
from *Zea mais*
MeOH - DMSO - H_2O solution under stirring 1-2 hours

Figure 2.2 Schematic representation of the step-by-step three-layered film system preparation, from top to bottom: **A)** first layer of Pectin, Carrageenan, and PVP loaded with Cur-βCD; **B)** second layer composed of Chitosan and PVP loaded with Cur-βCD deposited on the first layer through the rod coating technique, and **C)** third layer made of Zein deposited on the second layer through the spray coating technique.

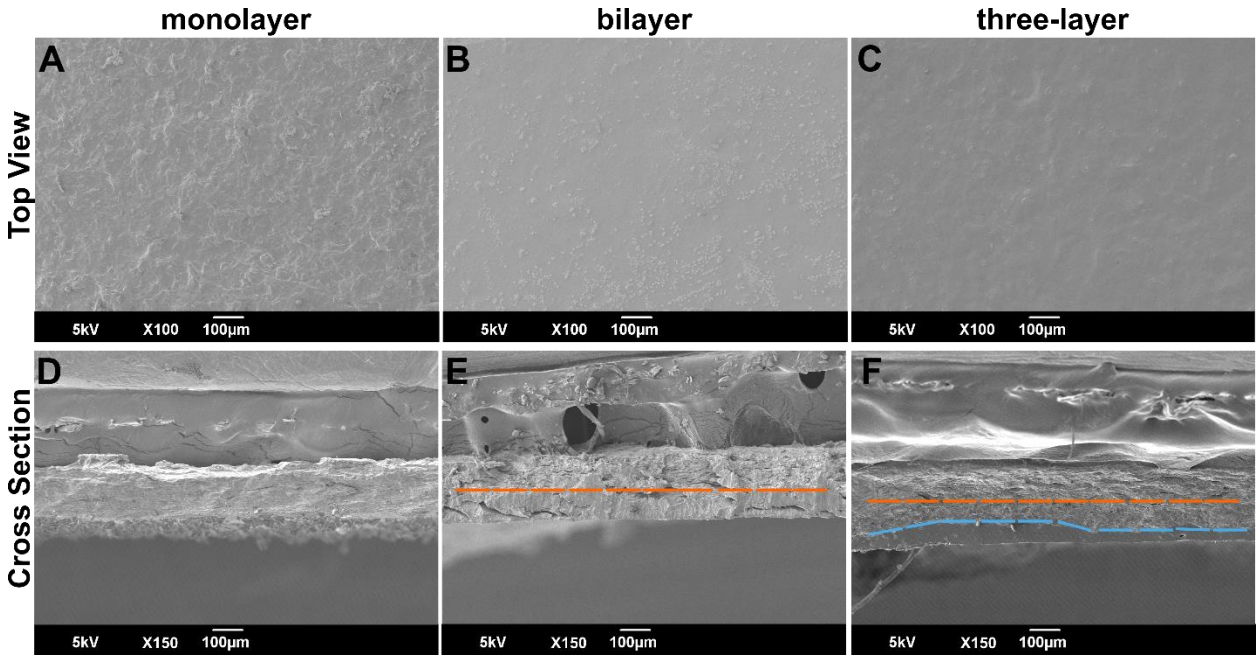

Figure 2.3 Top-view and cross-section SEM images of the materials. Top-view images of the **A)** monolayer, showing the surface of the first layer, **B)** bilayer, showing the surface of the second layer and **C)** three-layer sample, showing the surface of the third layer. Cross-section SEM images of the **D)** monolayer, **E)** bilayer, and **F)** three-layer sample. Orange and blue dashes indicate the separations between the first/second layer and the second/third layer, respectively.

Monolayer	Total	Layer 1	Layer 2	Layer 3
Length (µm)	180 ± 10	180 ± 10	/	/
Bilayer	**Total**	**Layer 1**	**Layer 2**	**Layer 3**
Length (µm)	280 ± 20	180 ± 10	100 ± 10	/
Three-layer	**Total**	**Layer 1**	**Layer 2**	**Layer 3**
Length (µm)	330 ± 35	180 ± 10	100 ± 10	50 ± 15

Table 2.1 Thickness of each layer for both bilayer and three-layer film systems.

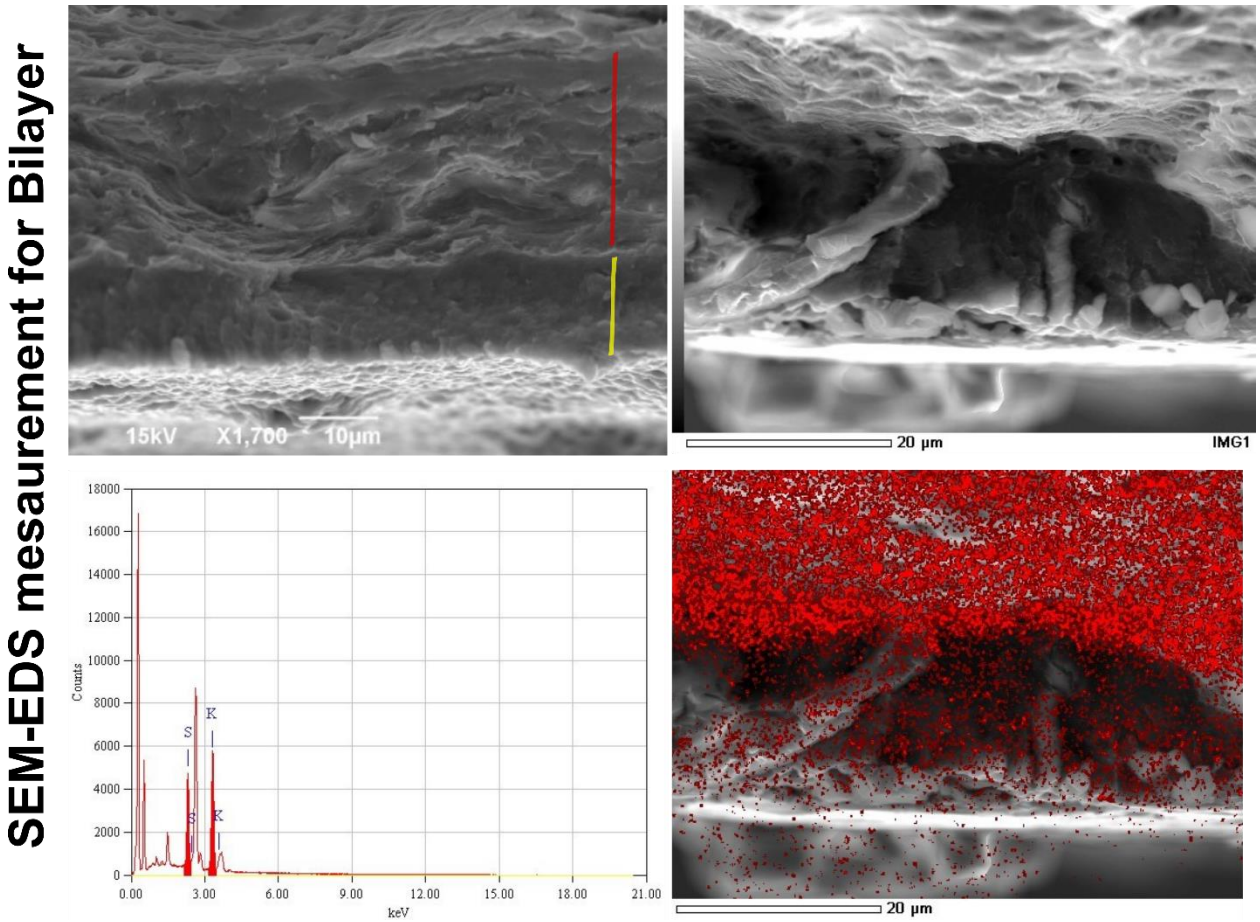

Figure 2.4 SEM-EDS analysis for bilayer system after ethanol-water dehydration and solvent fixation, highlighting separation among the two layers (layer 1 – red line and layer 2 – yellow line), indicated by the presence of sulfur (S) in layer 1 (made by carrageenan) and the absence of sulfur (S) in layer 2.

2.3.2 Chemical and mechanical characterizations of dry films

The UV-Vis absorbance of pristine curcumin and cur-βCD in water-ethanol was measured to evaluate the inclusion of the antioxidant compound within the ring-shaped molecules, before the production of the films. The main curcumin absorption band shifted from 425 nm for the pristine curcumin to 434 nm for the cur-βCD system (see **Figure 2.5A**). This shift to higher wavelengths, together with an increased water solubility of the cur-βCD system, suggests the successful incorporation and the resulting formation of a complexed nanocarrier, as also reported in the literature [57].

The fabricated monolayer, bilayer, and three-layer systems, and their pristine components, were chemically characterized by ATR-FTIR, and the spectra are reported in **Figures 2.5B**, **2.6**, and **2.7**. ATR-FTIR spectroscopy was used to characterize the chemical nature of the layers and eventual interactions among their ingredients. In **Figure 2.6A**, the spectra of the first-layer components are reported, and their characteristic peaks are assigned. The spectrum of carrageenan (black line) shows between 3400-3100 cm^{-1} the O-H stretching, the absorption bands between 1350-1200 cm^{-1} corresponding to asymmetric stretching of the O=S=O and S=O groups, and strong, broad absorption bands in the 1100 – 1000 cm^{-1} region represent the C-O-C and C-O stretching typical of polysaccharides [72]. In the pectin spectrum (red line), the O-H stretching mode appears between 3500-3100 cm^{-1}, the two strong bands at 1734 cm^{-1} and 1607 cm^{-1} indicate the ester carbonyl (C=O) groups and carboxylate ion stretching band (COO-), respectively [73]. The main bands of PVP (blue line) were associated with asymmetric and symmetric CH_2 stretching modes at 2951 and 2868 cm^{-1}, respectively, and the C=O stretching mode at 1657 cm^{-1} [74]. The spectrum of curcumin represented by the green line, showed free O-H stretching vibration at 3509 cm^{-1}, C-H aromatic and aliphatic stretching vibration from 3071 to 2845 cm^{-1}, C=O and C=C stretching

vibration of the inter-ring chain at 1628 cm^{-1}, C=O stretching vibration at 1506 cm^{-1}, CH_3 in-plane bending vibration of the methoxy group at 1457 cm^{-1}, C-O-H in-plane bending vibration connected to the enolic form at 1232 cm^{-1}, O-CH_3 stretching vibration of aromatic ring connected to "enolic" part at 1111 cm^{-1}, and C-O-C stretching vibration of aromatic ring connected with enolic" part at 1022 cm^{-1} [75]. Finally, the purple line reported the characteristic peaks of 2-hydroxy-propyl-β-cyclodextrin at 3368 cm^{-1} and 2926 cm^{-1}, corresponding to O-H and C-H stretching vibration, respectively, at 1420 cm^{-1} and 1369 cm^{-1}, corresponding to O-H and C-H bending vibration, respectively, and at 1158 cm^{-1} corresponding to C-O-C glycosidic stretching vibration. Ultimately, C-C and C-O stretching vibrations gave peaks at 1076 and 1020 cm^{-1}, respectively. From 945 to 606 cm^{-1}, stretching corresponding to the cyclodextrin ring was highlighted [76]. The spectrum of the monolayer (purple line in **Figure 2.6A**) showed bands mostly connected with the polymeric components. In the area of the carbonylic stretching, some variations were observed. The C=O of PVP had a red shift from 1657 to 1647 cm^{-1}. Under this band is also present the ester carbonyl (C=O) group of pectin, which moved from 1734 to around 1647 cm^{-1}, overlapped with the C=O of PVP. Similarly, the carboxylate group shifted from 1607 to 1601 cm^{-1} in the monolayer spectrum. These red shifts are typically attributed to the formation of H-bonds among the polymeric chains of the matrix.

FTIR spectra corresponding to the upper part of the bilayer system, thus to the second layer and its components, are reported in **Figure 2.6B**. PVP, curcumin, and β-cyclodextrins exhibit the same spectra as previously described in the monolayer and are here shown as black, blue, and green lines, respectively. Moreover, peaks of chitosan are highlighted in the red line. Specifically, the region between 3360 and 3290 cm^{-1} corresponds to N-H and O-H stretching, while the absorption bands around 2900 cm^{-1} can be attributed to asymmetric and symmetric C-H stretching. The

stretching of C=O (Amide I) occurred at 1649 cm^{-1}, the Amide II at 1582 cm^{-1}, and the stretching of C-N (Amide III) at 1319 cm^{-1}. Lastly, the absorption band at 1153 cm^{-1} can be attributed to the stretching of the C-O-C bridge, and the bands at 1057 and 1024 cm^{-1} to C-O stretching [77]. The purple line represents the FTIR spectrum of the second layer of the material. Peaks assigned to PVP, chitosan, and curcumin can be recognized. The main shifts can be found in the merged peaks of the C=O from PVP and the Amide I that fall at 1645 cm^{-1}, instead of 1657 and 1649 cm^{-1}, respectively.

Finally, the peaks of zein powder and the third layer, corresponding to the upper part of the three-layer system, are reported in **Figure 2.6C**. The zein spectrum is reported in black, while the complete spectrum of the third layer is in red. The two main peaks of zein powder were attributed to N-H and O-H at 3292 and 3188 cm^{-1}, respectively, aromatic and aliphatic C-H stretching between 3070 and 2853 cm^{-1}, and the Amide I at 1645 cm^{-1} [78]. In the third layer of the three-layer, zein solubilized and applied through spray drying shows the same peaks found in the powder, but it presents a shoulder in the Amide I peak, defining an alteration of the secondary structure of the protein in the direction of a higher presence of β-sheets and thus higher hydrophobicity [79–81].

Tensile tests for monolayer, bilayer, and three-layer samples were measured at 25°C and 44% relative humidity (RH). Stress-strain curves for each system are shown in **Figure 2.5C**. The monolayer had a Young's modulus (YM) of ≈ 2170 MPa, the bilayer ≈ 1240 MPa, and the three-layer ≈ 970 MPa (**Figure 2.5D**). Tensile stress at maximum load (TSML) of ≈ 22, ≈ 18, and ≈ 12 MPa was found for the mono, bi, and three-layer films, respectively (see **Figure 2.5E**). Finally, the elongation at break (EB) was ≈ 1.5, ≈ 2.7, and ≈ 3.0 %, in the mono, bi, and three-layer, respectively (see **Figure 2.5F**). The initial monolayer resulted in being a robust material, further stabilized by the H-bond interaction highlighted by the FTIR analysis. Adding the second layer

produced a reduction of the YM and the TSML. This can be explained by the increased presence of PVP inside the overall composition of the material, which is a typical hygroscopic material, and its mechanical properties are commonly affected by the humidity [46]. The three-layer film presented a further decrease in YM and TMSL, making it slightly more flexible and ductile (see photographs in **Figure 2.5G**). This ameliorated ductility is a crucial property, as it facilitates handling by operators and enables the material to conform to and wrap around corals of varying shapes. These variations in multilayered materials with respect to the single components and not-assembled layers have already been reported in the literature and were explained as the production of new polymeric rearrangements and interactions at the interfaces among the layers [82].

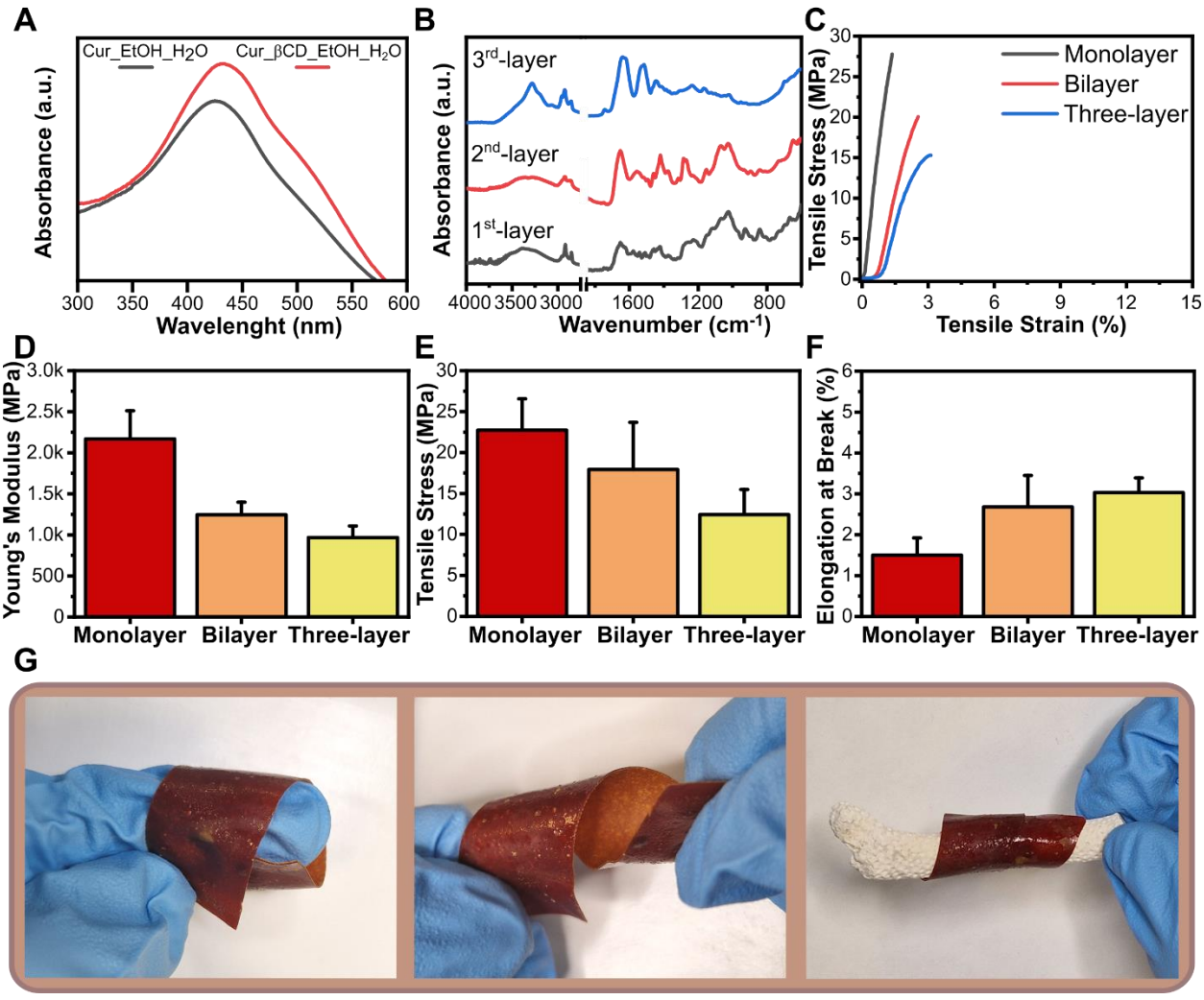

Figure 2.5 Comprehensive characterization of the materials through cur-βCD complexation, ATR-FTIR spectroscopy and mechanical tests **A)** UV-Vis absorbance of pristine curcumin and curcumin complexed within the nanocarrier βCD in ethanol-water solution. **B)** FT-IR normalized spectra for the upper part of the monolayer, bilayer (layer 2 up), and the three-layer (layer 3 up). **C)** Stress-strain curves for monolayer, bilayer, and three-layer. **D)** Young's modulus, **E)** tensile stress at maximum load, and **F)** elongation at break, respectively, of all the systems. The results are expressed as mean and standard deviation, with n = 10. **G)** Photographs of the three-layer material folded and wrapped around fingers and the coral skeleton.

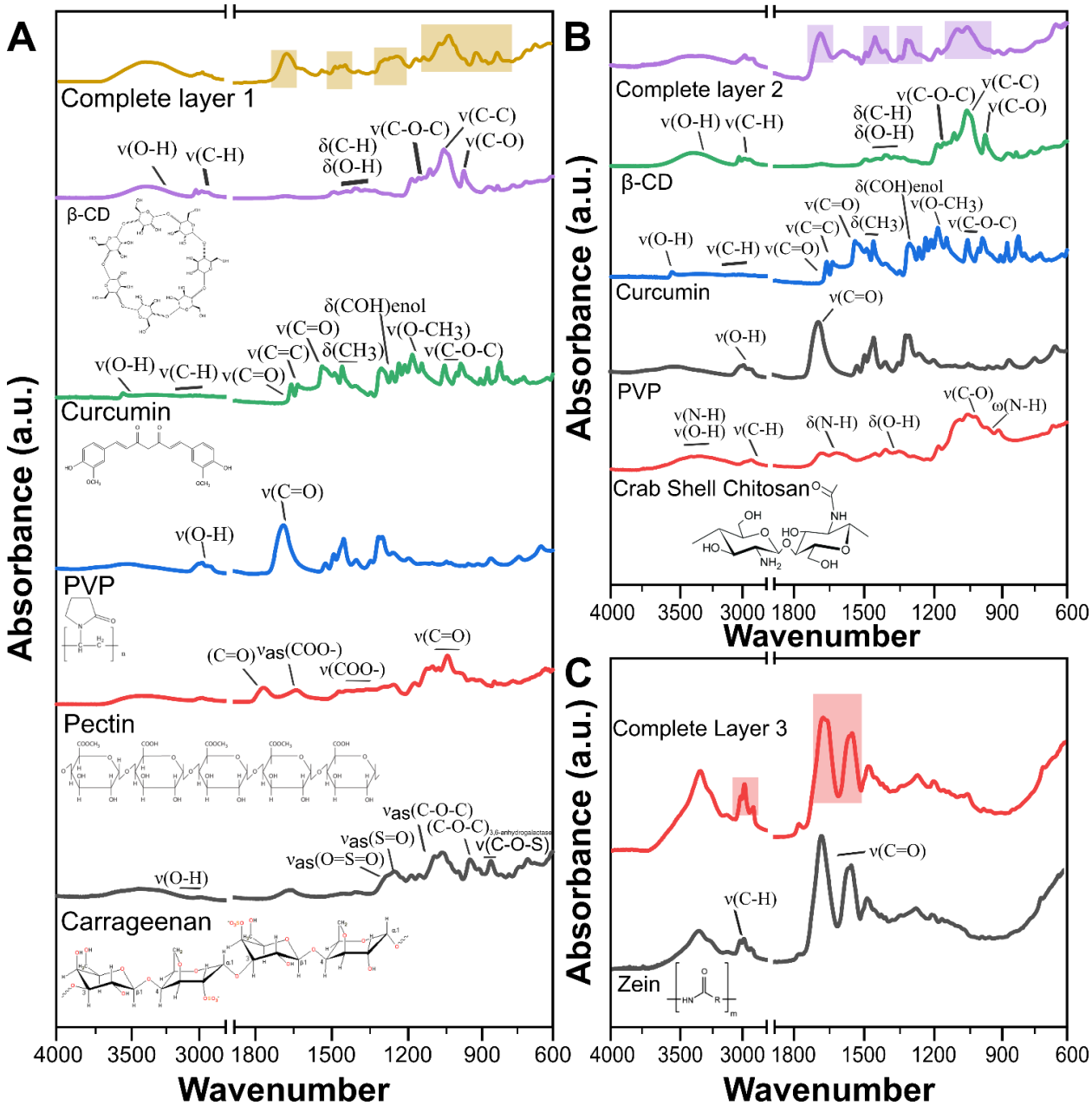

Figure 2.6 ATR-FTIR spectra of each component of each system. ATR-FTIR spectra of the upper part of **A)** monolayer (carrageenan-based), **B)** bilayer (second layer up – chitosan-based), and **C)** three-layer complete biofilm (third layer up – zein-based) with peak assignment for each component.

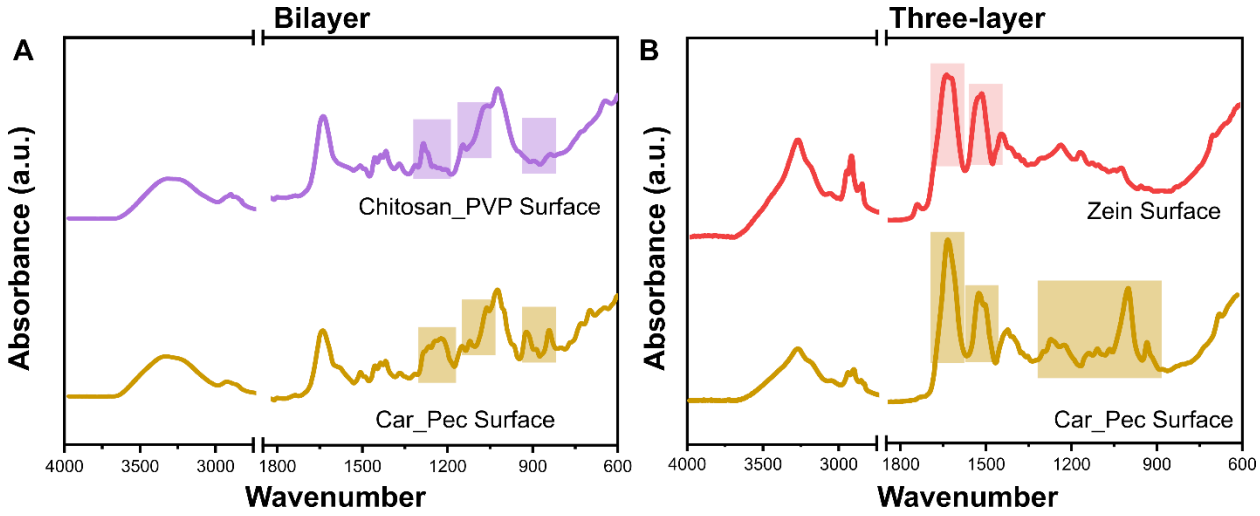

Figure 2.7 FT-IR analysis of both sides (up and down) of the bilayer and three-layered system **A)** bilayer (layer 2 up, layer 1 down) **B)** three-layer systems (layer 3 up, layer 1 down) with major peaks highlighted for each side.

2.3.3 Film – Water Interaction and Salty-Induced Crosslinking

Films' interactions with MilliQ and salty water were investigated through swelling, gel fraction, and rheological analyses. The swelling degree of monolayer, bilayer, and three-layer films immersed in MilliQ water for 24 hours is reported in **Figure 2.8A.** The monolayer system showed a quick swelling and consequent total dissolution after 40 minutes. Bilayer resisted underwater for a few more hours, showing a peak of swelling of ≈ 2000% after ≈1 hour, and dissolution in 4 hours. Three-layer films, instead, were still recoverable after 24 hours. In particular, they reached their swelling peak of ≈ 2500% after ≈ 4 hours, and then they started dissolving, although they were still measurable after 24 hours, due to the presence of the thin zein layer that did not dissolve in such a short time range.

Placing the films in salty water, they exhibited different behavior, as shown in **Figure 2.8B**. All the systems were quite stable in salty water, showing their highest values of swelling after 4 hours,

of ≈ 335 for the monolayer, ≈ 930 for the bilayer, and ≈ 960 for the three-layer, and then stabilizing their swelling around 500-600% after 24 hours.

Finally, **Figure 2.8C** reports the gel fraction degree for each system in salty water, whereas, as mentioned before, this analysis was impossible to obtain with the MilliQ water because the films dissolved. Gel fraction values were 65%, 80%, and 85% for the mono, bi, and three-layer systems, respectively, after 24 hours immersed in seawater.

Rheological analyses of the three systems upon immersion in salty water for 3 and 24 hours were carried out to further characterize their physical state and the mechanical properties. These two time points were chosen because the maximum degree of swelling was obtained after 3 hours, and after 24 hours, the swelling stabilized (see **Figure 2.8B**). Amplitude and frequency sweep tests were carried out for the different samples.

The materials, both at 3h and 24h, showcased a gel-like behavior in hydrated conditions, as confirmed by looking at **Figures 2.9C-2.9D,** where all the samples showed the elastic modulus (G') consistently higher than the viscous modulus (G″) across the entire frequency range. The three-layer system was the system that displayed the highest magnitude of both G'and G'' at every time point.

Even if showcasing a solid gel-like behavior, at 24h, all the samples displayed a slight decrease in complex viscosity, with respect to 3h, as visible in **Figures 2.8D, E, F.** This can be linked to the increased water content after 24 h with respect to the previous time point, confirming the swelling dynamics shown in **Figure 2.8B**. The results of the rheological analysis confirmed that once immersed in seawater, the different layers can absorb and retain salty water and assume a gel-like behavior in agreement with what is expected from a hydrogel.

This different way of interaction with MilliQ and salty water can be justified by the difference in ionic concentration and pH of the two media. Indeed, the main polymers composing the films undergo a crosslinking of their chains in the presence of ions. For instance, the presence of divalent ions, like calcium ions (Ca^{2+}) that can be found in salty water, has been widely demonstrated to increase water stability as well as the mechanical properties of pectin [83–85]. Similarly, it is well-known that carrageenan crosslinks in the presence of calcium ions (Ca^{2+}) and potassium ions (K^{+}), assuming a hydrogel-like behavior [86–88]. Moreover, chitosan results in much less solubility in basic conditions, further stabilizing the entire structure when immersed in salty water, which has a common pH of 8.2 [89].

2.3.4 Drug release studies, antioxidant and biodegradation properties

The three-layered material was designed to ensure a controlled, constant, and directional release of the cur-βCD nanocomplex once immersed in the seawater. Two experiments were carried out to evaluate the drug release performance. The first studied the overall drug release kinetics from the three layers under complete water immersion and anisotropic conditions. In contrast, the second one investigated whether the protective zein-based third layer could help address the release in a specific direction.

Results of cur-βCD nanocomplex diffusion from all the systems immersed in salty water are shown in **Figure 2.10**. The monolayer showed a burst release profile, losing 80% of the drug within the first 4 hours and reaching 100% in 24 hours. This is in agreement with the quick swelling behavior of this material. On the other hand, in the bilayer and three-layer materials, the release occurred more slowly and was prolonged, reaching the total drug release after 168 hours. The release starts almost immediately, reaching 30-40% after 8 hours, which can be linked to the drug diffusion from the first layer. After the initial burst of the release, the antioxidant compound was continuously

released from the second layer of the bilayer and the three-layer samples. The reduced kinetics can be explained by the fact that after 24 hours, the first layer did not dissolve, as also proved by the gel fraction results, and the drug from the second layer needs to diffuse across this further barrier. At the same time, chitosan in contact with seawater highly reduces its solubility due to the slightly basic pH. Therefore, after the initial swelling within the first hours, the main driving force of the release can be attributed to the slow erosion of the first and second layer matrices, allowing an overall slow and constant diffusion of the drug.

To study the unidirectionality of cur-βCD towards the organisms, once the material is placed near or directly in contact with the coral, a Transwell system was used, as shown in **Figure 2.8G**. In the Transwell system, the top represents the coral target, while the bottom simulates the marine environment. In the upper compartment, the release resulted in being constant and controlled, and after 24 hours, around 30% of the cur-βCD diffused. At the same moment, 10% of the overall dose was found in the lower compartment, which is probably due to the burst initial release and swelling of the film in the first hours of immersion. Afterward, the remaining part of the dose, about 50%, was released only in the upper compartment, and the other 10% in the lower compartment. At the end of the experiment, 80% of the overall dose was found in the target compartment rather than the other side, demonstrating excellent barrier properties of the hydrophobic third layer and allowing a directional diffusion of the antioxidant.

Since curcumin is very well known for its antioxidant properties, ABTS assays were conducted to determine the antioxidant capacity of monolayer, bilayer, and three-layered film systems after their fabrication. Results are reported in **Figure 2.8H**. After 4 hours, all the tested samples showed the maximum percentage of radical scavenging activity, as can also be noticed by the absence of the typical ABTS blue color in the cuvette in the inserted photo.

Finally, with a view to marine application, a fundamental point to verify is that the materials are biodegradable in that environment. For this reason, biochemical oxygen demand was conducted for monolayer, bilayer, and three-layered film systems. All the samples were studied for 30 days. Microcrystalline cellulose was tested as a positive control of biodegradation, while polyethylene (PE) was tested as a negative control of biodegradation [90,91]. The main results are reported in **Figure 2.8I**. The monolayer showed the highest degradation rate, obtaining a value of 30 mg O_2/100 mg material. Instead, the bilayer presented an oxygen consumption of 20 mg O_2/100 mg, and the three-layer of 14 mg O_2/100 mg, still higher than the value of 10 mg O_2/100 mg obtained for the microcrystalline cellulose. As expected, the PE did not show any signal of biodegradation.

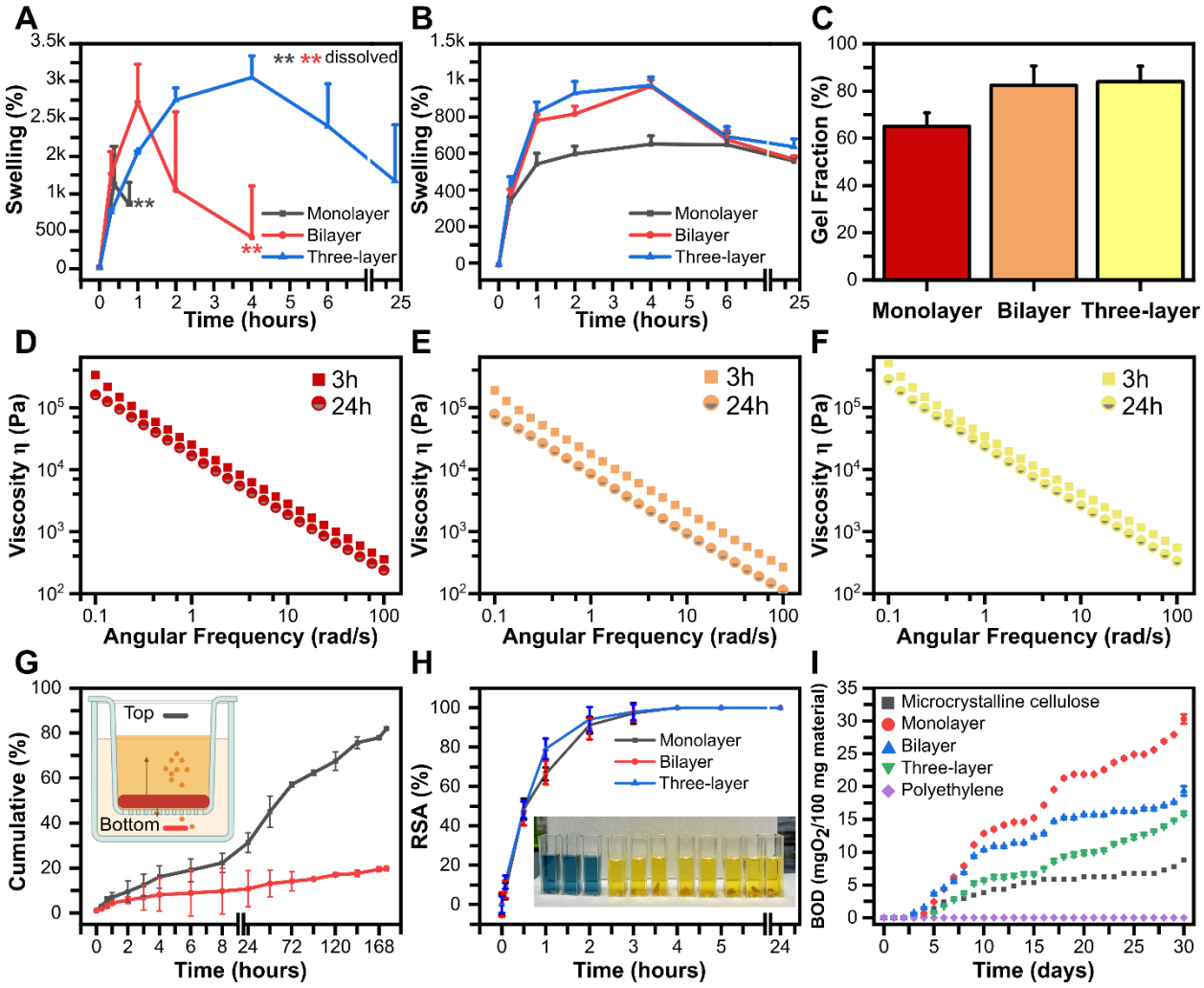

Figure 2.8 Comprehensive characterization of the materials through swelling and gel fraction test, rheology and biological test. Swelling percentage of monolayer, bilayer, and three-layer in **A)** MilliQ water and **B)** salty water. and **C)** gel fraction results for monolayer, bilayer, and three-layer after complete submersion within salty water. Results are shown as mean and standard deviation with n = 5. Shear strain results from rheological test on **D)** monolayer, **E)** bilayer, and **F)** three-layer samples after 24 hours submerged in salty water. **G)** Data from the unidirectional cumulative cur-βCD release experiment from the three-layer system in Transwell. The red line represents the bottom compartment of the Transwell, while the black one represents the upper compartment. The material is placed in the well with the zein-based hydrophobic layer in contact with the meshed membrane of the Transwell and the carrageenan-based hydrophilic layer towards the medium. **H)** Radical scavenging activity of each system in the ABTS assay. A photograph of the cuvette

with the control ABTS solution and the ABTS solution in contact with the materials after 24 hours is inserted. **I)** BOD showing results of monolayer, bilayer, and three-layer compared to a positive control - microcrystalline cellulose – and a negative control - PE. Results are shown as means and standard deviation with n=3.

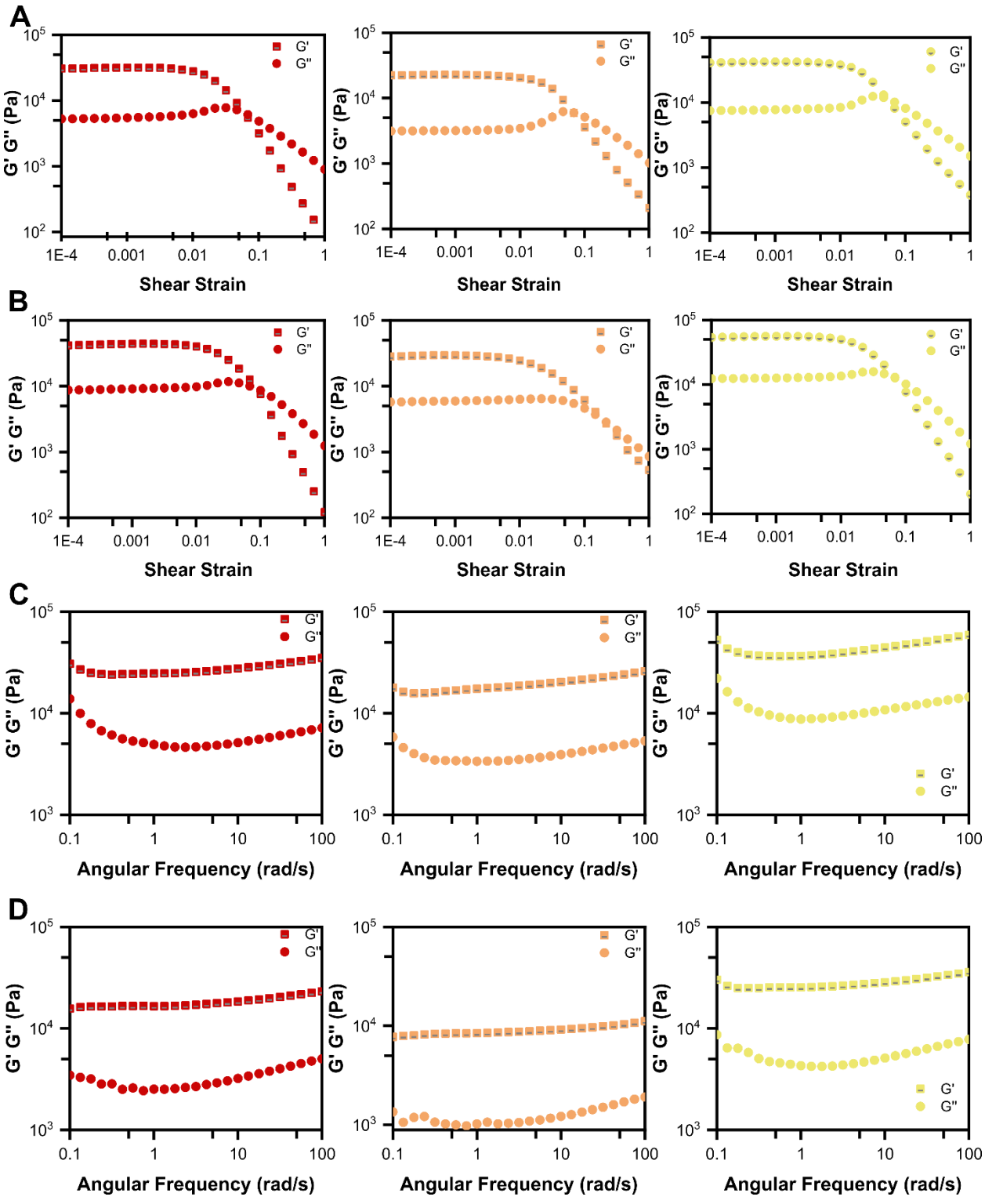
A
B
C
D
G'
G"
G' G" (Pa)
Shear Strain
Angular Frequency (rad/s)
1E-4
0.001
0.01
0.1
1
10
100

Figure 2.9 Rheological test of each system after 3h and 24h immersed in salty water. Amplitude sweep tests results on monolayer, bilayer, and three-layer after complete immersion in salty water for **A)** 3 hours and **B)** 24 hours; frequency sweep tests results on monolayer, bilayer, and three-layer after complete immersion in salty water for **C)** 3 hours and **D)** 24 hours.

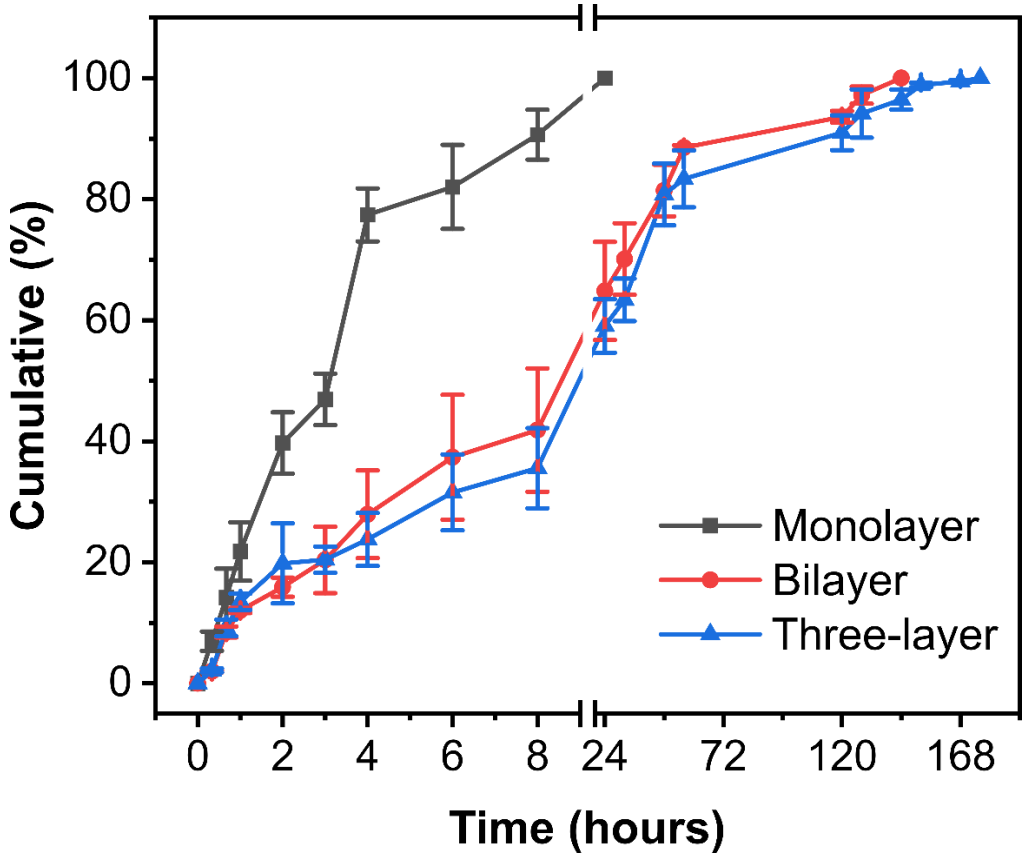

Figure 2.10 Drug release profile for cur-βCD nanocomplex diffusion from monolayer, bilayer, and three-layer film system through time.

2.3.5 Three-Layered Films on Corals during an Induced Thermal Stress Model

The biocompatibility and efficacy of the three-layer film system in reducing thermal stress susceptibility were evaluated in vivo at the Genoa Aquarium using a four-phase coral bleaching setup on *Stylophora pistillata*. An induced thermal stress model was designed to investigate the efficacy of the three-layered film system on corals during a simulated bleaching condition.

Specifically, four phases were reproduced: acclimation (**A**), heat stress (**HS**), bleaching (**B**), and recovery (**R**). Corals were divided into two different experimental groups: the untreated and the treated with the three-layered film. In **Figure 2.11,** the experimental setup for the film treatment is reported. Films were cut into ~5 x 5 cm^2 pieces and attached to a rigid support through marine epoxy resin (**Figures 2.11 A, B,** and **C**). The supports were then positioned at each side of the treatment tank - without direct contact with the skeleton - at ~5 cm from the corals, as shown in **Figure 2.11D**. This approach was selected to prevent further stress while providing a form of pre-treatment that allowed curcumin to diffuse gradually into the coral tissue. Indeed, as highlighted by the orange color in the proximity of the film, Cur-βCD was slowly released in the water (**Figure 2.11E**) and diffused within the tank thanks to the airflow, thus reaching all the coral fragments. The experimental setup of the coral bleaching experiment, with the associated visual appearance of untreated and treated corals for each phase, is shown in **Figure 2.12**. For each phase, the temperature setup and the duration of the phase are schematically reported in **Figure 2.12**, as well as the number of corals sampled.

Physiological parameters (content of chlorophylls, Symbiodiniaceae density, and enzyme activity) were monitored to assess the overall health of the corals in the experiment. During the acclimation phase, schematically represented in **Figure 2.12A**, after 7 days at 25 °C, no significant morphological changes were observed on corals, as well as after the heat stress phase (**Figure 2.12B**), where temperature progressively increased by 0.5 °C per day. However, after the continuous exposure to 31°C for one week during the bleaching phase (**Figure 2.12C**), and at the end of the recovery phase, in which the temperature was gradually reduced by 1°C per day back to 25°C (**Figure 2.12D**), corals in the control tank displayed some small white spots as highlighted by the zoom-in in the picture. Nevertheless, to clarify the effect of the delivered cur-βCD

nanocomplex into corals during the thermal stress model, bleaching biomarkers inside the coral tissue were analyzed during each phase and experimental group. All the results are reported in **Figure 2.13**, and the different colors represent the different phases of the model.

The bleaching phenomenon causes the breakdown of the symbiosis between the polyps and their algae; for this reason, as first biomarkers, the content of chlorophyll *a*, chlorophyll c_2, and the Symbiodiniaceae cell density were quantified. For these three biomarkers, no significant changes were noticed between the two experimental groups (treated and untreated) during the first two phases of the experiment (**Figures 2.13A**, **2.13B**, and **2.13C**). Instead, during the bleaching phase, significant differences in content of chlorophylls and Symbiodiniaceae cell density were observed between untreated control corals and those treated with the three-layered film system, with untreated corals showing consistently lower values. Specifically, chlorophyll *a* and c_2 levels were ~6.3 ± 0.1 μg/cm² and ~1.4 ± 0.2 μg/cm² in untreated corals, compared to ~8.1 ± 0.1 μg/cm² and ~2.1 ± 0.1 μg/cm² in treated corals, respectively (Chl_*a* *p=0.000077; Chl_c_2 *p=0.013) (**Figures 2.13A** and **2.13B**). Similarly, Symbiodiniaceae cell density was lower in untreated corals (~0.6 ± 0.1 × 10^6 cells/cm2) than in treated ones (~1 ± 0.1 × 10^6 cells/cm^2) during the bleaching phase (*p=0.000029). In the recovery phase, the trend was kept despite no statistical significance obtained for the two chlorophylls, whereas the content of Symbiodiniaceae was still significantly different, with values of ~0.7 ± 0.1 × 10^6 cells/cm^2 and ~1 ± 0.1 × 10^6 cells/cm^2 as shown in **Figure 2.13C** (*p=0.0028).

One of the main causes of coral bleaching is oxidative stress, and corals, in response to this, produce enzymes that can buffer/scavenge the propagation of oxidative species. Here, the levels of coral Superoxide dismutase (SOD), Catalase (CAT), Glutathione S-transferase (GST), and Glutathione reductase (GR) were evaluated, and the results are reported in **Figures 2.13D**, **E**, **F**,

and **6G**. The overall activity level of these enzymes increased moving from the acclimation phase to the heat and bleaching phases because of the induced thermal stress. The level of SOD between the untreated and treated samples did not seem to be strongly different in the trend during the heat stress (≈ 0.81 U/mg), while it became slightly lower for the treated corals in the bleaching phase (untread ≈ 0.87 U/mg, treated ≈ 0.72 U/mg). Instead, during the recovery phase, the treated corals presented a statistically much lower level of this enzyme (untread ≈ 0.75 U/mg, treated ≈ 0.32 U/mg, *p=0.0051). CAT was strongly expressed during the heat, bleaching, and recovery phases in the untreated corals with values of 0.058, 0.054, and 0.051 K/mg, respectively. On the contrary, the CAT values for the treated corals in the HS, B, and R phases were 0.038, 0.036, and 0.020 K/mg, respectively, resulting in a statistically significant difference in the R phase (*p=0.022). GST showed a peak of expression during the HS phase in the untreated samples ≈ 0.013 U/mg, and then stabilized in the B and R phases at ≈ 0.010 U/mg. The treatment gave a statistically positive protection on the HS phase with GST levels of ≈ 0.008 U/mg (*p=0.048), and then slightly increased in the other two phases (B ≈ 0.009 U/mg; R ≈ 0.010 U/mg), reaching comparable values to the untreated corals. Finally, GR levels increased in the HS phase for the untreated samples (≈ 0.051 U/mg) and were statistically different from the treated corals (≈ 0.036 U/mg) (*p=0.024). In the B and R phases, no significant differences or trends were observed for this enzyme.

Oxidative stress generates an overproduction of ROS, which can damage cellular components such as DNA, proteins, and lipids. Interaction between ROS and lipids leads to the generation of lipid peroxidation (LPO), and, for this reason, it is considered a clear and ubiquitous sign of ROS-induced cellular damage [92].

Therefore, as a final biomarker of coral health status and thermal-induced damage, LPO levels were evaluated in all the phases and the experimental group, and the results are reported in **Figure**

2.13H. In the A and HS phases, LPO levels did not show significant variations (A ≈ 0.06 μM MDA/μg protein and HS ≈ 0.07 μM MDA/μg protein for both treated and untreated in the two phases), probably due to the time required for ROS to induce the damage. During the B phase, it became evident how the heat stress produced high amounts of ROS, and consequently, the untreated corals presented LPO values of ≈ 0.40 μM MDA/μg protein, while the samples treated with the cur-βCD nanocomplex had LPO levels of ≈ 0.14 μM MDA/μg protein (*p=0.08). Finally, in the R phases, the untreated corals still presented higher damage with LPO values of ≈ 0.22 μM MDA/μg protein compared to the treated ones with LPO of ≈ 0.10 μM MDA/μg protein.

In general, the overproduction of enzymes, together with the decreased levels of chlorophylls, Symbiodiniaceae cells, and increased LPO, which are considered inter- and intramolecular signals of ROS damage and stress, confirmed the suitability of this induced thermal-stress model [93–95]. An overall positive effect of the three-layered material for the administration of cur-βCD nanocomplex could be observed in all the biomarkers taken into consideration. These significant differences in the antioxidant enzymes, especially in the heat stress and recovery phases, may indicate that treated corals likely required lower enzyme activity than control corals due to the ROS-scavenging effect of βCD-curcumin complexed nanocarrier.

Finally, a schematic representation and summary of the effects of the heat and the three-layer film applications are reported in **Figure 2.14**.

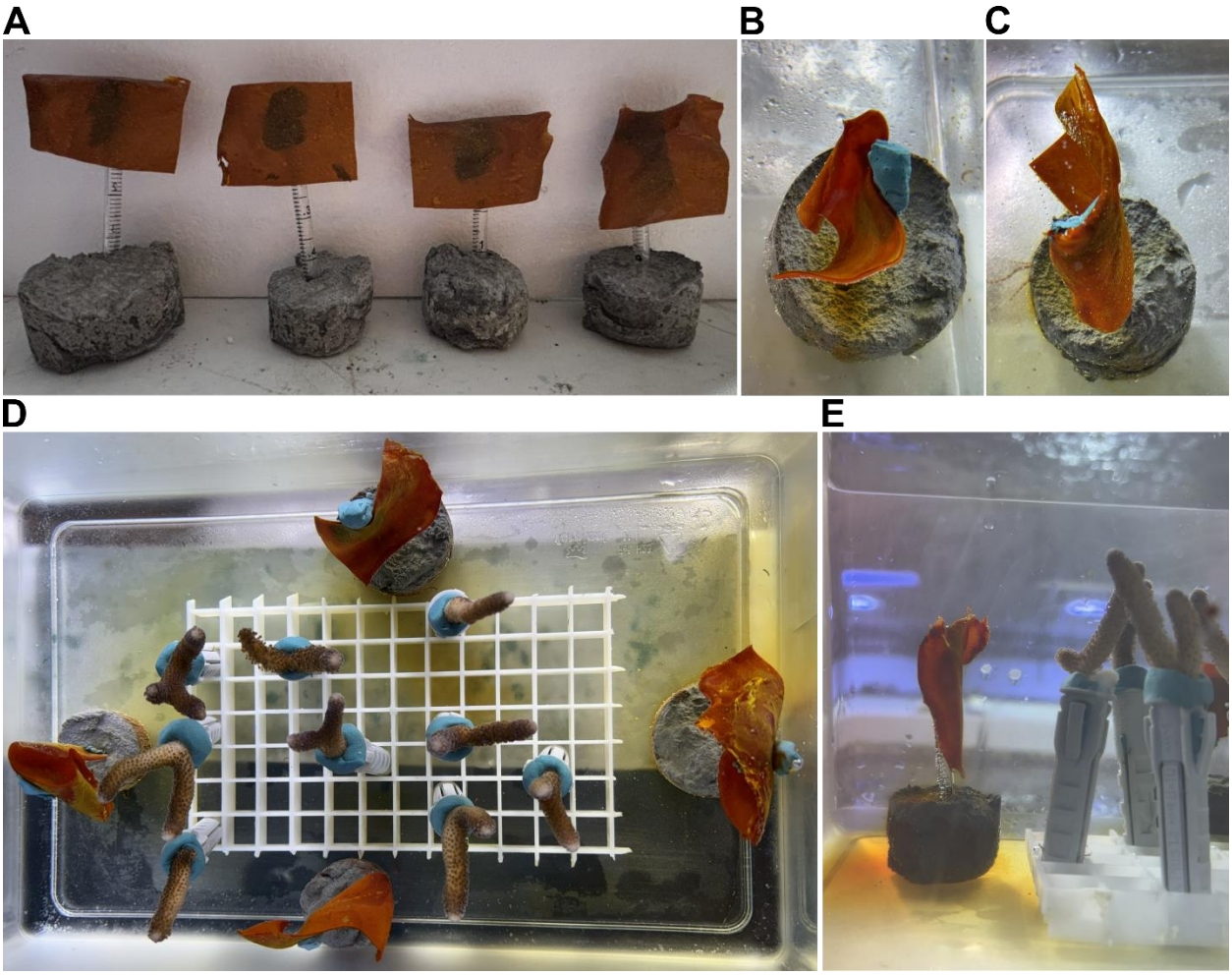

Figure 2.11 Three-layered film system application *in vivo* – coral bleaching set up **A) B) C)** three-layer film system pieces cut and attached on supports for cur-βCD delivery once submerged into the water; **D)** three-layer film system treatment tank with coral fragments; **E)** focus on the orange color of the water once the system is placed in the tank and starts the cur-βCD release.

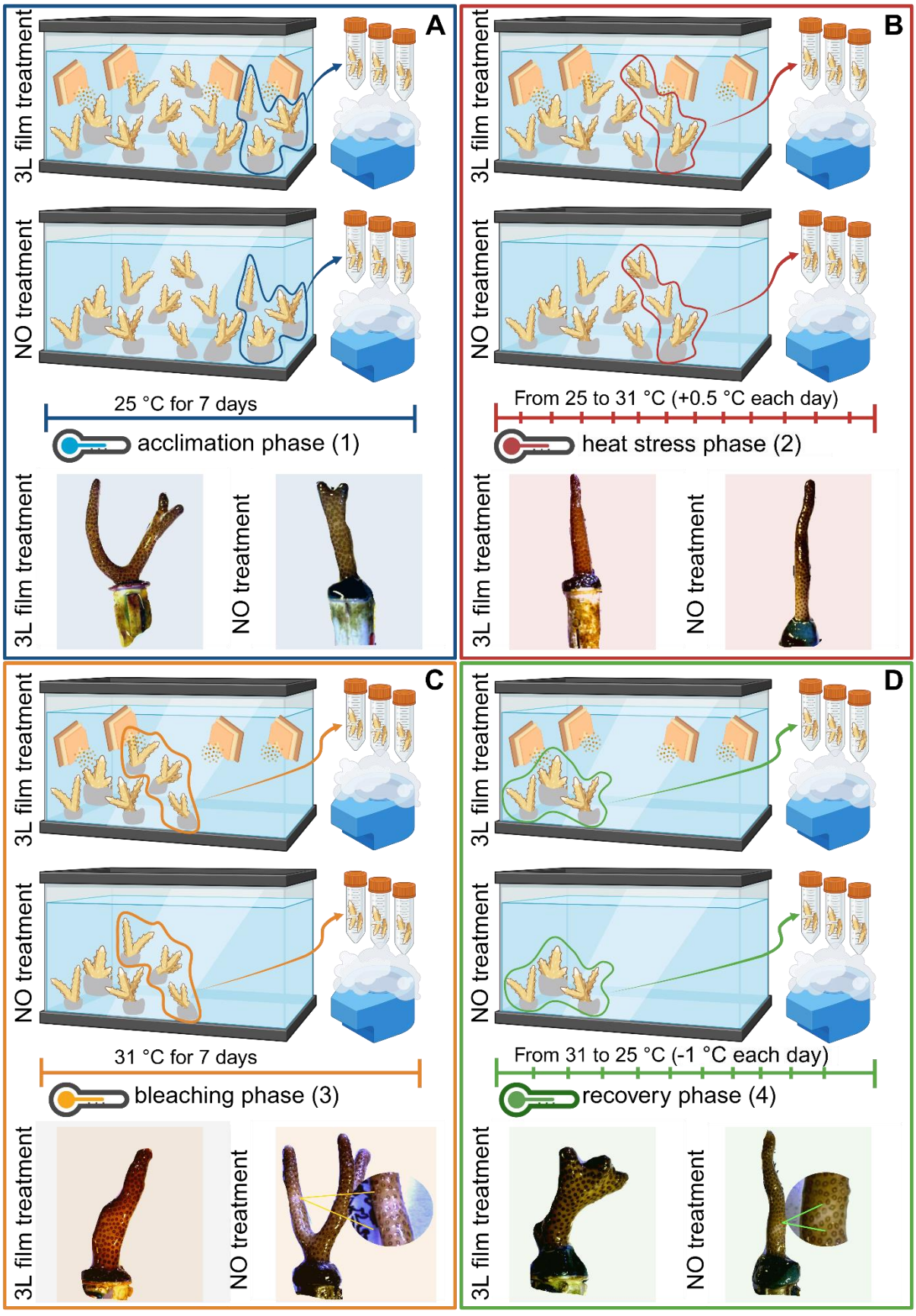
A
3L film treatment
NO treatment
25 °C for 7 days
acclimation phase (1)
3L film treatment
NO treatment
B
3L film treatment
NO treatment
From 25 to 31 °C (+0.5 °C each day)
heat stress phase (2)
3L film treatment
NO treatment
C
3L film treatment
NO treatment
31 °C for 7 days
bleaching phase (3)
3L film treatment
NO treatment
D
3L film treatment
NO treatment
From 31 to 25 °C (-1 °C each day)
recovery phase (4)
3L film treatment
NO treatment

Figure 2.12. Schematic representation of each phase of the experimental setup and relative visual results. At each phase, **A)** acclimation phase, **B)** heat stress phase, **C)** bleaching phase, and **D)** recovery phase, relevant comparisons between the untreated control coral and the corals treated with the three-layered film system were highlighted through qualitative pictures.

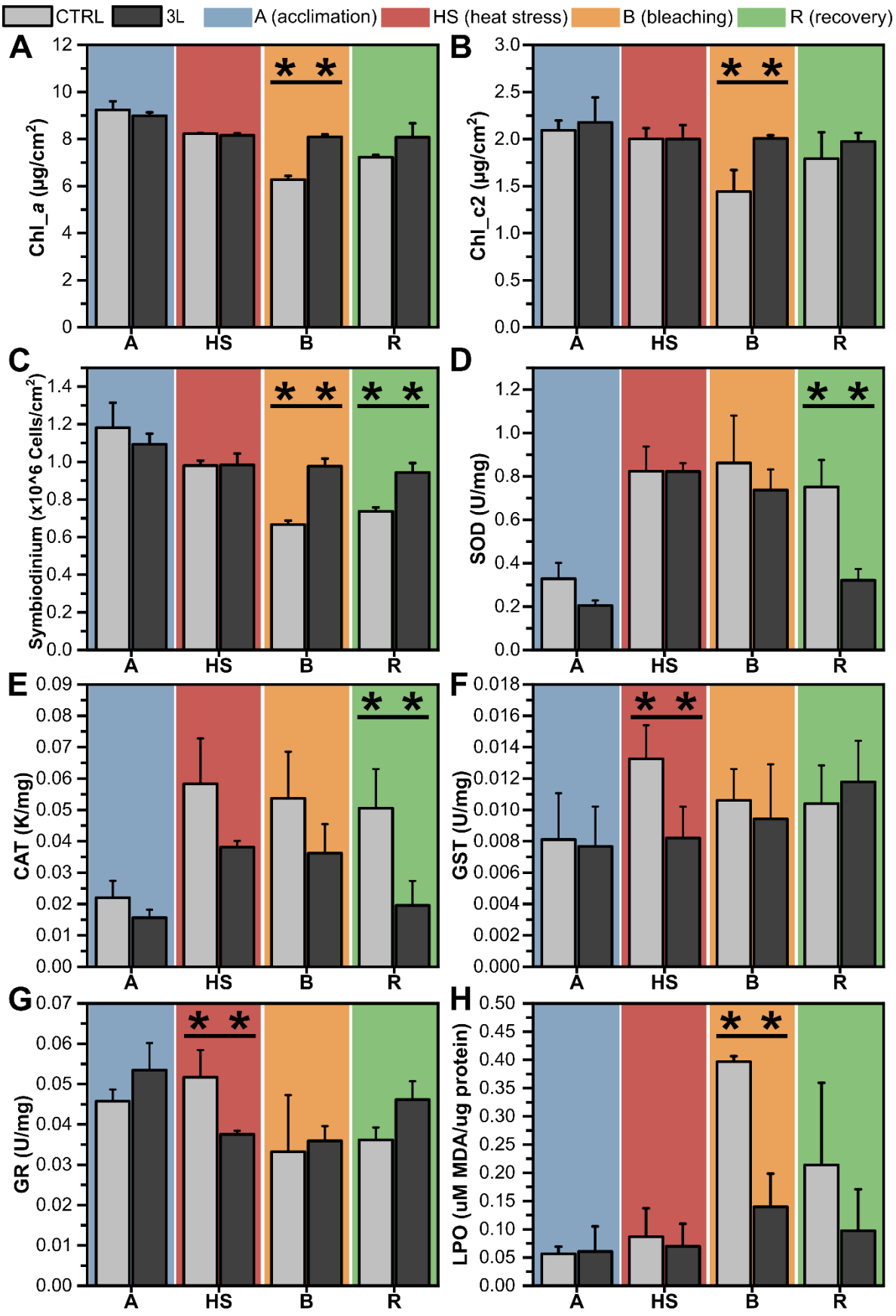
CTRL
3L
A (acclimation)
HS (heat stress)
B (bleaching)
R (recovery)
A
Chl_a (µg/cm²)
B
Chl_c2 (µg/cm²)
C
Symbiodinium (x10^6 Cells/cm²)
D
SOD (U/mg)
E
CAT (K/mg)
F
GST (U/mg)
G
GR (U/mg)
H
LPO (uM MDA/ug protein)
A
HS
B
R
* *

Figure 2.13. Results from molecular analysis on heat stress's major biomarkers. **A)** chlorophyll a *$p < 0.05$ CTRL vs 3L (bleaching phase P=0.000077), **B)** chlorophyll c2 *$p < 0.05$ CTRL vs 3L (bleaching phase P=0.013), **C)** Symbiodiniaceae cell density *$p < 0.05$ CTRL vs 3L (bleaching phase P=0.000029, recovery phase P=0.0028), **D)** SOD, *$p < 0.05$ CTRL vs 3L (recovery phase P=0.0051), **E)** CAT *$p < 0.05$ CTRL vs 3L (recovery phase P=0.0212), **F)** GST *$p < 0.05$ CTRL vs 3L (heat stress phase P=0.048), **G)** GR *$p < 0.05$ CTRL vs 3L (heat stress phase P=0.024), and **H)** LPO *$p < 0.05$ CTRL vs 3L (bleaching phase P=0.008) for both control corals and three-layered film system-treated corals in each phase of the coral bleaching experiment.

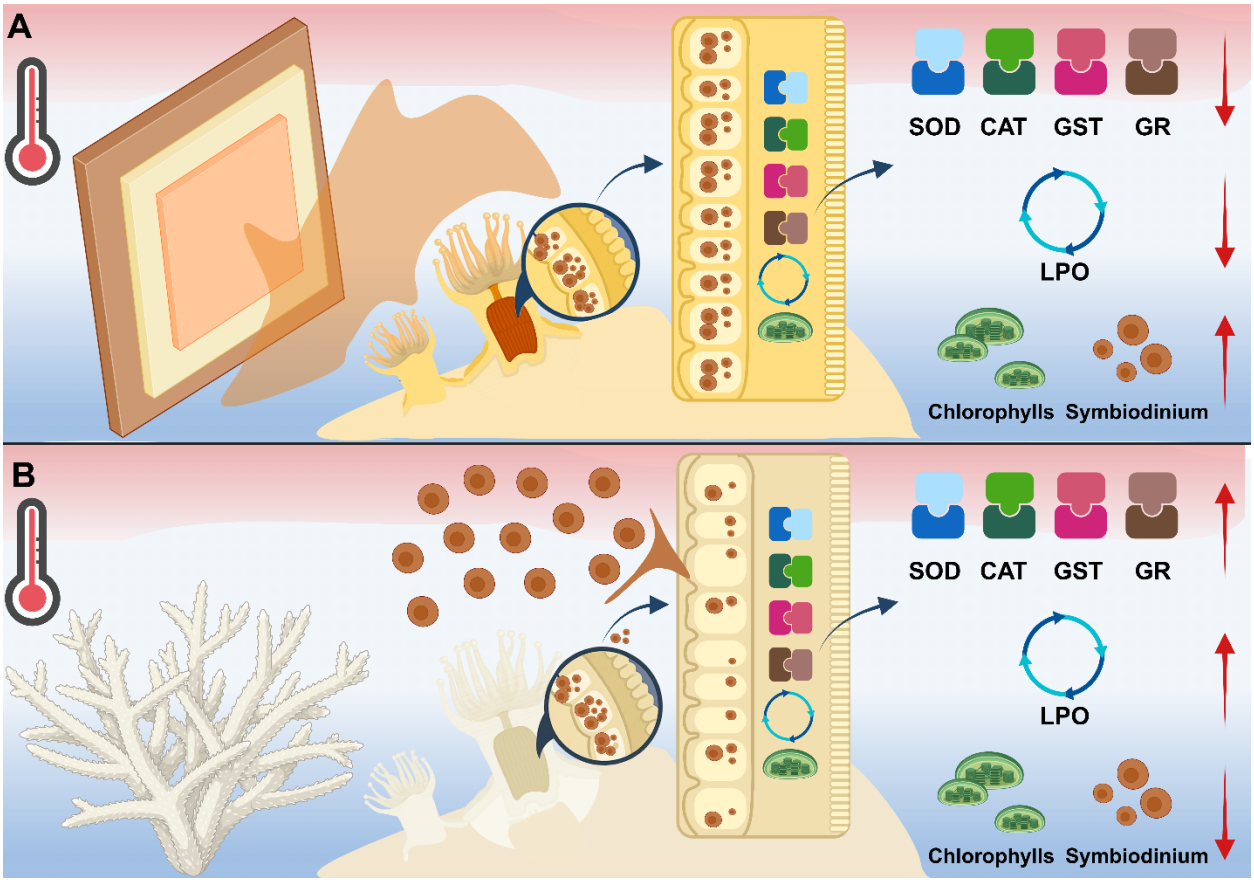

Figure 2.14. Schematic representation and summary of the effects of the heat stress model on heat stress's major biomarkers, including chlorophylls, Symbiodiniaceae, antioxidant enzymes (SOD, CAT, GST, GR), and lipid peroxidation (LPO). **A)** *In vivo* application of the antioxidant three-layered underwater film

system. From left to right, the absorption of cur-βCD within coral cells is shown. A hypothetical schematic cross-section of coral tissue includes a magnified view of the gastrodermis and symbiosomes, illustrating the potential intracellular effects of curcumin on the selected biomarkers. **B)** Schematic condition without the application of the drug delivery system, showing the hypothetical intracellular effects of heat stress on the same biomarkers.

2.4 Discussion and conclusions

Morphological and chemical analyses confirmed the successful stratification of the three different layers of the system, while appearance and mechanical tests demonstrated solid resistance combined with good flexibility, suggesting potential applicability across different coral species.

When immersed in seawater, the system behaved like a hydrogel, absorbing water and showing strong ionic cross-linking likely due to interactions between carrageenan, chitosan, and seawater ions. Swelling and gel fraction data supported this hypothesis, while viscoelastic analyses confirmed that higher absorption correlated with a lower elastic modulus. This property is particularly relevant, enabling efficient drug release without compromising structural integrity.

Each layer was engineered to degrade at distinct rates, thereby enabling a continuous and gradual release of curcumin, which was incorporated into the first two layers of the film. As demonstrated, the hydrophobic zein-based third layer allowed the directional diffusion of the majority of the drug, facilitating the targeted delivery of the antioxidant directly to the coral, potentially maximizing therapeutic efficacy, while minimizing dispersion into the surrounding environment. This approach is critical in controlled aquarium settings and especially relevant for future field applications in coral nurseries. To further support the employment of this material in real open field conditions, its complete biodegradability was investigated to ensure that once applied, it does not become a

persistent pollutant, in contrast with plastic-based objects widely used in coral restoration, and opens up to a one-shot eco-friendly application without the need for retrieval.

ABTS assays confirmed the antioxidant activity of the curcumin complex, and biodegradability tests validated the environmental compatibility of the system.

The film's biocompatibility and efficacy were tested *in vivo* at Genoa Aquarium using a four-phase bleaching model on *Stylophora pistillata*. The system was positioned near coral nubbins without direct skeletal contact, allowing curcumin to diffuse gradually. Treated corals tolerated thermal stress better than controls, as shown by higher chlorophyll content, greater Symbiodiniaceae density, and lower LPO production, all of which are reliable biomarkers of stress and ROS damage.

The model induced strong but reversible bleaching, allowing meaningful comparison between treated and untreated corals and confirming the protective effect of the film. Long-term stability, ease of deployment, and compatibility with different coral morphologies make this multilayer design a promising therapeutic tool. After being thoroughly tested on corals in aquaria, with no macroscopic side effects observed (no mucus production, no necrosis), preliminary field trials in the Maldives on *Acropora* and *Porites* corals (see **Figure 2.15**) further suggested the material's stability and adhesion under real reef conditions, setting the foundation for broader *in situ* applications. Considering its natural and readily available composition and the described scalable fabrication process, the material can be produced and applied in different sizes and shapes. Moreover, in the direction of a large-scale application, the material is intended to be applied mostly in human-made structures, moving from aquaria to underwater architectures used for coral restoration.

In aquaria, it often occurs that corals stored in aquaria for exhibition or experimentation can undergo local bleaching due to the wrong exposure to the aquarium lights (both in terms of intensity and distance from the corals) [96–98]. As shown in this work, the three-layered material can be easily and effectively applied in the closed environment of the tanks to restore the normal homeostasis in colonies under stress or with local bleaching.

In a real "in-field" scenario, the three-layer can potentially be safely used by a diver operator in all the current structures already present at most coral restoration sites, such as nurseries, spiders, and underwater aquaria for micro-fragmentation [99], to be used in case of heat waves for prevention of bleaching or as a first-aid tool, as schematically shown in **Figure 2.16**. However, future steps should focus on field testing the materials to further adapt the technology to specific restoration sites and to account for environmental factors that may influence system performance, along with long-term monitoring. In coral nurseries, for instance, water currents and the distance from target colonies should be carefully considered to optimally position the delivery system and maximize therapeutic release and efficacy.

In summary, the functionalized three-layer film system demonstrated the ability to: (i) provide a tunable, continuous, controlled, and directional release of the curcumin–β-cyclodextrin complexed nanocarrier; (ii) effectively enhance coral thermal stress tolerance without requiring direct contact with the coral skeleton; and (iii) be easily adapted and applied across a range of coral morphologies both in aquaria and on field.

Thanks to its biobased polymer composition, tailored degradation profiles, antioxidant activity, and water-compatible design adaptable to different coral species, the three-layered underwater film system presented here emerges as a promising therapeutic tool to mitigate oxidative stress and support coral immune function during heat-induced bleaching events.

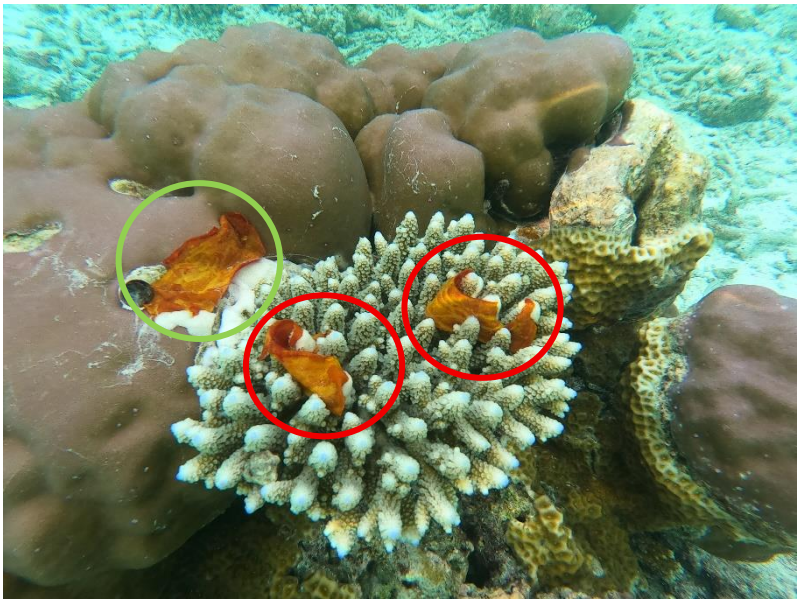

Figure 2.15 three-layered film system application in the Maldives on a boulder coral – genera *Porites* (green circle) and on a branching coral – genera *Acropora* (red circles).

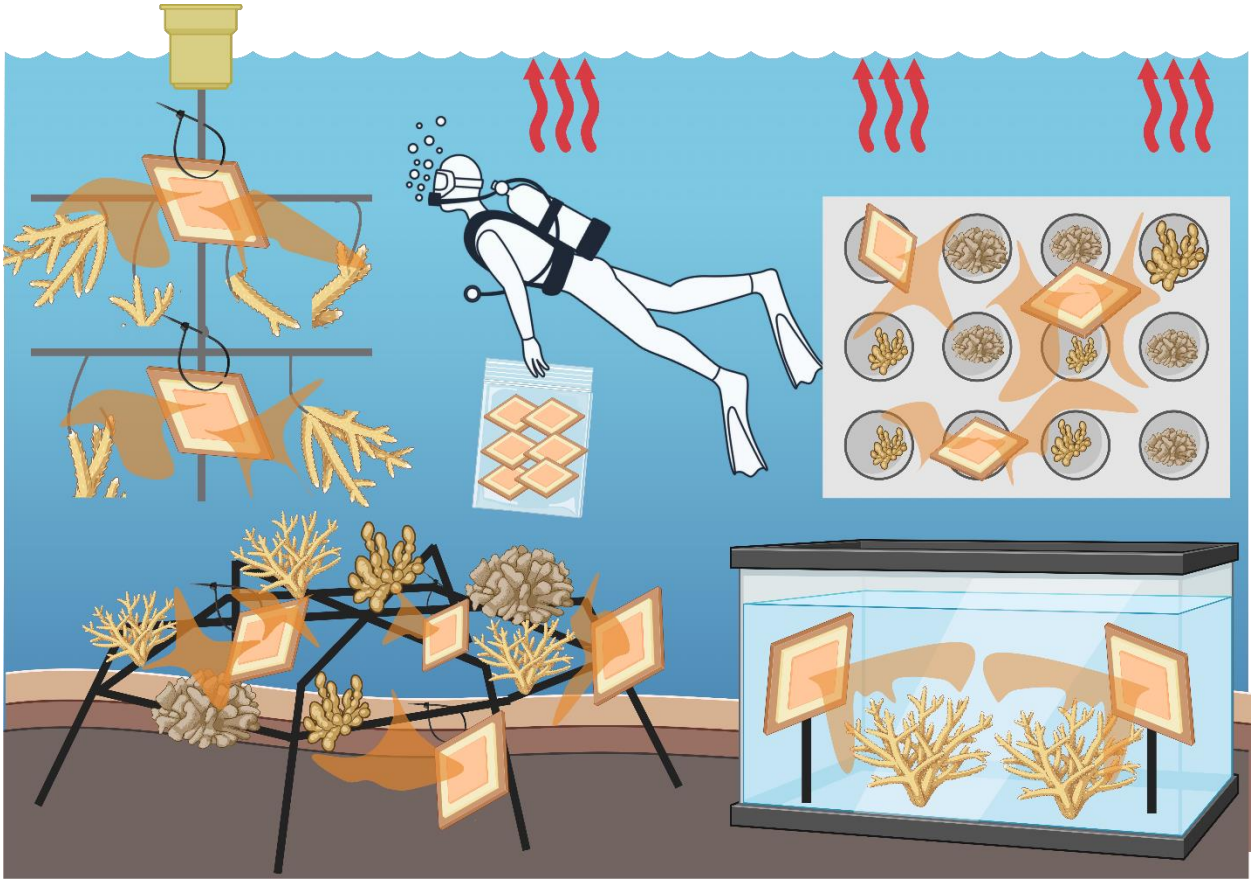

Figure 2.16 Schematic representation of the possible different uses of the three-layered underwater film system in outdoor coral restorations (nurseries, top left corner; spiders/reef stars, down left corner), microfragmentation (top right corner), and aquaria (down right corner).

Chapter 3: Antioxidant Microparticles

3.1 Engineering Silk Microparticles in Coral Bleaching Treatment: Bioinspired Underwater Vehicles for Curcumin Delivery

In response to the urgent call for innovative coral conservation strategies and the emerging use of cerium-based antioxidant nanoparticles, this study presents a novel approach based on curcumin-loaded silk fibroin microparticles (cur-silk-MPs) to mitigate thermal stress and enhance coral resilience. The therapy exploits the natural heterotrophic feeding behavior of corals through a bio-inspired, protein-based antioxidant delivery system designed to mimic coral prey in size, composition, and digestibility. In their natural environment, corals feed on a broad spectrum of plankton, from picoplankton (0.2–2 μm) to mesozooplankton (200 μm–2 mm), while in aquaria they are commonly fed brine shrimps (*Artemia salina*, ~500 μm). These dietary sources typically contain 30–70% protein by dry weight, indicating that corals can digest objects even at the macro-scale level [100,101].

Building on this principle, silk fibroin (SF) – a biocompatible protein derived from *Bombyx mori* silkworms [102]– was used to encapsulate curcumin from *Curcuma longa* [47,48], generating micrometric carriers (hereafter referred to as microparticles) tailored for controlled release. The shape of microparticles was carefully chosen to meet several desired characteristics, drawing on insights from drug delivery systems used in human therapies. Microparticles are indeed well-known for enabling controlled release, which enhances therapeutic effectiveness and reduces dosing frequency. They also allow targeted delivery, as they can be customized to localize specific sites, minimizing material waste and side effects. In this context, the use of microparticles provides an ideal technology to support biocompatibility with corals and a biomimetic approach [103,104].

Exploiting silk's unique mechanical properties, the proposed microparticles were customized by modifying the secondary structure of SF. They can be thermally modulated from an α-helix (water-soluble) to a β-sheet (water-insoluble) conformation, enabling tunable underwater drug release kinetics [105,106]. Two coral species were selected for in vivo testing: *Heliofungia fralinae* to assess microparticle digestibility and toxicity (dose–response), and *Stylophora pistillata* to evaluate their effectiveness in mitigating heat stress.

Biochemical analyses confirmed effective uptake and digestion of the microparticles, while molecular data demonstrated preserved chlorophyll content and Symbiodiniaceae density, enhanced antioxidant enzyme activity (SOD, CAT, GST, GR), and reduced lipid peroxidation (LPO) in treated corals. Altogether, these results highlight the potential of this eco-friendly, biomimetic drug delivery system to strengthen coral resilience in the face of ocean warming.

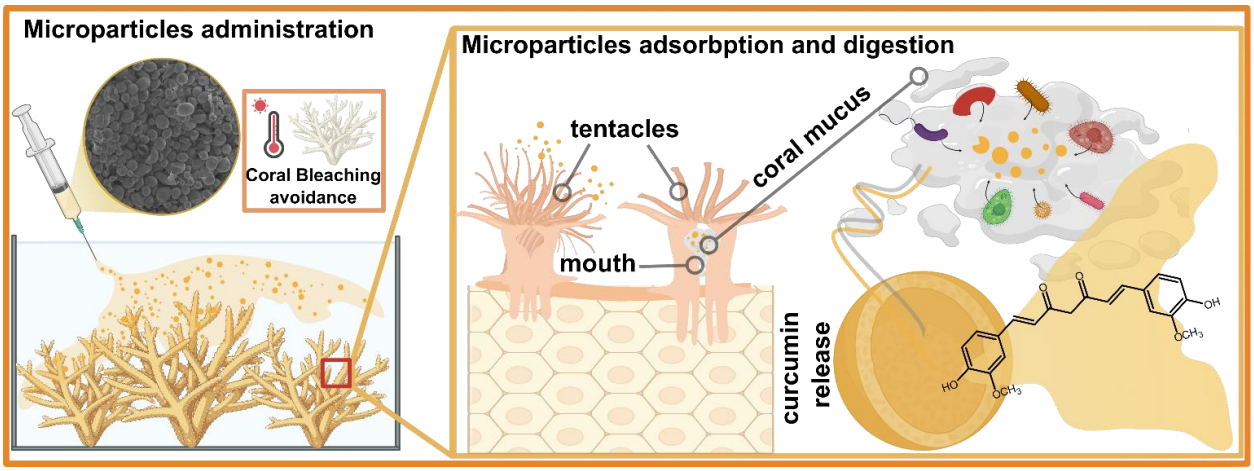

Figure 3.1 Schematic representation of curcumin-silk microparticle administration and hypothetical consequent adsorption and digestion to avoid coral bleaching.

3.2 Materials and Methods

3.2.1 Materials

Bombyx mori silkworm cocoons were purchased from Cantiere della Provvidenza SPA Scs Onlus (Belluno, Italy), Poly(vinyl alcohol) (PVA) (M_w = 30 000-70 000, 87-90% hydrolyzed), curcumin from *Curcuma longa* (turmeric) powder, and ethanol were purchased from Sigma-Aldrich. Sodium carbonate (≥ 99.0%) and lithium bromide (≥ 99.0%) were also provided by Sigma-Aldrich.

3.2.2 Silk fibroin extraction

Silk fibroin (SF) was extracted from *Bombyx mori* cocoons following Rockwood *et al*. [107]. Cocoons were cut and boiled in 0.02 M sodium carbonate (Na_2CO_3) for 30 minutes to remove sericin. The degummed fibers were rinsed three times in deionized water (20 min each) and dried overnight. Dried SF was then dissolved in 9.3 M lithium bromide (LiBr) at 60 °C for 4 hours. The resulting solution was transferred into dialysis tubing (Fisherbrand, vol/cm 9.3 mL), dialyzed against deionized water for 48 hours, and centrifuged twice (5 °C, 9,000 rpm, 20 min) to yield a 60 mg/mL silk solution, stored at 4 °C.

3.2.3 Silk – curcumin microparticles preparation

Microparticles were prepared using an emulsion-based method [108]. A fresh 50 mg/mL silk fibroin (SF) solution was made from the stored stock, while polyvinyl alcohol (PVA) was dissolved in deionized water at the same concentration. Silk and PVA were mixed at a 1:4 ratio under gentle stirring for 10–15 minutes. For curcumin-loaded particles, curcumin was added at 3%, 10%, or 15% (w/w relative to silk). The resulting emulsions were cast onto PDMS Petri dishes and air-dried into films, which were then cut and redissolved in ultrapure water to remove PVA. The suspension was centrifuged twice (5,000 rpm, 10 min, 4 °C); supernatants were discarded, and pellets resuspended in water each time. Final pellets were suspended in 20 mL ultrapure water at

4 °C and lyophilized (Christ Alpha 2-4 LSCplus), yielding both curcumin-loaded and empty microparticles. For clarity, empty microparticles are referred to as "**silk MPs**," while drug-loaded ones are labeled "**cur-silk MPs 3%," "10%,"** or **"15%**." All experiments, except SEM and ImageJ analysis, were performed using cur-silk MPs 10%. This decision was made based on encapsulation efficiency experiment results, where values were approximately 6 ± 0.3% for cur-silk MPs 3%; 30 ± 2% for cur-silk MPs 10%, and 15 ± 0.2% for cur-silk MPs 15%.

3.2.4 Post-fabrication treatment

After fabrication, cur-silk MPs 10% were thermally treated in a climatic chamber at 35 °C and 80% relative humidity overnight to induce the structural transition of silk fibroin from the water-soluble Silk I (α-helix - random coil) to the water-insoluble, β-sheet rich Silk II form. This conformational change enhances mechanical strength and water resistance, essential for underwater coral applications [109,110]. Given that the intended application of cur-silk MPs 10% involves underwater environments for coral treatment, achieving a Silk II conformation is crucial. The resulting β-sheet cur-silk MPs 10% were used in all subsequent analyses, including confocal microscopy, ABTS assays, and *in vivo* experiments.

Morphological analysis

3.2.5 Scanning electron microscopy

The morphology of the all obtained microparticles - silk MPs, cur-silk MPs 3%, cur-silk MPs 10%, and cur-silk MPs 15% - was analyzed by Scanning Electron Microscopy (SEM), using a variable pressure JOEL JSM-649LA (JEOL, Tokyo, Japan) microscope equipped with a tungsten thermionic electron source and working in high vacuum mode, with an acceleration voltage of 5 kV. The specimens were coated with a 10 nm thick film of gold utilizing a Cressington Sputter Coater – 208 HR (Cressington, Watford, UK).

The diameters of the microparticles were analyzed and determined by using ImageJ software. Approximately 100 measurements were taken to determine the mean diameter distribution of each type of microparticle.

3.2.6 Confocal microscope

Microparticles were analyzed using a Nikon A1 confocal microscope equipped with a 405 nm laser to assess whether the fluorescence properties of curcumin, which typically exhibits excitation around 420 nm and emission between 460 and 550 nm, were influenced by the fabrication process. A 1 mg/mL concentrated solution of β-sheet cur-silk MPs 10% in salty water was prepared and sonicated to destroy aggregates, enhancing microparticle visualization under a microscope. From 5 to 10 µL of cur-silk MPs 10% solutions were then placed on glass and covered with cover-glass for analysis. A 60x objective has been used. Furthermore, the same methodology was used to follow microparticle digestion inside the coral mucus.

3.2.7 Attenuated total reflection-Fourier transform infrared (ATR-FTIR) spectroscopy

Infrared spectra of Silk MPs and cur-silk MPs 10% were acquired by using an ATR accessory (MIRacle ATR, PIKE Technologies) with a diamond crystal coupled to an FTIR spectrometer (Vertex 70v FTIR, Bruker) in transmission mode using KBr pellets. Measurements were repeated for Silk MPs and cur-silk MPs 10% before and after climatic chamber treatment. All spectra were recorded between 4000 and 600 cm^{-1}, with a resolution of 4 cm^{-1}, accumulating 64 scans. Fourier self-deconvolution (FSD) of the infrared spectra covering the amide regions was performed by Opus 5.0 software to highlight differences between α-helix MPs and β-sheet MPs.

3.2.8 X-Ray diffraction

The physical state of silk MPs and cur-silk MPs 10%, both before and after climatic chamber treatment, was determined by X-ray diffraction spectroscopy. X-ray diffractograms were obtained using a Malvern PANalytical Empyrean X-ray diffractometer (Malvern Panalytical, Malvern, UK) equipped with a 1.8 kW Cu Kα source sealed in a ceramic tube, and a 0D Xe proportional detector with a PixCel 3D 2x2 area detector. The samples were placed on quartz support, and experiments were performed using a Cu Kα anode (λ = 1.5406 °A) operated at 45 kV and 40 mA from 5 to 65° 2θ. Again, deconvolution of the spectra covering the amide regions was performed by Opus 5.0 software to highlight differences between "before treatment" microparticles and "after treatment" microparticles.

3.2.9 Drug release

The curcumin release from cur-silk MPs 10% both before and after the climatic chamber was measured using a Varian Cary 6000i Scan UV–visible spectrophotometer (Walnut Creek, California, USA). Curcumin in seawater has a characteristic UV absorbance peak at 421 nm. At time zero, 6 mg of cur-silk-MPs before and after climatic chamber treatment were placed within a 2 x 2 cm dialysis bag (Fisherbrand dialysis tubing vol/cm 6.74 mL/cm wall thickness 28 µm 3.5 kDa MWCO) and immersed in 4 mL of salty water. This system created a controlled drug-release environment, as the dialysis bag acts as a semi-permeable membrane, partially mimicking *in vivo* conditions, also preventing sample agglomeration during the experiment, facilitating more accurate measurements. The dialysis bags were sealed, placed in 2 cm diameter circular Petri dishes, and immersed in 5 mL of saltwater. At each time point, 2.5 mL of solution was taken out and replaced with the same amount of fresh medium. All measurements were taken so that sinking conditions were maintained, and the validity of the Beer-Lambert law was reassured. The

experiments were carried out in triplicate, and the data were expressed as a cumulative percentage. The entire Petri was sealed with Parafilm tape to ensure no water evaporation occurred.

3.2.10 ABTS free radical cation scavenging assay

An ABTS (2,2′-azino-bis(3-ethylbenzothiazoline-6-sulfonic acid)) free radical cation scavenging assay was performed as described in Fadda *et al.* [60]. Three different concentrations of β-sheet cur-silk MPs 10% (1.0 mg/mL, 1.5 mg/mL, 3.0 mg/mL) were evaluated using the $ABTS^{\cdot+}$ solution. The decrease in absorbance was determined at 734 nm with a Varian Cary 6000i Scan UV–visible spectrophotometer (Walnut Creek, California, USA) at different times. All measurements were carried out in triplicate, and the results were averaged to obtain a mean value. Radical scavenging activity (RSA) was expressed as the inhibition percentage of free radicals of the sample and calculated by using **eq 2**:

$$radical\ scavenging\ activity\ (\%) = \frac{A_0 - A_1}{A_0} x100$$

where A_0 is the absorbance value of the control radical cation solution, and A_1 is the absorbance value of the sample at different time points. ABTS experiments were performed on cur-silk MPs after climatic chamber treatments only, since they were the ones selected for *in vivo* experiments on corals.

3.2.11 *In vivo* experiments – corals preparation and acclimation

In vivo experiments were conducted at the Genoa Aquarium to assess the digestibility, safety, and anti-bleaching efficacy of β-sheet cur-silk MPs 10%.

Heliofungia fralinae was used for digestion and dose-response tests, while *Stylophora pistillata* was selected for bleaching experiments. Corals were randomly chosen and acclimated in 12 L

tanks at 25 °C - *H. fralinae* for one week, and *S. pistillata* fragments for two weeks before thermal stress. All corals were fed daily and monitored for potential side effects throughout the study.

3.2.12 Coral Digestion Model of MPs

To study coral–microparticle interaction, *Heliofungia fralinae* specimens were used at the Genoa Aquarium due to their large oral opening (from a few millimeters to several centimeters in diameter), ideal for administering and monitoring microparticles. After climatic chamber treatment, 4 mg of β-sheet cur-silk MPs 10% were suspended in 1 mL of aquarium seawater and delivered directly into the coral's mouth via a Pasteur pipette. Mucus samples from the gastric cavity were collected at different time points - T0, T5, T15, T30, T45, and T60 minutes - using a micro syringe, then frozen with dry ice for analysis. Confocal microscopy was used to track microparticle presence and digestion. Parallel *H. fralinae* feeding trials with *Artemia salina* nauplii served as a digestion time reference and to assess the enzymatic activity of coral mucus.

3.2.13 MPs biocompatibility and dose

To assess the biocompatibility of β-sheet cur-silk MPs 10%, preliminary toxicity tests were conducted on *Heliofungia fralinae*. Following a toxicological approach [111], a dose–response experiment was designed in two phases: one-shot and multiple-shot administration. In both phases, three concentrations (1, 15, and 50 mg/mL) were tested on six coral specimens each (for a total of 18 corals/phase). In the one-shot phase, microparticles were administered on Day 1, and coral health was monitored for one week. In the multiple-shot phase, corals received repeated doses over a week, with follow-up observations continuing thereafter.

Coral length and mouth diameter were recorded for dose correlation, and unconsumed MPs were collected, dried, and weighed 30 minutes post-administration to estimate digestion efficiency. Coral health was visually assessed using a three-level stress scale: (1) fully open mouth, no mucus;

(2) slight closure, low mucus; (3) closed mouth, high mucus. Final coral status was evaluated one week post-treatment based on survival and bleaching occurrence.

3.2.14 Microparticles collection

Unconsumed β-sheet cur-silk MPs 10% from both one-shot and multiple-shot experiments, were collected to estimate the administration/digestion ratio for each coral specimen. To accelerate the evaporation of seawater, the vials containing unconsumed MPs were heated. The dried residue was then dialyzed using dialysis bags (Fisherbrand dialysis tubing vol/cm 6.74 mL/cm wall thickness 28 μm) to remove salts. After completing the dialysis process, the β-sheet cur-silk MPs 10% were dried overnight in an oven at 40°C in the presence of silica beads and then weighed.

3.2.15 Application on corals in Aquarium

Following the experiment of Santoro *et al.* [41], a new coral bleaching set-up has been developed to test β-sheet cur-silk MPs 10% efficacy in enhancing the heat stress tolerance of corals. The coral bleaching model was divided into four different phases: acclimation phase (T = 25°C), thermal stress phase (T increased by 0.5°C day by day), bleaching phase (31°C for a week), and the recovery phase (T decreased by 1°C day by day till 25°C). A total of 24 coral cuttings were acclimated for two weeks into a 3100 L tank of the tropical division of the Genoa aquarium and subsequently divided into two different tanks (12 per tank). In one tank, coral cuttings were treated with microparticles, while in the control tank, no treatment was performed. These experimental tanks have been placed in a water bath within a 400 L tank to regulate temperature and light better. For the light intensity, LED x coral light 50 W 10.000 K was used (11:13 h light dark 230 PA). After the acclimation time, the temperature was increased using a 300 W thermostatic heater (Schego, Germany). Water change within the tank was conducted every two days to avoid overproduction of algae. Inoculation of microparticles was conducted once a week with a

concentration of 1 mg/L. β-sheet cur-silk MPs 10% after climatic chamber treatment were used. Finally, sampling for further molecular analysis was performed at the end of each phase (3 coral nubbins each) for a total of 12 samples. During the entire coral bleaching set-up, tank cleaning was performed thrice a week, substituting 5 liters of dirty water with 5 L of clean water (previously warmed up when necessary). Microparticle administration was performed once a week, in correspondence with water change, by dissolving 12 mg of microparticles in salty water and using a pipette to reach all the coral nubbins within the tank. To avoid any additional stress, temperature increase/decrease, water change, and microparticle administration were always conducted at the same time in the morning, as precisely as possible. The coral bleaching experiment was designed to induce controlled stress in the corals without causing mortality. To achieve this, the experiment was halted at the first signs of localized bleaching, before the corals reached a fully bleached state. This approach ensured that the corals experienced stress sufficient to study their responses, but not to the extent that would lead to their death.

3.2.16 Coral Bleaching Assessment

The Coral Health Chart, developed by CoralWatch [112], was employed as a guideline to detect macroscopic colorimetric changes in corals and prevent their death. Even if photographs of the corals were taken with the reference card as background, this tool was not utilized to assess the health status of the corals in this study. Molecular analyses were conducted, instead, on coral samples at the end of each experimental phase. Quantifications of chlorophylls, Symbiodiniaceae density, and specific enzymatic activities were evaluated. These parameters were instrumental in determining the onset of thermal stress and assessing the efficacy of the β-sheet cur-silk MPs 10% in enhancing coral resilience.

3.2.17 Quantification of Chlorophyll *a* and *c2*

Coral tissue was removed from frozen fragments using airflow delivered through a 1000 µL pipette tip connected to a benchtop air pressure valve via a rubber hose, combined with 5 mL of ice-cold phosphate-buffered saline [61]. The resulting tissue slurry was homogenized and centrifuged at 3600g for 4 minutes. After removing the supernatant, the pellet was incubated in 100% acetone for 24 hours in the dark at 4 °C. Following extraction, the sample was centrifuged again at 3600g for 4 minutes, and the supernatant was used to determine Chl *a* and *c2* concentrations. Fluorescence readings at 630, 663, and 750 nm were applied to dinoflagellate-specific equations [62] and normalized to the coral surface area. The coral skeletons remaining after tissue removal were soaked in 10% bleach and left to dry for 48 hours. The surface area of each fragment was measured using the paraffin wax dipping method [63]. The change in weight from the wax coating was compared against a standard curve generated with dipped clay cylinders of known surface area to calculate the skeletal surface area of each fragment.

3.2.18 Symbiodiniaceae density

Samples previously fixed in 4 % formalin were used to count Symbiodiniaceae cells from six independent hemocytometer (Improved Newbauer) counts under an optical microscope (Leica Company, France), as previously described [64]. Physical and cellular impact of environmentally relevant microplastic exposure on thermally challenged *Pocillopora damicornis* (Cnidaria, Scleractinia). Cell density was calculated from the surface area of the respective fragments [65].

3.2.19 Oxidative Stress Analysis

Protein Extraction

Coral fragments were crushed using a pre-chilled mortar and pestle, then transferred into tubes and homogenized in 750 µL of lysis buffer (50 mM Tris-HCl, pH 7.4, 150 mM NaCl, 10% glycerol,

1% NP40 detergent, 5 mM EDTA) supplemented with 1 mM phenylmethylsulfonyl fluoride (Sigma-Aldrich). An initial centrifugation step (5 minutes at 3000 rpm) was performed to separate skeletal components. The samples were then centrifuged a second time (15 minutes at 14,000 rpm, 4 °C), after which the supernatant was collected and immediately frozen at −80 °C for later analysis. The total protein content of each sample was quantified using the Bradford assay, with BSA serving as the standard for calibration curve generation.

Catalase Activity Assay

Catalase (CAT) activity was measured based on the enzyme's peroxidation function, following the method outlined by Bergmeyer and Graßl [67]. The reduction in H_2O_2 concentration was monitored spectrophotometrically at 240 nm using a Varian Cary 50 Scan spectrophotometer (Agilent Technologies). Enzyme activity is reported as units (U) per milligram of protein, where U corresponds to k, the first-order rate constant (min^{-1}).

Superoxide Dismutase Activity Assay

Superoxide dismutase (SOD) activity was measured following the method of Vance *et al*. [66]. SOD activity is determined by its ability to compete with ferricytochrome c for superoxide radicals (O_2^-) generated by the xanthine/xanthine oxidase system, inhibiting the reduction of ferricytochrome c. The reaction mixture included the following reagents (Sigma-Aldrich): 0.01 mM ferricytochrome c, 0.1 mM EDTA, 0.01 mM xanthine, and 0.0061 U xanthine oxidase, prepared in a final volume of 1 mL. Various sample volumes were added to the reaction mixture to achieve 50% inhibition of the reaction rate. The reduction of ferricytochrome c was monitored spectrophotometrically at 550 nm and 25 °C using a Varian Cary 50 Scan Spectrophotometer (Agilent Technologies). Under these conditions, one unit of SOD activity was defined as the amount of enzyme required to inhibit the

reduction of ferricytochrome c by 50%. Results are reported as units (U) of enzyme activity per milligram of protein.

Glutathione S-transferase activity assay

GST activity was assessed by considering the reaction of the enzyme with the 1-Chloro-2,4-dinitrobenzene (CDNB) substrate, according to Hayes and Strange [69]. The reaction solution (containing 200 mM potassium phosphate buffer pH 6.5, 20 mM CDNB dissolved in 95 % ethanol, and 20 mM reduced glutathione) was mixed in a 1 mL cuvette with different volumes of samples, and the formation of CDNB-oxidized glutathione conjugate was followed spectrophotometrically at 340 nm (Varian Cary 50 Scan spectrophotometer, Agilent Technologies). GST activity is expressed as units (U) of enzyme per mg of protein and is proportional to the increase in absorbance caused by conjugated product formation.

Glutathione reductase activity assay

The enzymatic assay of glutathione reductase (GR) was performed according to Wang et al. [70]. The activity of GR was evaluated through the spectrophotometric detection of the absorbance at 340 nm (Varian Cary 50 Scan spectrophotometer, Agilent Technologies) of NADPH oxidation to NADP+ reaction, which occurs in conjunction with the glutathione reduction, and is proportional to the decrease in absorbance over time. NADPH reaction was initially measured in the reaction mix (containing 0.1 M potassium phosphate buffer pH 7.6, 0.16 mM NADPH, 1 mg ml^{-1} BSA and 4.6 mM oxidized glutathione), and subsequently adding different volumes of sample. GR activity was obtained from the difference between the two absorbance values. One unit of GR activity is defined as the oxidation of 1 nmol NADPH/min at 25°C. Results are expressed as units (U) of enzyme per mg of protein.

Lipid Peroxidation

Lipid peroxidation levels were evaluated by measuring malondialdehyde (MDA) concentrations using a commercially available assay kit (Bioxytech LPO-586, Oxis International, USA). This method relies on the reaction between MDA and the chromogenic reagent N-methyl-2-phenylindole at 45 °C. Coral apex samples (~1 g each) were pulverized using a pre-chilled mortar and pestle and then homogenized in 1 mL of 20 mM phosphate buffer (pH 7.4). To prevent oxidation during processing, 10 µL of 0.5 M butylated hydroxytoluene in acetonitrile was added to each 1 mL homogenate. The homogenates were centrifuged at 3,000 × g for 10 minutes at 4 °C, and the supernatant was collected for protein quantification using the Bradford method.

The assay was performed following the hydrochloric acid solvent procedure provided by the kit's manufacturer. The absorbance of the resulting blue product was measured at 586 nm, as described by Gérard-Monnier *et al.* (1998) [71]. Results are expressed as µmol of MDA per µg of protein.

3.2.20 Statistics

Statistical analysis was performed using OriginPro (OriginLab). One-way ANOVA followed by Tukey's post-hoc test was used for group comparisons. Significance was set at $p < 0.05$ and marked with (*) in graphs.

3.3 Results

3.3.1 Characterization of Silk Microparticles

The microparticle production process is schematically reported in **Figure 3.2**. Specific materials, formulations, and mixing procedures are shown in **Figures 3.2A** and **3.2B**. The resulting solutions were cast onto PDMS-coated Petri dishes, and dried films were then cut and washed to remove PVA (**Figure 3.2C**). The final centrifuged suspensions were lyophilized to obtain microparticles,

as shown in **Figure 3.2D**. Four formulations of silk MPs were prepared with increasing curcumin concentrations: Silk MPs (empty), cur-silk MPs 3%, cur-silk MPs 10%, and cur-silk MPs 15% (the reported curcumin concentrations are expressed as w/w relative to silk). Successful curcumin encapsulation was visually confirmed by the intense yellow color of the MPs (**Figure 3.2D**). SEM analysis (**Figure 3.3A**) was used to assess MPs' morphology before and after thermal treatment in the climatic chamber (35°C, 80% Rh), used to modify the protein's secondary structure conformation from α-helix to β-sheet. The top images show the MPs before treatment, while the bottom images show the MPs after treatment. All formulations appeared uniform and rounded, with no morphological changes post-treatment. The mean dimensions of the MPs are reported in **Figures 3.4A** and **3.4B** and **Tables 3.1A** and **3.1B.** Dimensions are expressed as mean length instead of diameter since not all the obtained microparticles are completely spherical in shape. In detail, silk MPs averaged 7.5 ± 1.5 μm, while curcumin-loaded MPs ranged from 7.5 ± 3.5 μm to 8.5 ± 1.5 μm. Slight size variations were attributed to curcumin loading. **Figures 3.3B** and **3.3C** display the size distribution of cur-silk MPs 10% before and after thermal treatment, showing no significant changes, confirming that the treatment did not alter MPs' morphology. Given the optimal balance between drug content and MPs integrity, cur-silk MPs 10% were selected for subsequent experiments. To verify curcumin fluorescence post-encapsulation and use this property for particle tracking, confocal microscopy was performed (**Figure 3.3D**). β-sheet cur-silk MPs 10% exhibited clear fluorescence, confirming curcumin's retention and localization within the MPs. Transmission and merged images further validated its internal distribution.

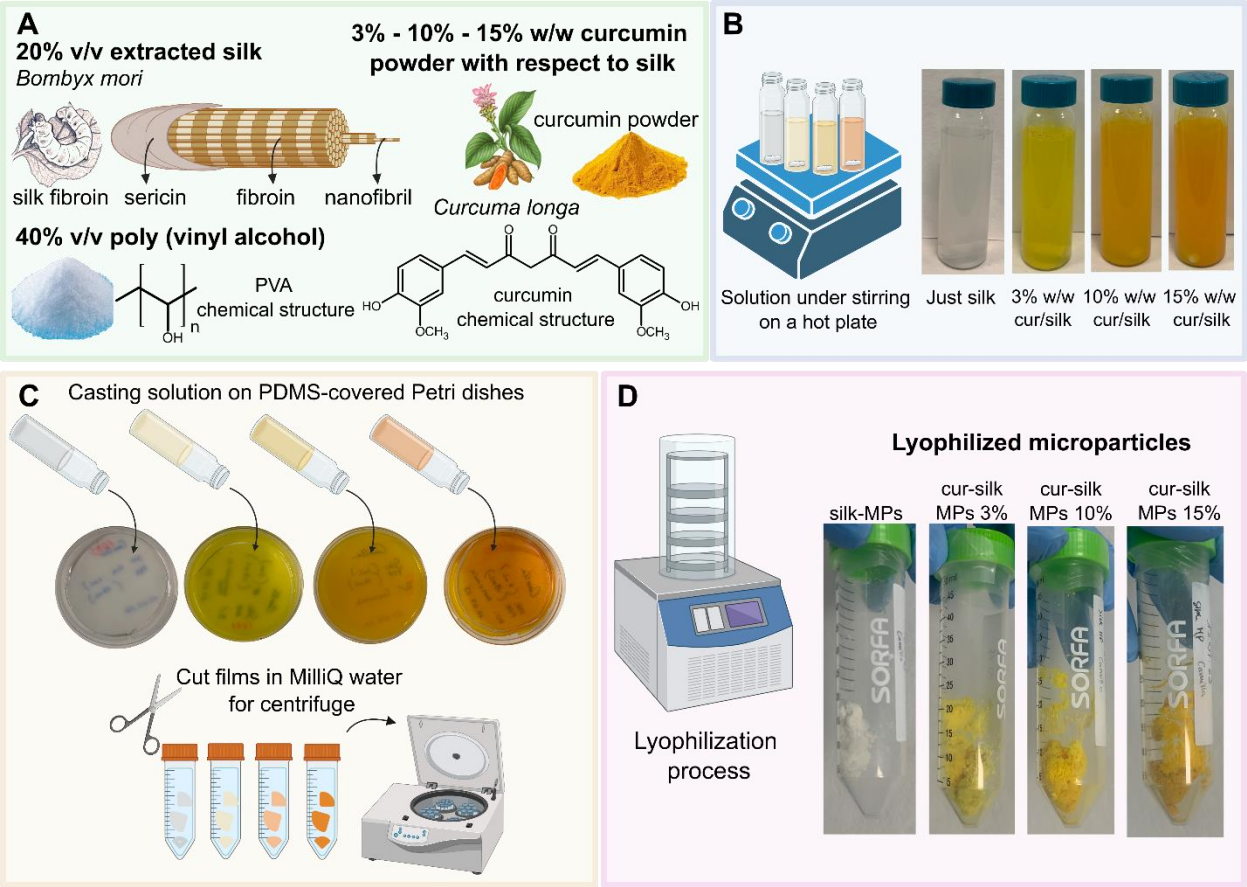

Figure 3.2 Schematic representation of the preparation of silk microparticles. **A)** different components of the final microparticles with relative concentrations; **B)** stirring procedure for solution preparation; **C)** solvent casting method and further centrifugation step; **D)** final lyophilization process for dried microparticles production.

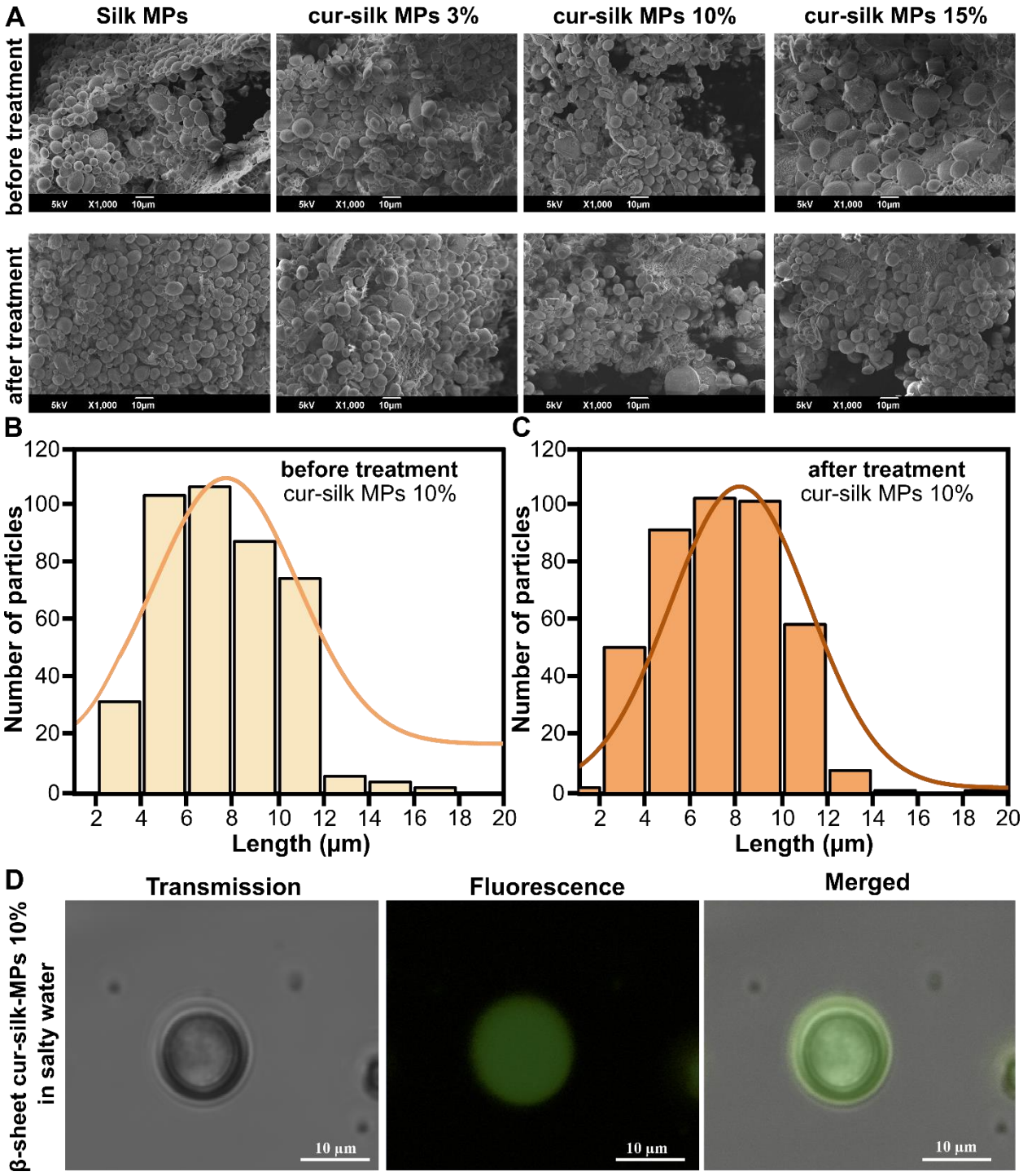

Figure 3.3 Morphological analysis of the obtained microparticles. **A)** SEM images of silk MPs, cur-silk MPs 3%, cur-silk MPs 10%, and cur-silk MPs 15% before the climatic chamber (up) and after (down). **B)** and **C)** Size Distribution of cur-silk MPs 10% before and after the climatic chamber, respectively. **D)**

Confocal microscope acquisitions of β-sheet cur-silk MPs 10% using transmission, fluorescence, and merged channels.

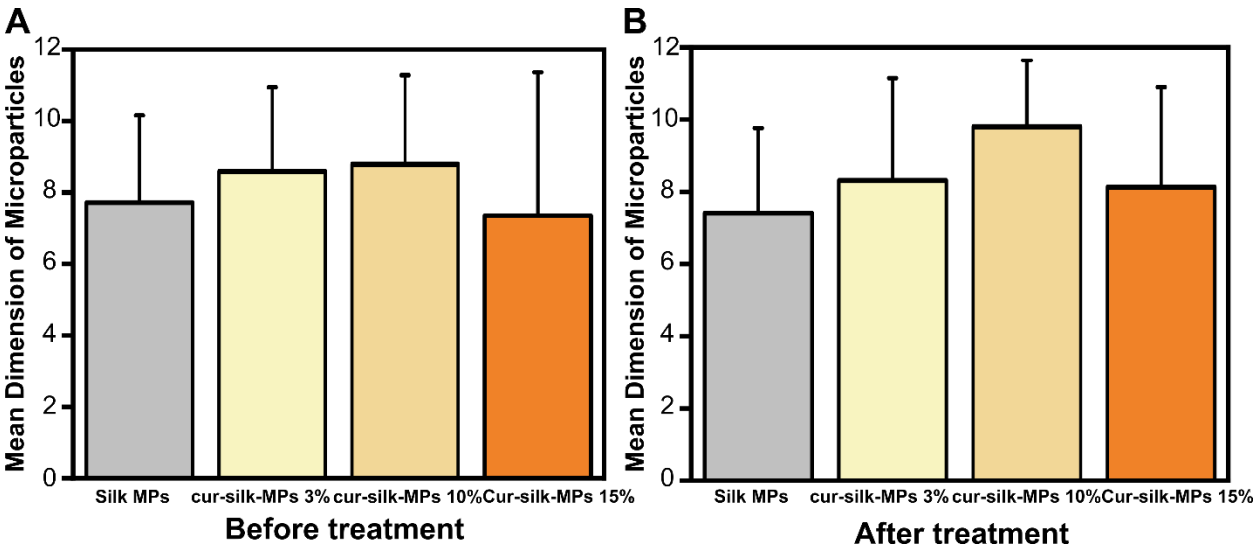

Figure 3.4 ImageJ analysis from SEM images. Mean dimension of silk microparticles divided by categories **A)** before treatment within the climatic chamber and **B)** after treatment within the climatic chamber.

A.

Before treatment	Mean Length (µm)	SD	Minimum	Maximum
Silk – MPs	7.7244	1.8088	2.931	12.238
Cur – Silk MPs 3%	8.39753	1.5844	2.683	11.481
Cur – Silk MPs 10%	8.763	1.515	2.531	10.469
Cur – Silk MPs 15%	7.292	3.788	1.935	20.465

B.

After treatment	Mean Length (µm)	SD	Minimum	Maximum
Silk – MPs	**7.805**	**1.8448**	**2.375**	**11.033**
Cur – Silk MPs 3%	**8.2869**	**1.9376**	**1.256**	**13.322**
Cur – Silk MPs 10%	**9.9353**	**2.1614**	**2.354**	**19.956**
Cur – Silk MPs 15%	**8.1791**	**1.8303**	**2.286**	**10.503**

Table 3.1 Table of Mean Length, standard deviation, minimum, and maximum length of silk microparticles divided by categories. **A)** before treatment within the climatic chamber and **B)** after treatment within the climatic chamber.

3.3.2 Physiochemical characterization

The physicochemical properties of silk can be tailored by modifying its secondary structure, following established protocols [105], to produce materials with tunable performance. **Figure 3.5** summarizes the properties of the MPs before and after thermal treatment.

Specifically, FT-IR spectroscopy was employed to analyze the chemical and conformational changes in silk-based MPs. Full spectra for silk MPs, pristine curcumin, and cur-silk MPs 10%, before and after treatment, are shown in **Figures 3.6A** and **3.6B**. As expected, silk MPs (black lines) exhibited characteristic protein vibrational modes, such as the Amide I, II, and III [113], while curcumin (red lines) displayed its typical vibrational peaks [114]. Cur-silk MPs 10% (blue lines) showed overlapping peaks from both components.

To study structural transitions, silk MPs were used as a reference instead of cur-silk MPs 10% due to curcumin's strong peaks that could interfere with interpretation. A similar approach was used by Contardi *et al.* [46] to study the conformational state of the protein zein. As shown in **Figure 3.5A**,

notable spectral shifts after thermal treatment were observed in the Amide I (1600–1800 cm^{-1}), II (1470–1570 cm^{-1}), and III (1250–1350 cm^{-1}) regions (highlighted in gray), which reflect protein conformational states [113]. Fourier self-deconvolution (FSD) of these regions (**Figures 3.5B** and **3.5C**) allowed quantification of structural changes, with peak assignments detailed in **Tables 3.2A** and **3.2B**. Precisely, a specific percentage can be assigned to each conformation based on the deconvolution of the peaks. Before treatment, silk MPs consisted mainly of α-helix (~50%), followed by β-sheet (~30%) and random coils (~10%) (**Table 3.2A**). After treatment, β-sheet content increased to ~50%, while α-helix dropped to ~5% and random coils rose to ~30% (**Table 3.2B**). This confirms that thermal exposure induces a conformational shift from α-helix to β-sheet, which is known to reduce solubility and prolong drug release [105].

To further assess structural changes, X-ray diffraction (XRD) spectroscopy was performed (**Figure 3.5D**). For the same reason as above, silk MPs were preferred over cur-silk MPs 10%. Peak assignments are shown in **Figures 3.5E** (before climatic chamber treatment) and **3.5F** (after climatic chamber treatment) [110]. During the deconvolution process, each peak was characterized by its Full Width at Half Maximum (FWHM). By utilizing additional parameters such as the X-ray wavelength, the Scherrer constant, and the angle at which the XRD measurements were performed, the crystallite size can be calculated using the Scherrer equation (all relevant data and the equation are provided in **Table 3.3**). Specifically, the crystallite size of the MPs before exposure to the climatic chamber was found to be 3.03 nm, while it increased to 5.26 nm after climatic chamber treatment. These results further confirm the successful thermal transition from α-helix to β-sheet conformation. A smaller crystallite size typically indicates more disordered, flexible coil-like structures characteristic of α-helix silk, whereas larger crystallite sizes are generally associated with rigid, ordered structures typical of β-sheet silk [110].

For clarity, from this point forward, cur-silk MPs 10% before treatment are referred to as **"α-helix cur-silk MPs 10%"**, and those after as **"β-sheet cur-silk MPs 10%."**

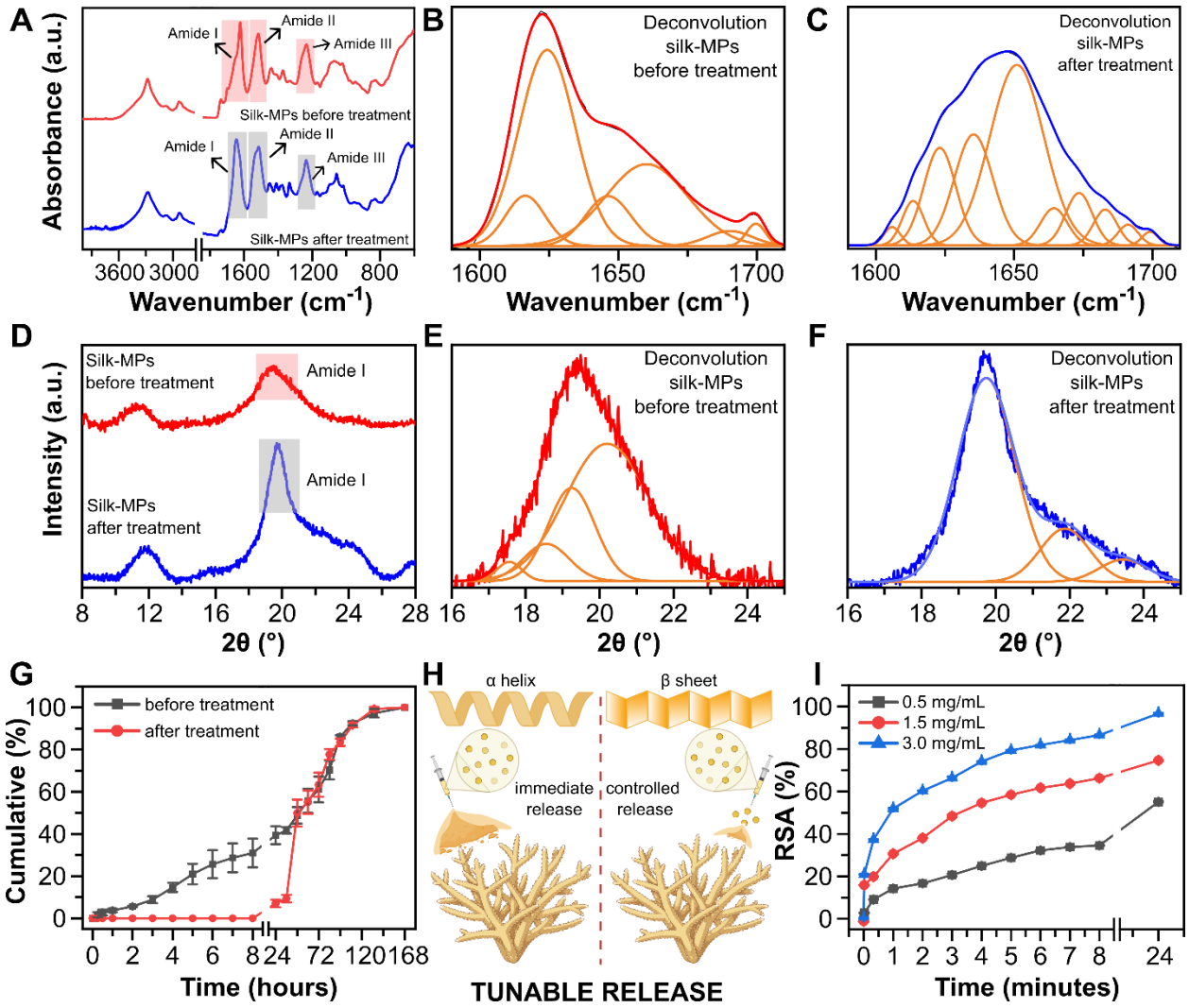

Figure 3.5 Physicochemical and functional characterization of the developed system. **A)** Silk MPs FTIR spectrum before and after the treatment in the climate chamber. The squares and the arrows highlight the region of Amide I, II, and III; A bigger and detailed description of the single spectra is shown in **Figure S3**. **B) C)** Fourier self-deconvolution (FSD) of the Amide I region for MPs before and after treatment, respectively. **D)** XRD spectra of silk MPs before and after the climatic chamber; **E) F)** relative peaks assignment to highlight the difference between amide I regions in silk MPs before and after the climatic chamber. **G)** Drug release curves of cur-silk MPs 10% before and after the climatic chamber. **H)** Schematic

representation of drug release profiles from α helix cur-silk MPs 10% (**left**) – immediate release underwater – and from β sheet cur-silk MPs 10% (**right**) – controlled release underwater. **I)** Radical Scavenging Activity of β-sheet cur-silk MPs over time.

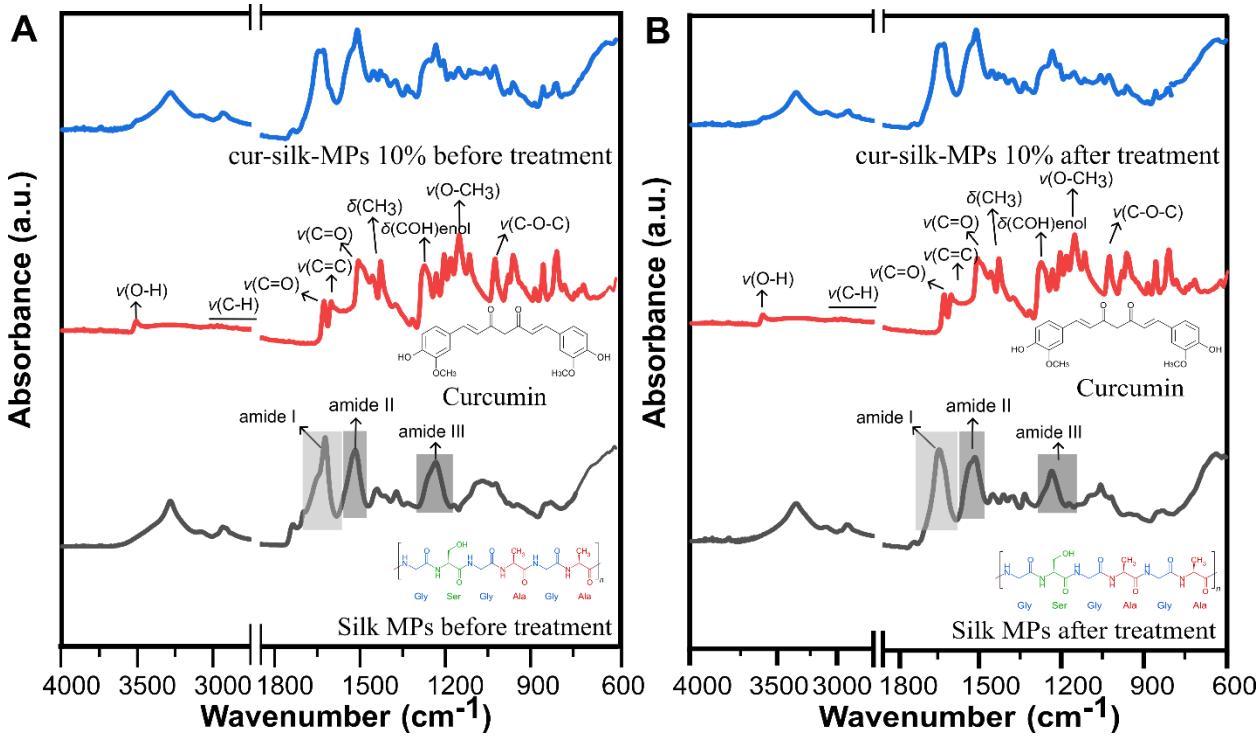

Figure 3.6 FT-IR spectrum of silk MPs, pristine curcumin, and cur-silk MPs 10%. **A)** before the climatic chamber and **B)** after the climatic chamber.

A.

Wavenumber range (cm $^{-1}$)	Assignment	Percentage (%)
1605 – 1615	(Tyr)	8.6
1616 – 1621	Beta – sheets (weak)[a]	29.59*
1622 – 1627	Beta – sheets (strong)[a]	
1628 – 1637	Beta – sheets (strong)[b]	
1638 – 1646	Random coils	9.82
1647 – 1655	Random coils	
1656 – 1662	Alpha – helices	49.08
1663 – 1670	Turns	2.92
1671 – 1685	Turns	
1686 – 1696	Turns	
1697 – 1703	Beta – sheets (weak) [a]	*

B.

Wavenumber range (cm $^{-1}$)	Assignment	Percentage (%)
1605 – 1615	**(Tyr)**	**1.34**
1616 – 1621	**Beta – sheets (weak)[a]**	**48.36***
1622 – 1627	**Beta – sheets (strong)[a]**	
1628 – 1637	**Beta – sheets (strong)[b]**	
1638 – 1646	**Random coils**	**33.91**
1647 – 1655	**Random coils**	
1656 – 1662	**Alpha – helices**	**4.47**
1663 – 1670	**Turns**	**11.91**
1671 – 1685	**Turns**	
1686 – 1696	**Turns**	
1697 – 1703	**Beta – sheets (weak) [a]**	*****

Table 3.2 Assignment of vibrational bands according to each chemical group and corresponding percentage for each MPs type. **A)** silk-MPs before treatment with the climatic chamber and **B)** silk-MPs after the climatic chamber treatment.

2θ = 20°			
X–ray wavelength (λ) = 0.15406 nm			
α – helix		**β – sheet**	
Peak	**FWHM**	**Peak**	**FWHM**
1	2.66797	1	1.53751
2	2.54123	2	1.56925
3	2.64812	3	1.48184
Scherrer equation: $D=\frac{k\lambda}{\beta\cos(\theta)}$	**k** = Scherrer constant, typically 0.9 **λ** = 0.15406 nm (x-ray wavelength) **β** = 0.02685 radians (converted FWHM) **θ** = 10°		

Table 3.3 Assignment of FWHM value for each peach coming from the deconvolution of both XRD measurements of α-helix and β-sheet silk-MPs.

3.3.3 Drug release and antioxidant properties

Drug release behaviors were evaluated for both α-helix-rich (pre-treatment) and β-sheet-rich (post-treatment) cur-silk MPs 10%. As shown in **Figure 3.5G**, the two formulations displayed distinct release profile: α-helix cur-silk MPs 10% showed steady diffusion, releasing 40–50% of curcumin within 24 hours while β-sheet cur-silk MPs 10% exhibited a delayed release, with no drug detected in the first hours, followed by a burst release of 40–50% after 32 hours (**Figure 3.7A** and **B,** respectively). By 48 hours, both types aligned in their release profiles, maintaining sustained diffusion over 7 days. This behavior can be explained by the increased β-sheet content, which has a higher affinity with hydrophobic drugs such as curcumin, slowing down the initial release [46].

Figure 3.5H schematically illustrates the underwater release of curcumin from both MP types, highlighting their tunable release rate. Planning a prolonged administration and considering their slower degradation, β-sheet cur-silk MPs 10%, were selected for all *in vivo* experiments.

To investigate the antioxidant capacity of the produced vehicle, the scavenging ABTS assay for the β-sheet cur-silk MPs 10% in three different concentrations was performed, and the results are displayed in **Figure 3.5I.** After 24 hours, all the tested concentrations showed an excellent percentage of radical scavenging activity (RSA). Specifically, 0.5 mg/mL concentration showed 50% of RSA, 1.5 mg/mL concentration showed 70% of RSA, and 3.0 mg/mL, the highest concentration, showed almost 100% of RSA.

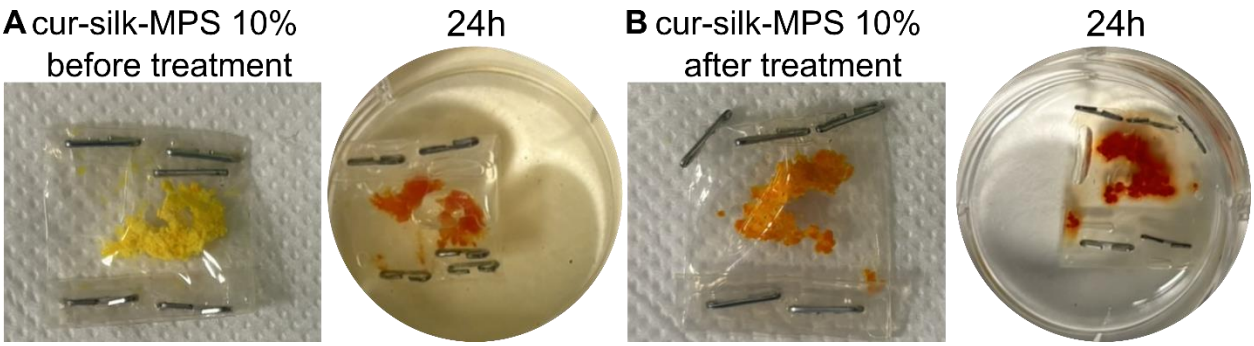

Figure 3.7 Dialysis bag from the drug release experiment after 24 hours submerged in salty water for both MP types. A) α-helix cur-silk-MPs 10% (before treatment) and B) β-sheet cur-silk-MPs 10% (after treatment).

3.3.4 Digestion of Curcumin-Silk Microparticles by Corals

One of the main challenges in drug delivery and precision medicine, following the effective encapsulation of a therapeutic agent, is to ensure its controlled and localized release upon reaching the intended target. In this study, the coral mouth is the delivery target, and the goal is to avoid premature release or loss of curcumin before microparticle uptake. The delayed release of curcumin, achieved via climatic chamber treatment of cur-silk MPs 10%, ensures that curcumin

remains encapsulated until the microparticles are ingested by the coral, enabling targeted and efficient delivery to internal tissues. This strategy can minimize compound loss and enhance therapeutic precision within the coral organism.

Heliofungia fralinae corals were utilized due to their uniquely wide mouth as a model to study what occurs to the β-sheet cur-silk MPs 10% once injected or eaten by a coral. Curcumin's natural yellowish color and fluorescence were used to track the MPs inside the coral mouth. Photographs of an *H. fralinae* coral after different time points from the injection of β-sheet cur-silk MPs 10% are displayed in **Figure 3.8A**. The coral did not eject the MPs, and no signs of side effects such as mucus release were detected during the experimental time (60 min). This may suggest that corals recognized the materials as food-inspired, confirming a certain level of biocompatibility of the samples with the animal.

At each time point, the content of the coral mouth was extracted and analyzed under a confocal microscope. The mixture included β-sheet cur-silk MPs 10%, seawater, mucus, and native associated microorganisms. Images of the β-sheet cur-silk MPs 10% dispersed in the gastric content at different time points are shown in **Figure 3.8B**. Initially, the β-sheet cur-silk MPs 10% structure appears unaltered, and the fluorescent is localized inside them. After 15–30 minutes, unidentified structures appeared in the mucus. By 1 hour, MPs were no longer distinguishable, and curcumin fluorescence appeared dispersed, indicating digestion and release.

To double-check the digestion capacity of this extracted gastric content and to have a reference of a typical coral food, the same analysis was carried out by injecting *Artemia salina* nauplii, and the results are reported in **Figure 3.9**. *A. salina* nauplii digestion was analyzed by an optical microscope, thanks to its size (500 μm – 1 mm) and since it does not exhibit fluorescence features. The outcomes demonstrate how this substrate was digested by the coral's mucus within 60 minutes.

Similar digestion time was described by Hii, Soo, and Liew [101] in their study on the feeding behavior and efficiency of the coral *Galaxea fascicularis* (commonly known as octopus coral) when offered *A. salina* nauplii under controlled conditions. Indeed, it was observed that after 180 minutes of feeding, no *A.* nauplii remained in the corals' gastrovascular cavities, indicating that the corals had likely digested the majority of the prey by that time.

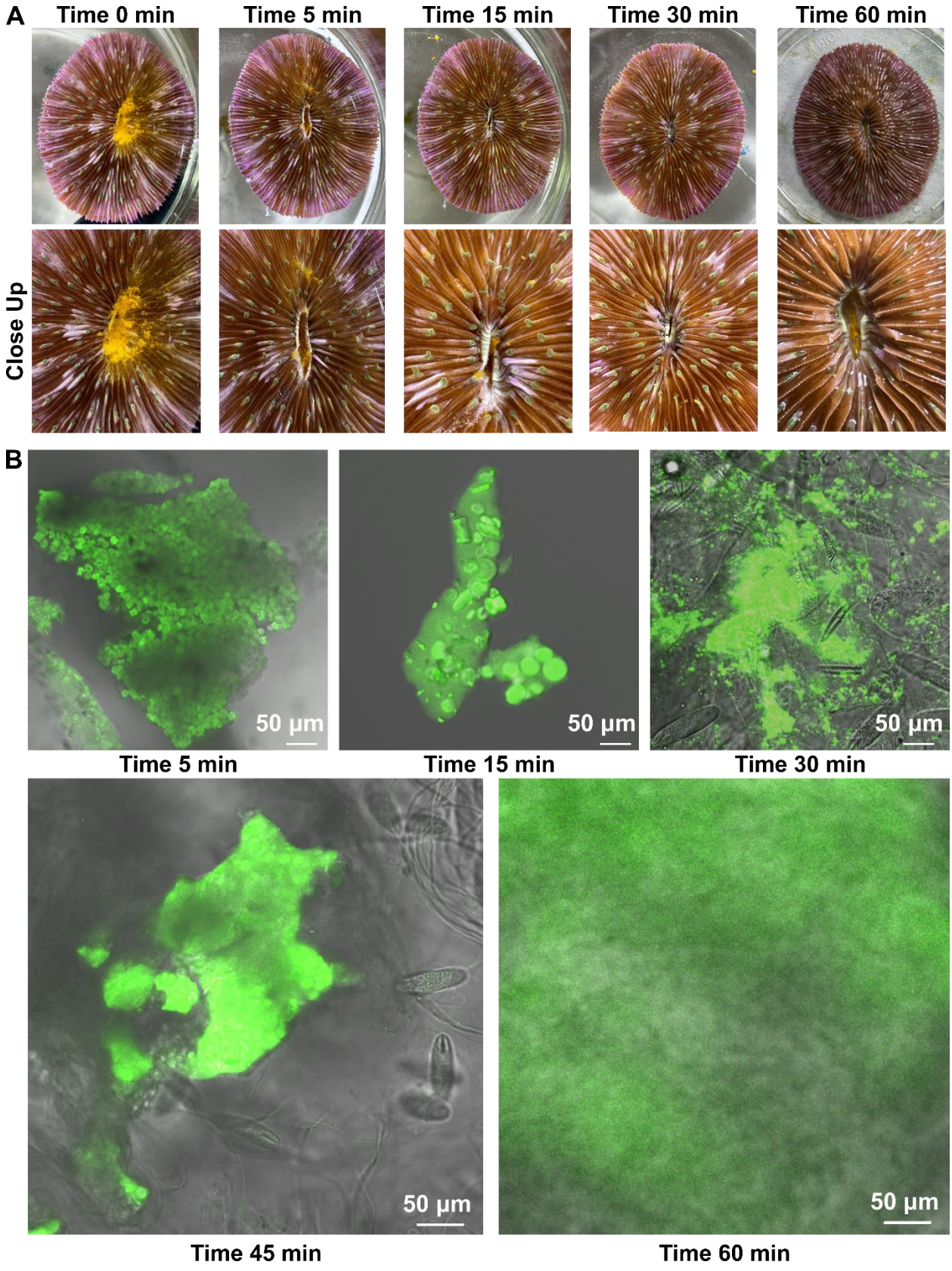
A
Time 0 min
Time 5 min
Time 15 min
Time 30 min
Time 60 min
Close Up
B
50 µm
Time 5 min
50 µm
Time 15 min
50 µm
Time 30 min
50 µm
Time 45 min
50 µm
Time 60 min

Figure 3.8 Microparticles administration and digestion experiment with *Heliofungia fralinae* corals. **A)** Photographs of *H. fralinae* coral and its gastric cavity at different magnifications and time points of the digestion experiment. **B)** Confocal Microscope images of β-sheet Cur-Silk MPs within coral mucus withdrawn during the different time points of the digestion experiment.

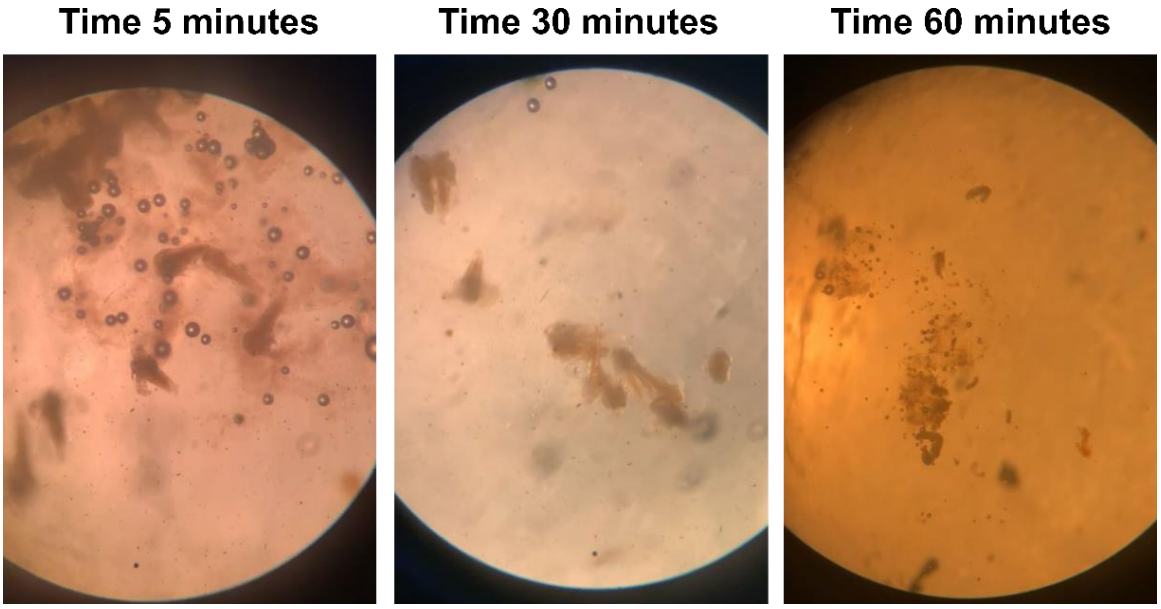

Figure 3.9 Microscope images of *Artemia salina* nauplii being digested by coral mucus during time.

3.3.5 Biocompatibility and toxic dose

Biocompatibility is the first goal for any type of vehicle that should interact with a patient, in this case, corals. However, whether a drug therapy has beneficial or toxic effects depends on the administered dose, which must be assessed over time. To evaluate the potential macroscopic toxicity of β-sheet cur-silk MPs 10%, two experiments were conducted: a single-dose (one-shot) and a repeated-dose (multiple-shot) administration. In both experiments, three concentrations of MPs (1, 15, and 50 mg/mL) were administered to eighteen *Heliofungia fralinae* corals. During the one-shot administration, microparticles were delivered just once, while in the multiple-shot administration, microparticles were delivered every three days for a total of three applications (**Figure 3.10A**).

To estimate digestion efficiency, unconsumed, in excess, MPs were collected, dried, and weighed 30 minutes post-administration. It was found that most MPs were ingested at 1 and 15 mg/mL (~100% and ~80%, respectively), while only 50% uptake was observed at 50 mg/mL (**Figure 3.10B**), suggesting corals may regulate intake based on dose, possibly linked to their size or stress response.

To assess post-administration stress, mucus production and mouth closure were evaluated immediately after exposure to MPs. As shown in **Figure 3.10C**, most corals showed no adverse effects, with only minor mucus or partial closure in a few cases. All thirty-six corals survived. However, in the multiple-shot group, mild local bleaching was observed at 15 mg/mL (n = 1) and more frequently at 50 mg/mL (n = 3), shown in **Figure 3.10D** and visually in **Figure 3.11C**.

The experimental outcomes indicated that at the lowest dose (1 mg/mL), no signs of bleaching or mortality occurred on corals after either single or multiple exposures, with 100% uptake of MPs. The intermediate dose (15 mg/mL) also showed no major issues, though one coral showed slight stress after repeated exposure. In contrast, the highest dose led to reduced uptake and signs of stress. Nevertheless, no lethal dose was identified for *Heliofungia fralinae*, suggesting a favorable biocompatibility and tolerance of curcumin even at elevated concentrations. To avoid overloading and potential expulsion, 15 mg/mL was established as the theoretical maximum effective dose. Based on these results, a therapeutic range of 1–15 mg/mL for short- to long-term treatments can be hypothesized for this coral species.

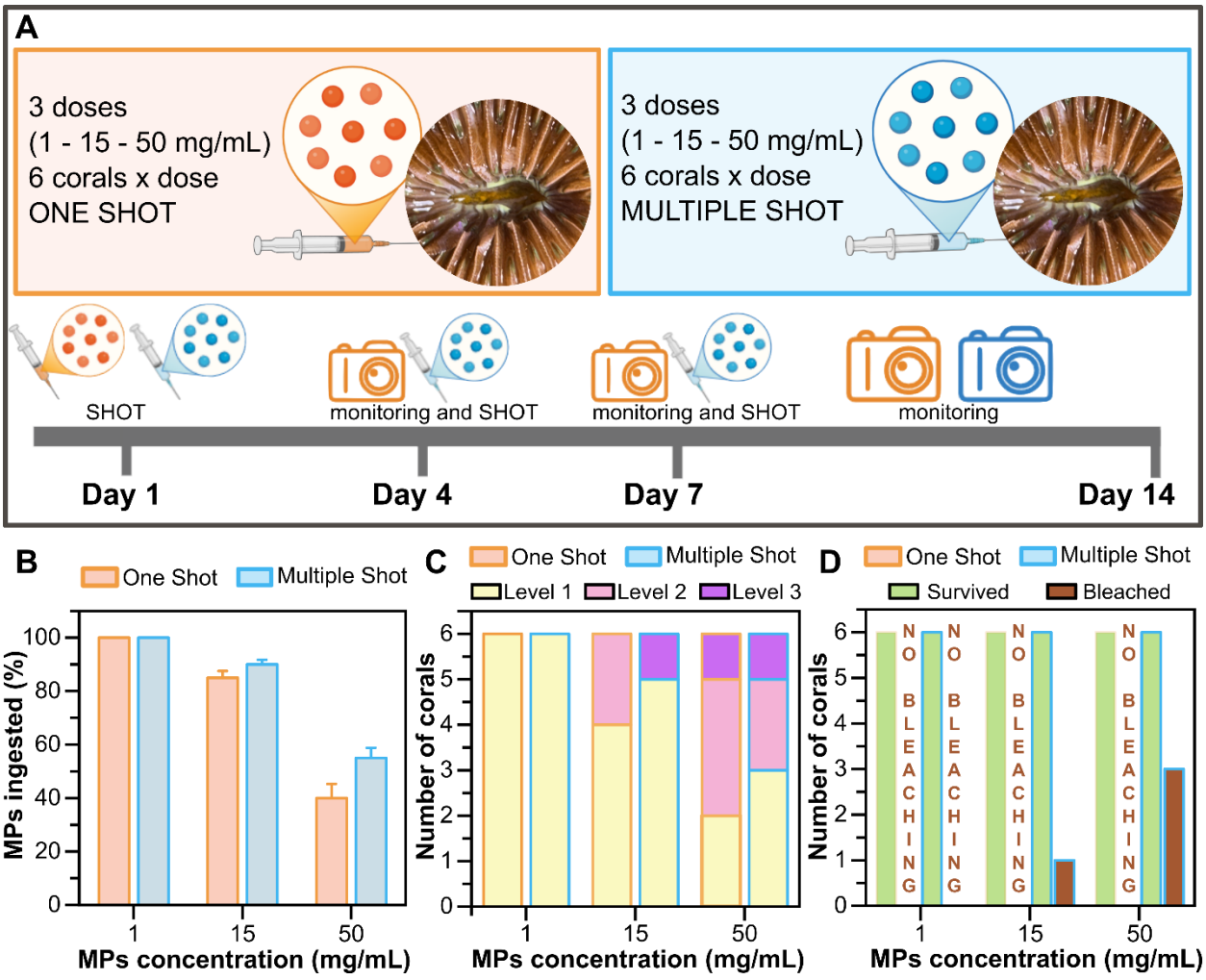

Figure 3.10 Schematic representation of one-shot and multiple-shot experiments and relative results. **A)** One shot and multiple shot experimental set up and relative monitoring time line; **B)** dose/percentage of β-sheet cur-silk MPs 10% ingested by corals for both one-shot and multiple-shots experiments; **C)** β-sheet cur-silk MPs 10% dose/number of corals for each stress-level for both experiments, where stress level 1 = well-opened mouth, no mucus production; stress level 2 = slight closure of mouth, low mucus production; stress level 3 = fully closed mouth, high mucus production; **D)** β-sheet cur-silk MPs 10% dose/number of corals survived and/or bleached.

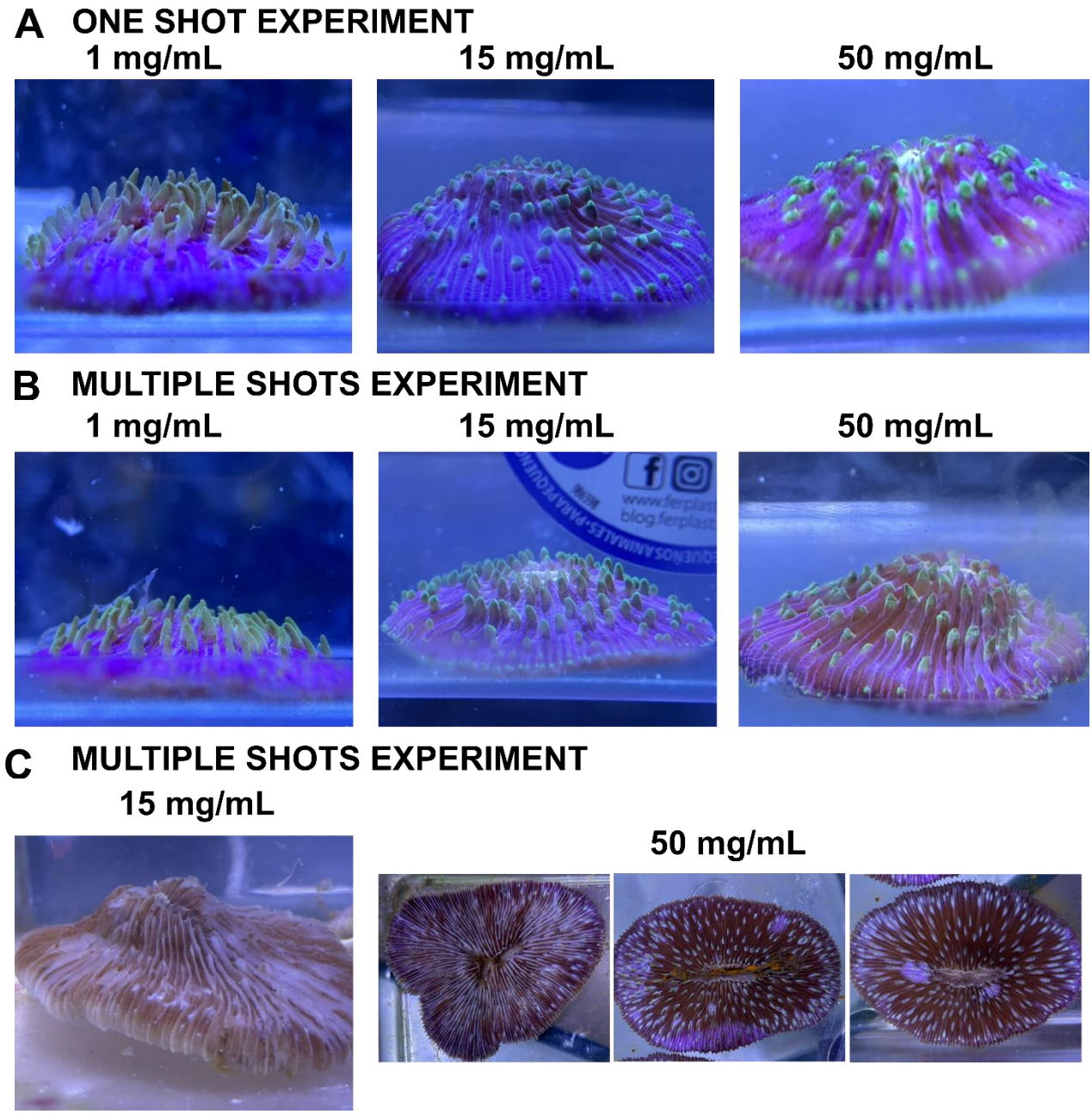

Figure 3.11 Representative *Heliofungia fralinae* corals during one-shot and multiple-shot experiments. **A)** shows a representative *H. fralinae* coral for each concentration during the one-shot experiment and **B)** during the multiple-shot experiment. **C)** Signs of local bleaching for 15 and 50 mg/mL concentration after the multiple-shot experiment.

3.3.6 Coral thermal stress test

A four-phase bleaching experiment was conducted on *Stylophora pistillata* nubbins to induce controlled thermal stress in corals, strong enough to elicit molecular differences between treated and untreated corals, without causing mortality or significant tissue loss. The experimental design is schematically illustrated in **Figure 3.12A**. Coral health was assessed by visually monitoring the organism's overall color and ultimately by evaluating physiological markers (chlorophyll content, symbiodiniaceae density, and enzymatic activity) at the end of each experimental phase. Representative coral fragments are shown in **Figure 3.12B**. Microparticle inoculation was initiated after a 7-day acclimation period at 25°C. Every time water was changed, microparticles were administered again to the corals during the following phases, as described in the Materials and Methods section. Corals were then subjected to a gradual temperature increase (0.5°C per day), reaching and maintaining 31°C for one week. At the peak stress phase, corals from the untreated control group exhibited visible skeletal whitening (highlighted in red), whereas those treated with MPs largely retained structural and visual integrity. During the recovery phase, in which the temperature was decreased by 1°C per day back to 25°C, control corals displayed small, localized bleaching patches, highlighted by red circles in photographs reported in **Figure 3.12B**. To contextualize these macroscopic observations, molecular analyses were performed.

3.3.7 Quantification of Chlorophyll *a* and *c2* – Symbiodiniaceae density

The health status of corals after the coral bleaching experiment was assessed by physiological and molecular analysis of samples collected at the end of each phase. Chlorophyll content and Symbioniaceae density represent crucial markers of bleaching status within coral cells. Results suggested important differences between the MPs-treated corals and untreated corals, especially during the bleaching phase. Specifically, in the case of chlorophylls, both chlorophyll a and chlorophyll c2 were significantly lower in control corals than in treated corals, with values of 6.3

± 0.2 µg/cm^2 and 8.1 ± 0.1 µg/cm^2 for chlorophyll a, and 1.5 ± 0.2 µg/cm^2 and 2.0 ± 0.1 µg/cm^2 for chlorophyll c2, respectively (**Figure 3.13A** and **3.13B**). For Symbiodiniaceae density, significant differences were observed between the two groups in both the bleaching and recovery phases, with values of 0.7 ± 0.06 x10^6 cells/cm^2 vs 1.0 ± 0.04 x10^6 cells/cm^2 in the bleaching phase, and 0.7 ± 0.04 x10^6 cells/cm^2 vs 1.0 ± 0.03 x10^6 cells/cm^2 in the recovery phase for control and treated corals, respectively (**Figure 3.13C**).

3.3.8 Oxidative Stress Analysis

Similarly, to quantify the level of oxidative stress, the levels of the four commonly involved antioxidant enzymes, Superoxide dismutase (SOD), Catalase (CAT), Glutathione S-transferase (GST), and Glutathione reductase (GR), were evaluated.

All tested antioxidant enzymes exhibited a similar trend across experimental conditions (**Figure 3.13 from D to G**). During the acclimation phase, enzyme activity levels were comparable between control corals and those exposed to microparticles. However, in the subsequent phases - heat stress, bleaching, and recovery - enzyme activity was generally higher in control corals compared to those treated with microparticles.

Notably, statistically significant differences were observed during the recovery phase for both SOD and CAT (**Figure 3.13D** and **3.13E**). In this phase, control corals exhibited significantly elevated enzyme activities compared to microparticle-treated corals, with values of ~ 0.70 ± 0.04 U/mg vs ~0.30 ± 0.03 U/mg for SOD, and ~0.05 ± 0.007 K/mg vs ~0.02 ± 0.003 K/mg for CAT ($p < 0.05$). On the contrary, no statistically significant differences were detected for GST and GR enzymes (**Figure 3.13F** and **3.13G**).

Finally, another important coral bleaching biomarker [71] - Lipid Peroxidation (LPO) - was evaluated. LPO reflects the structural integrity of the cell membranes, and production of LPOs

indicates that levels of ROS overwhelm the antioxidant pathways, accumulating and damaging cellular membrane lipids, thus signaling an ongoing oxidative stress [92 115]. During the acclimation and heat stress phases, the values for this parameter were similar between control corals and microparticle-treated corals. However, statistically significant differences were observed during the bleaching phase. Specifically, LPO values were significantly higher in control corals compared to microparticle-treated corals, with values of 0.22 ± 0.06 µM MDA/µg protein vs 0.10 ± 0.06 µM MDA/µg protein, respectively, as shown in **Figure 3.13H**.

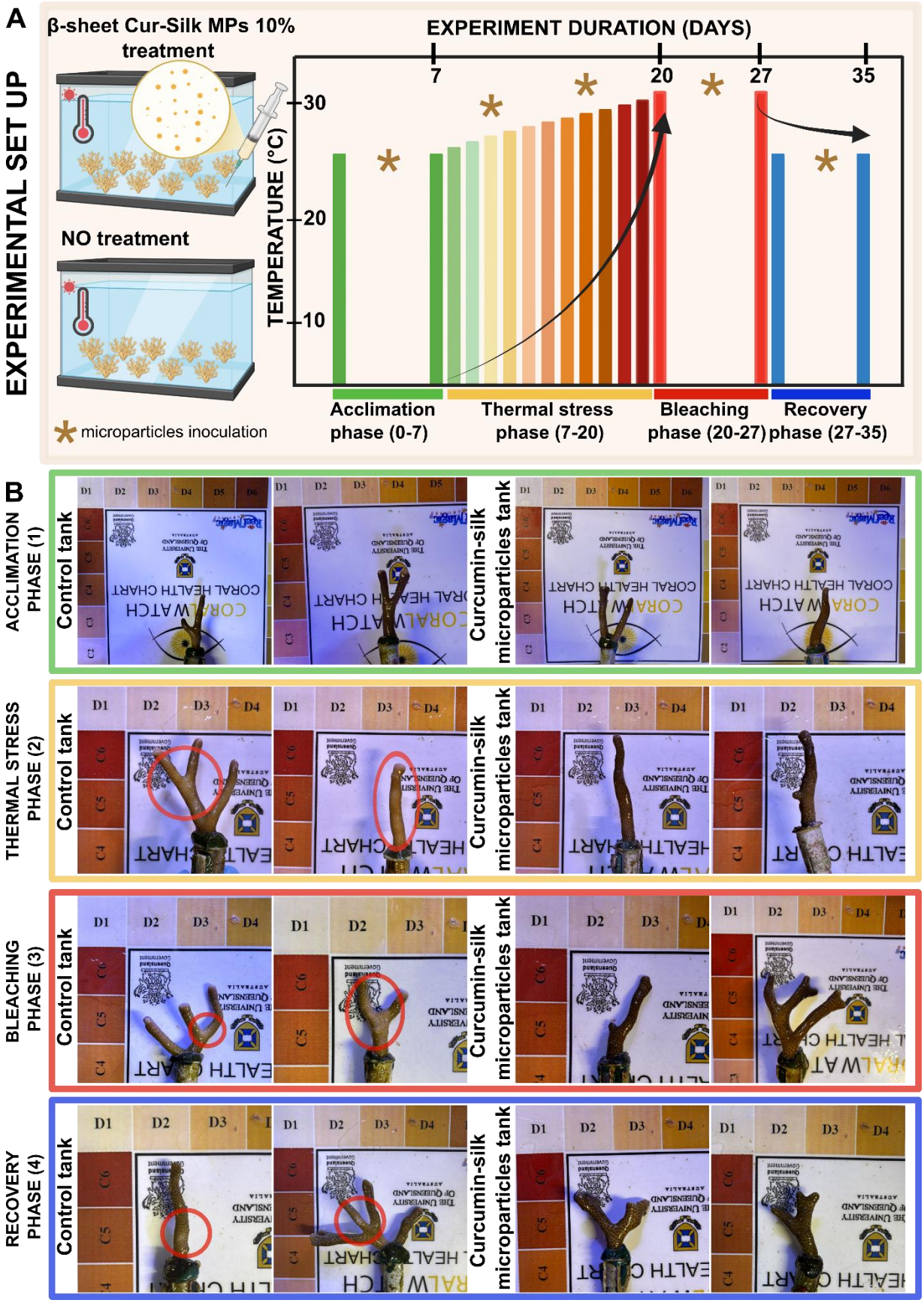
A
EXPERIMENTAL SET UP
β-sheet Cur-Silk MPs 10% treatment
NO treatment
microparticles inoculation
EXPERIMENT DURATION (DAYS)
7
20
27
35
TEMPERATURE (°C)
30
20
10
Acclimation phase (0-7)
Thermal stress phase (7-20)
Bleaching phase (20-27)
Recovery phase (27-35)
B
ACCLIMATION PHASE (1)
THERMAL STRESS PHASE (2)
BLEACHING PHASE (3)
RECOVERY PHASE (4)
Control tank
Curcumin-silk microparticles tank

Figure 3.12 Schematic representation of the coral bleaching experiment and representative coral fragments for each phase of the experimental setup. **A)** The different phases are visualized by colors, with green indicating the acclimation phase, yellow the thermal stress phase, red the bleaching phase, and blue the recovery phase; asterisks approximately represent MPs inoculation during each phase. **B)** At each phase, relevant comparisons among untreated control corals and microparticle-treated corals were highlighted by red circles, underlying the eventual whitening of the skeleton.

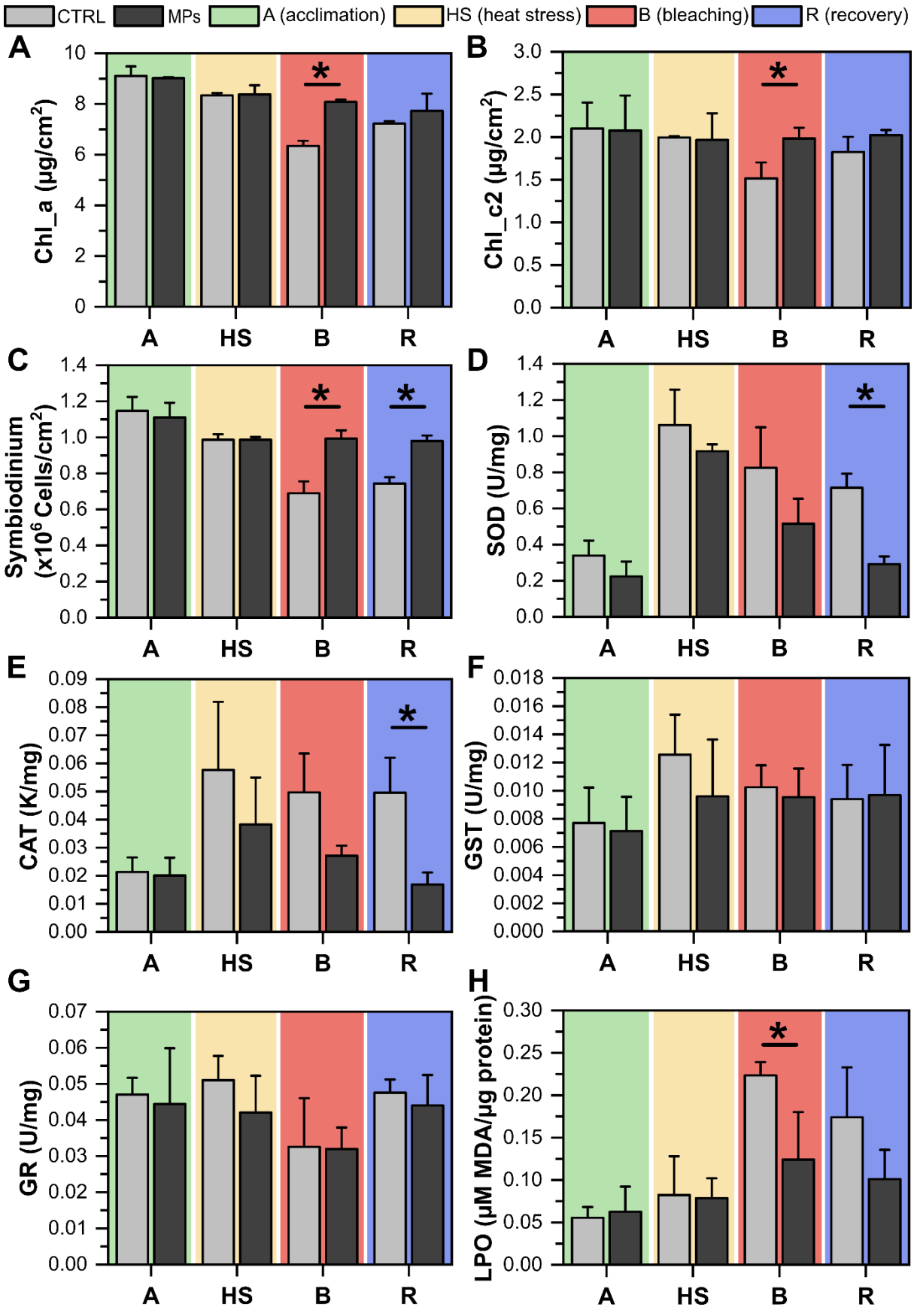
CTRL
MPs
A (acclimation)
HS (heat stress)
B (bleaching)
R (recovery)
A
Chl_a (µg/cm²)
B
Chl_c2 (µg/cm²)
C
Symbiodinium (x10⁶ Cells/cm²)
D
SOD (U/mg)
E
CAT (K/mg)
F
GST (U/mg)
G
GR (U/mg)
H
LPO (µM MDA/µg protein)
A
HS
B
R
*

Figure 3.13 Molecular analysis results following the coral bleaching experiment, comparing bleaching biomarkers and enzymatic activity between microparticles (MPs)-treated and control corals at each phase of the experimental setup. **A)** chlorophyll a *$p < 0.05$ CTRL vs MPs (bleaching phase P=0.00018), **B)** chlorophyll c2 *$p < 0.05$ CTRL vs MPs (bleaching phase P=0.022), **C)** Symbiodiniaceae cell density *$p < 0.05$ CTRL vs MPs (bleaching phase P=0.0027, recovery phase P=0.00094), **D)** SOD, *$p < 0.05$ CTRL vs MPs (recovery phase P=0.00115), **E)** CAT *$p < 0.05$ CTRL vs MPs (recovery phase P=0.012), **F)** GST, **G)** GR and **H)** LPO *$p < 0.05$ CTRL vs MPs (bleaching phase P=0.014).

3.4 Discussion and conclusions

Cur-silk microparticles (MPs) were fabricated at varying weight ratios, maintaining curcumin fluorescence, rounded morphology, stable dimensions (~8-10 μm diameter), and tunable silk fibroin structures. Among all the MPs formulations, Cur-silk MPs 10% were selected for the experiments. Thermal treatment induced a transition from water-soluble Silk I (α-helix) to water-insoluble Silk II (β-sheet), as confirmed by FTIR and XRD, enabling controlled curcumin release. In particular, β-sheet Cur-silk MPs 10% retained curcumin for at least 24 hours, allowing ingestion and gastric delivery before release, while preserving antioxidant activity as verified by ABTS assays. Digestibility tests on *Heliofungia fralinae* showed that MPs were ingested and processed within 30-60 minutes, with no lethal effects even at the highest dose (50 mg/mL). Although partial ingestion limits were observed at higher concentrations, overall survival and only mild stress responses indicated good biocompatibility. The food-like behavior of MPs suggests they are recognized and degraded through coral digestive pathways, consistent with the role of mesenterial filaments and mucus in proteolytic processing. Efficacy was further tested in *Stylophora pistillata* under sub-lethal thermal stress. While control corals exhibited significant reductions in chlorophyll and Symbiodiniaceae density, treated corals preserved higher algal content and photosynthetic

efficiency. Antioxidant enzyme analyses revealed lower SOD and CAT activity in treated corals, especially during recovery, suggesting reduced oxidative stress due to curcumin. No significant effects were seen on GST and GR, indicating potential enzyme selectivity. LPO assays confirmed lower oxidative damage in treated corals compared to controls. Together, these results demonstrate that curcumin delivered via silk-based MPs enhances coral resilience to heat stress by limiting ROS accumulation and preserving symbiont function. Beyond bleaching mitigation, this biomimetic system highlights the overlooked potential of heterotrophy in corals, offering a scalable, eco-friendly strategy for targeted delivery of antioxidant or other bioactives.

In conclusion, cur-silk MPs offer a drug delivery system for antioxidant therapy in corals that combines (i) biocompatibility even at high doses; ii) structural stability for sustained release; and iii) effective digestion and drug administration to the gastric cavity. This food-inspired platform not only offers a promising tool for coral bleaching prevention but may also serve broader applications in reef restoration and aquaculture. Although further optimization and field validation are required, the system's low cost, biodegradability, and possible scalability make it a valuable contribution toward sustainable coral conservation.

Chapter 4: 3D bioprinted hydrogel scaffold loaded with antioxidant microparticles

4.1 Spray-Dried Antioxidant Microparticles for Enhancing Symbiodinium Growth and Stress Tolerance in 3D Hydrogel Scaffolds

Building on the promising results obtained with antioxidant-based therapies for coral bleaching mitigation using underwater film systems and protein-derived microparticles, this study seeks to integrate these two approaches into a single platform. To do this, a novel polymeric drug delivery system was developed through a two-step process: the fabrication of antioxidant microparticles and their subsequent encapsulation within a hydrogel scaffold.

In the first stage, four different types of antioxidant-loaded microparticles were prepared using a spray-drying technique. Compared to previous methods, spray drying offers improved scalability, enabling rapid production of powder-form microparticles with minimal use of raw materials. Beyond silk fibroin and curcumin, additional natural antioxidants and biopolymeric carriers were explored. Specifically, sumac extract-loaded chitosan microparticles (**MP1**), curcumin-loaded silk microparticles (**MP2**), reduced-L-glutathione-loaded chitosan microparticles (**MP3**), and carminic acid-loaded carrageenan microparticles (**MP4**) were produced.

Besides curcumin – already described as a strong antioxidant compound from the *Curcuma longa* plant [48]– different drugs were considered for the other microparticles' formulations. Specifically, sumac from the *Rhus glabra* plant is a commonly used spice in Turkey, widely used as a drug in wound healing therapies for its strong antimicrobial and antioxidant capacities [116]; reduced-L-glutathione is the active form of glutathione, a small, water-soluble tripeptide composed of three amino acids (glutamate, cysteine, and glycine), known as one of the most important intracellular antioxidants found in both animal and plant cells [117]; while carminic acid

is a natural red pigment derived from insects – specifically from *Dactylopius coccus* – that containing hydroxyl groups shows free radical scavenging ability [118].

Given that Symbiodiniaceae algae are the primary targets of thermal stress during bleaching events, experiencing photosystem II damage, ROS overproduction, and eventual expulsion from the coral host [17 119]. For this reason, the direct interaction between microparticles and algae was investigated on the *Breviolum psygmophylum* species. Preliminary tests in liquid cultures confirmed MPs' biological compatibility and positive effects on algae's growth and ecophysiology. For this reason, in the second stage of the study, a higher level of control over drug release was assessed by encapsulating both Symbiodiniaceae and microparticles within a hyaluronic acid-based hydrogel scaffold, ensuring close contact between the algae and the antioxidant carriers. Hyaluronic acid was selected as a candidate material for its well-known biocompatibility with cells, as highly demonstrated in previous works [120,121]. The form of hydrogel was selected for cell growth and microparticles interaction to mimic as closely as possible the coral inner conformation [37]. Being a non-invasive technique and requiring the minimum amount of exposure time to light, the flat slab 3D bioprinting technique was used for the development of the material [122].

Material characterization and biological assays confirmed the beneficial effects of MPs on algal growth, chlorophyll *a* content, and resistance to light and thermal stress, particularly for MP2 formulations. Specifically, *in vivo* bleaching simulation on *Breviolum psygmophylum* – MP2 – hydrogel scaffolds demonstrated again curcumin's efficacy in scavenging ROS production.

Overall, these results highlight the potential of spray-dried antioxidant microparticles embedded in hydrogel scaffolds as an innovative and effective delivery platform for engineering heat- and

light-resistant Symbiodiniaceae, offering a promising step forward in coral bleaching mitigation strategies.

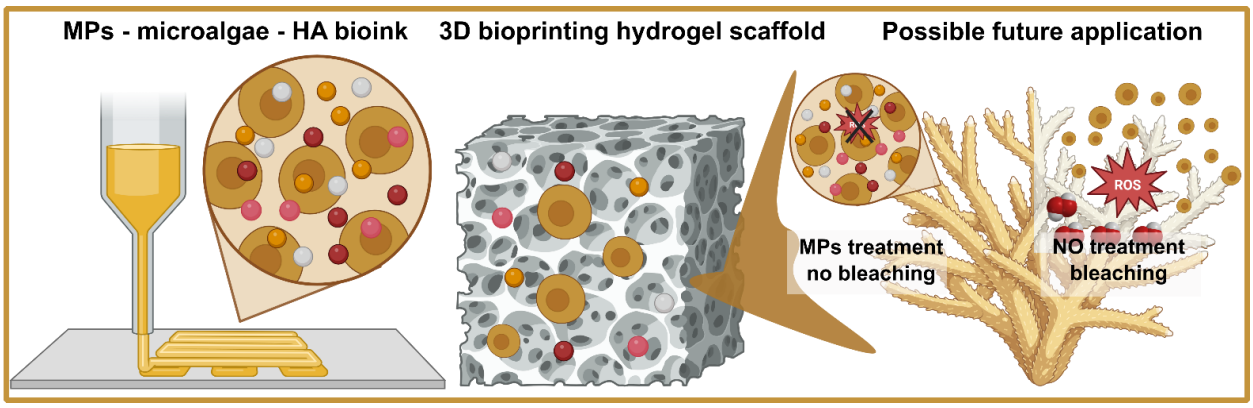

Figure 4.1 Schematic representation of 3D bioprinted hydrogel scaffold preparation and future possible application in coral bleaching treatment.

4.2 Materials and Methods

4.2.1 Materials

Bombyx morii silkworm cocoons were purchased from Cantiere della Provvidenza SPA Scs Onlus (Belluno, Italy), curcumin from *Curcuma longa* (turmeric) powder (Mw = 368.38 g/mol), ethanol, chitosan from crab shells (Mw = 600 kDa), carminic acid (Mw = 492.39 g/mol), reduced L-glutathione (Mw = 307.32), ethanol (≥99.8%), and acetic acid (≥ 99.8%) were purchased from Sigma-Aldrich. Sumac (*Rhus coriaria*) extract was provided by the Smart Bio-Interfaces facility of Istituto Italiano di Tecnologia, Pontedera. Symbiodinium cultures (species *Breviolum psygmophylum*) were kindly donated by Professor Martin Tresguerres of SCRIPPS Institution of Oceanography. Modified hyaluronic acid and Lithium phenyl-2,4,6-trimethylbenzoylphosphinate (LAP) photo-initiator were kindly provided by the Coral Reef Ecophysiology & Engineering group of SCRIPPS Institution of Oceanography.

4.2.2 Preparation of Microparticles via Spray Drying

Solutions Preparation

Four different types of microparticles (**MP**) were prepared via spray drying. Sumac-loaded chitosan microparticles are nominated **MP1**, curcumin-loaded silk microparticles **MP2**, glutathione-loaded chitosan microparticles **MP3**, and carminic-loaded carrageenan microparticles **MP4**. For each microparticle type, a specific solution was prepared as follows.

MP1 Solution Preparation

Based on the protocol described in the paper of Kosaraju *et al.* 2006 [123], 1% w/v chitosan microparticles loaded with 0.8% w/v of sumac extract were prepared by first dissolving 2.0 g of chitosan powder from crab shells in 181 mL of Milli-Q - acetic acid solution (96% Milli-Q - 4% acetic acid). Subsequently, 11.4 mL of sumac extract stock solution (70 mg/mL) was added to reach a final volume of 200 mL. The mixture was stirred on a 45°C hot plate until complete dissolution and homogenization prior to spray drying.

MP2 Solution Preparation

Similarly, based on the previous work on silk microparticles, where the emulsion-based method was used [107], 1% w/v silk microparticles loaded with 0.1% w/v curcumin powder were prepared in a 200 mL solution containing 2% v/v ethanol. Specifically, 33.3 mL of silk stock solution (60 mg/mL) was mixed with 0.2 g of curcumin powder dissolved in a mixture of 3.3 mL of ethanol and 163.4 mL of Milli-Q water. The components were gently stirred at room temperature for 1 hour to achieve complete dissolution and homogenization without disturbing the silk solution.

MP3 Solution Preparation

MP3 were prepared using 1% w/v chitosan microparticles loaded with 0.1% of reduced L-glutathione. 2.0 g of chitosan powder from crab shell and 0.2 g of reduced L-glutathione were dissolved in 200 mL of Milli-Q water, The solution was left under stirring on a 45°C hot plate until complete dissolution and homogenization prior to spray drying.

MP4 Solution Preparation

Following the paper of Tomoda *et al*. [124] and Obaidat *et al.* [125] 1% w/v carrageenan microparticles loaded with 0.01% w/v carminic acid were prepared in 200 mL of Milli-Q water by dissolving 2.0 g of carrageenan powder and 0.02 g of carminic acid in Milli-Q water and stirring continuously for 2 hours at 60°C. The heating time was limited to prevent gelation of carrageenan, which would increase the solution viscosity and complicate the spray drying process.

4.2.3 Spray Drying Process

The obtained solutions were then spray dried using the Mini Spray Dryer B290, acid-resistant, BUCHI, Flawil, Switzerland, with the following parameters: 100% aspiration rate, T (°C) inlet 180°C, T (°C) outlet between 90°C and 100°C, feed rate 15%.

At the end of each spray drying process, the obtained MP1, MP2, MP3, and MP4 powders were collected and weighed to evaluate the process yield according to the following formula:

$$yield\ \% = \frac{recovered\ powder\ (g)}{starting\ components\ amount\ (g)}\ x\ 100$$

The microparticles exhibited different yield percentages, which depended both on the amount of starting materials used and, on their composition, as well as on the resulting molecular weight of

the formulations. The yields were approximately ~18% for MP1, ~15% for MP2, ~30% for MP3, and ~15% for MP4. Similarly, encapsulation efficiency is a work in progress evaluation.

Microparticles Characterization

4.2.4 Scanning Electron Microscopy

The morphology of all the obtained microparticles – MP1, MP2, MP3, MP4 – was analyzed by Scanning Electron Microscopy (SEM), using a variable pressure JOEL JSM-649LA (JEOL, Tokyo, Japan) microscope equipped with a tungsten thermionic electron source and working in high vacuum mode, with an acceleration voltage of 5kV. The specimens were coated with a 10 nm thick film of gold utilizing a Cressington Sputter Coater – 208 HR (Cressington, Watford, UK).

4.2.5 ImageJ Analysis

The diameters of the microparticles were analyzed and determined by combining the SEM images with ImageJ software. Approximately 100 measurements were taken to determine the mean diameter distribution of each type of microparticles, and OriginPRO 2022 software (Version 9.9.0.225 (Government) was used to obtain the size distribution.

4.2.6 *In vitro* Reactive Oxygen Species (ROS) Scavenging Activity Assay

Free Antioxidant Compounds

The Amplex™ Red Hydrogen Peroxide/Peroxidase Assay Kit (*126*) was employed to evaluate the scavenging activity of free antioxidant compounds against hydrogen peroxide (H_2O_2), one of the key reactive oxygen species (ROS) involved in coral bleaching. This assay is specifically designed to detect and quantify H_2O_2 through the oxidation of the non-fluorescent Amplex™ Red reagent in the presence of horseradish peroxidase (HRP), producing resorufin, a highly

fluorescent compound. Fluorescence was measured using a plate reader at excitation/emission wavelengths of ~563/587 nm, respectively.

To assess antioxidant efficacy, 175 µg of each free compound - sumac extract, curcumin, reduced L-glutathione, and carminic acid - was added to individual wells of a 96-well plate along with a fixed amount of H_2O_2. Control wells included: (i) H_2O_2 only (positive control), and (ii) antioxidants only (background control). After the addition of the Amplex™ Red working solution, samples were incubated at room temperature for 30 minutes, and fluorescence intensity was recorded.

This experimental setup enabled the quantitative comparison of each compound's ability to scavenge hydrogen peroxide and thereby reduce oxidative stress.

Loaded Antioxidant Microparticles

The same assay was subsequently performed using 500 µg of each microparticle type (MP1, MP2, MP3, and MP4), under the assumption that the encapsulated antioxidant compounds would be released gradually from the microparticles. To account for this expected delayed release, a kinetic approach was adopted. Fluorescence measurements were taken at the following time points: T_0 (0 h), where the reaction mixture was added immediately after the microparticles and H_2O_2 were combined; T_1 (1 h), where the microparticles and H_2O_2 were incubated together for 1 hour prior to the addition of the reaction mixture; T_2 (24 h), incubation for 24 hours before the addition of the reaction mixture; and T_3 (48 h), incubation for 48 hours before the addition of the reaction mixture. This time-course experimental setup allowed for the evaluation of the antioxidant release kinetics from the microparticles and their effect on hydrogen peroxide scavenging over time.

4.2.7 In Liquid Microparticles – Symbiodiniaceae Algae Interaction

Cellular Growth

One of the main objectives of the study was to assess the interaction between the developed microparticles (MPs) and Symbiodiniaceae, with the aim of evaluating any potential positive or negative effects on their ecophysiology. To this end, algal growth was monitored in the standard culture medium (ASP-8A) supplemented with MPs.

Three different concentrations of each MP type were tested: 25 µg, 50 µg, and 100 µg. Experimental conditions were set up in a 12-well plate, with each well containing 2 mL of *Breviolum psygmophilum* culture under the following conditions: Positive control (algae only); C1 (algae + 25 µg MPs); C2 (algae + 50 µg MPs); and C3 (algae + 100 µg MPs). The cultures were incubated for 15 days at 25°C under a 13 h light / 11 h dark photoperiod, with a light intensity of 100 µmol photons m^{-2} s^{-1} (PAR). Algal growth was assessed by measuring optical density (OD) and performing cell counts using a hemocytometer every 3 days. Growth curves were analyzed to determine any dose-dependent effects of the MPs on algal proliferation.

4.2.8 Imaging Pulse-Amplitude Modulated (PAM) Fluorometry

Maximum Quantum Yield (Fv/Fm)

To assess whether microparticles interfere with the photosynthetic activity of dinoflagellate algae, PAM fluorometry was performed on the Symbiodinium-MPs well plate from the cellular growth experiment. Specifically, an imaging pulse amplitude-modulated chlorophyll a fluorometer (Imaging PAM, mini version; WALZ GmbH, Effeltrich, Germany), equipped with a blue measuring light (460 nm), was used to measure the maximum quantum yield of photosystem II (Fv/Fm). Measurements were taken for different microparticle types (MP1, MP2, MP3, and MP4) and concentrations (C1 - 25 µg, C2 - 50 µg, and C3 - 100 µg) at 24 hours, 48

hours, 7 days, and 14 days after incubation. Prior to each measurement, the well plates were removed from the incubator and placed in a black acrylic chamber for dark adaptation (20 minutes). A saturation pulse (default settings) was then applied to determine Fv/Fm. For each well, seven areas of interest were selected where the plate was in sharp focus for Fv/Fm analysis.

4.2.9 Electron Transport Rate

Electron transport rate (ETR) curves provide insight into the rate of electron flow through photosystem II (PSII), reflecting the activity and efficiency of the light-dependent reactions of photosynthesis under varying conditions. To generate ETR curves, samples were exposed to continuous actinic light using the Imaging PAM system, simulating sunlight to drive photosynthetic activity. Measurements were conducted for four microparticle types (MP1, MP2, MP3, and MP4) at three concentrations (C1 - 25 µg, C2 - 50 µg, and C3 - 100 µg).

4.2.10 Chlorophyll *a* extraction

Chlorophyll *a* extraction from Symbiodinium–microparticle liquid cultures was performed on samples collected 15 days post-incubation. From each well, 0.3 mL of culture was collected in triplicate and transferred to Eppendorf tubes. Samples were centrifuged at 13,000 rpm for 1 minute, and the supernatant was discarded. Each pellet was washed by adding 1 mL of Milli-Q water, followed by vortexing and a second centrifugation at 13,000 rpm for 1 minute. After discarding the supernatant, the pellets were protected from light by wrapping the tubes in aluminum foil. A 1 mL extraction solution (5% DMSO and 95% acetone; 50 µL DMSO + 950 µL acetone) was added to each tube, and samples were stored at 4°C until chlorophyll *a* quantification. The full chlorophyll *a* absorption spectrum was recorded using a plate reader. Concentrations were calculated using the method described by Jeffrey and Humphrey [62].

Additionally, since optical density (OD) and cell density had been measured before extraction, chlorophyll *a* content per cell was also determined.

4.2.11 In Hydrogel Microparticles – Symbiodiniaceae Algae Interaction

Flat Slab 3D Bioprinting

To enhance the interaction between algae and microparticles (MPs) and to develop a material potentially suitable for direct application on corals, a 3D bio-printed hydrogel scaffold incorporating Symbiodinium and MPs was fabricated using the flat slab technique. Scaffolds were produced for each type of microparticle, alongside a positive control containing only algae without MPs. The hydrogel scaffold was primarily composed of modified hyaluronic acid (HA) (glycidyl-methacrylate hyaluronic acid - GMHA). Five bioinks were formulated as follows: **Bioink 1** (Control) – HA, Symbiodinium algae, culture medium, and LAP (photo-initiator); **Bioink 2** (MP1) – HA, Symbiodinium algae, MP1, and LAP; **Bioink 3** (MP2) – HA, Symbiodinium algae, MP2, and LAP; **Bioink 4** (MP3) – HA, Symbiodinium algae, MP3, and LAP; **Bioink 5** (MP4) – HA, Symbiodinium algae, MP4, and LAP.

Approximately 150 µL of bioink was gently dispensed for each formulation onto methacrylated glass coverslips positioned within a 200 µm-thick PDMS mold pre-attached to define the scaffold shape. Cross-linking was initiated by exposing the samples to UV light for 20 seconds. After polymerization, the PDMS molds were carefully removed, and the coverslips were transferred into individual wells of a 6-well plate containing 6 mL of ASP8A medium, which was replaced every two days to maintain algal viability and promote growth.

4.2.12 Imaging Pulse-Amplitude Modulated (PAM) Fluorometry

Maximum Quantum Yield (Fv/Fm)

Before each media change, PAM fluorometry was performed to assess the physiological health of the Symbiodinium cells by measuring their maximum quantum yield of photosystem II (PSII) as previously described.

4.2.13 *In vivo* Bleaching Simulation Experiment

Based on the results from PAM analysis, a simulated bleaching experiment was performed on hydrogel scaffolds containing MP2. Hydrogel scaffolds with and without MP2 were prepared using the flat slab 3D bioprinting technique, as described previously. Samples were incubated under standard conditions (100 µmol m^{-2} s^{-1} PAR and 25°C) for three days to allow the algae to recover from prior UV-light exposure. Following this recovery period, Symbiodinium-loaded hydrogels, both with and without MP2, were subjected to a gradual temperature increase over five days. Starting at 25°C, the temperature was raised by 1.5°C daily, reaching 31°C on the final day. A positive control was maintained at constant standard conditions (100 µmol m^{-2} s^{-1} PAR and 25°C) throughout the experiment.

4.2.14 Diving Pulse-Amplitude Modulated (PAM) Fluorometry

Effective Quantum Yield Y(II)

To assess the overall health of samples without removing them from the incubator (and thus minimizing temperature and light fluctuations), diving PAM measurements under light conditions were preferred over Imaging PAM analysis. The diving PAM instrument (Walz, Germany) integrates fluorescence over a 2–8 mm diameter area via its optical fiber, allowing direct and convenient access to the samples in situ. The effective quantum yield Y(II) was measured instead of Fv/Fm to avoid the need for dark adaptation and prevent interference with

the bleaching experiment. Measurements were performed on the positive control (normal conditions), the negative control (bleaching conditions without microparticles), and the Symbiodinium–hydrogel scaffold containing MP2.

4.2.15 *In vivo* Reactive Oxygen Species (ROS) Scavenging Activity Assay

Following the previously described protocol, the Amplex™ Red Hydrogen Peroxide/Peroxidase Assay Kit was used to evaluate the scavenging activity of MP2 against hydrogen peroxide (H_2O_2). Each day, 50 µL of medium was carefully collected from each well—maintaining proximity to the hydrogel—and mixed with 50 µL of H_2O_2. Subsequently, 50 µL of the reaction mixture was added, and the samples were incubated for 30 minutes to allow the reaction to proceed. Fluorescence measurements were then recorded using a plate reader. On day 5, when the temperature reached 31°C, reactive oxygen species (ROS) measurements were performed three times throughout the day.

4.3 Results

4.3.1 Characterization of microparticles

A schematic overview of the microparticle production process is presented in **Figure 4.2**. The figure illustrates materials, formulations, mixing procedures, and the spray-drying technique employed for each microparticle type: **A)** chitosan microparticles loaded with sumac extract (MP1); **B)** silk microparticles loaded with curcumin (MP2); **C)** chitosan microparticles loaded with reduced L-glutathione (MP3); and **D)** carrageenan microparticles loaded with carminic acid (MP4). The intense color of the obtained powders visually indicated the successful encapsulation of antioxidant compounds. SEM analysis (**Figure 4.3**) was performed to further characterize the samples to evaluate morphology and particle size. All microparticle types appeared uniform and spherical, consistent with the spray-drying process. Size distributions are reported alongside the

SEM images for each formulation. Although the same technique was used for all microparticles, differences in mean particle size were observed, likely due to the distinct polymers and antioxidant compounds employed. Specifically, MP1, MP2, and MP3 showed comparable mean diameters of 3.0 ± 1.0, 3.5 ± 1.5, and 3.0 ± 2.0 μm, respectively, whereas MP4 exhibited the largest size, with a mean diameter of 6.0 ± 2.5 μm.

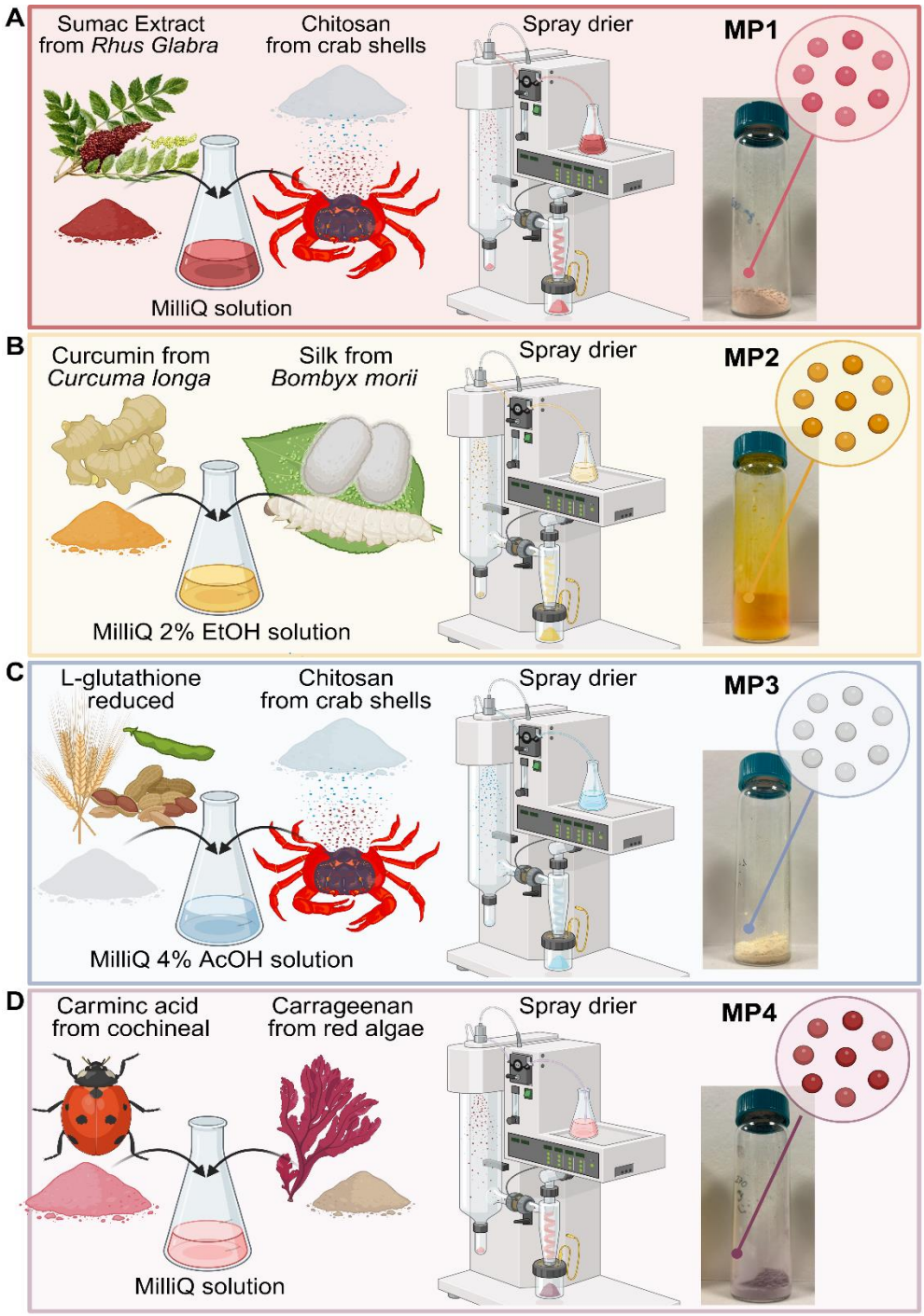

Figure 4.2 Schematic representation of the preparation of the different types of microparticles through the spray drying technique. **A)** MP1 – chitosan microparticles loaded with sumac extract; **B)** MP2 – silk microparticles loaded with curcumin; **C)** MP3 – chitosan microparticles loaded with reduced L-glutathione; and **D)** MP4 – carrageenan microparticles loaded with carminic acid.

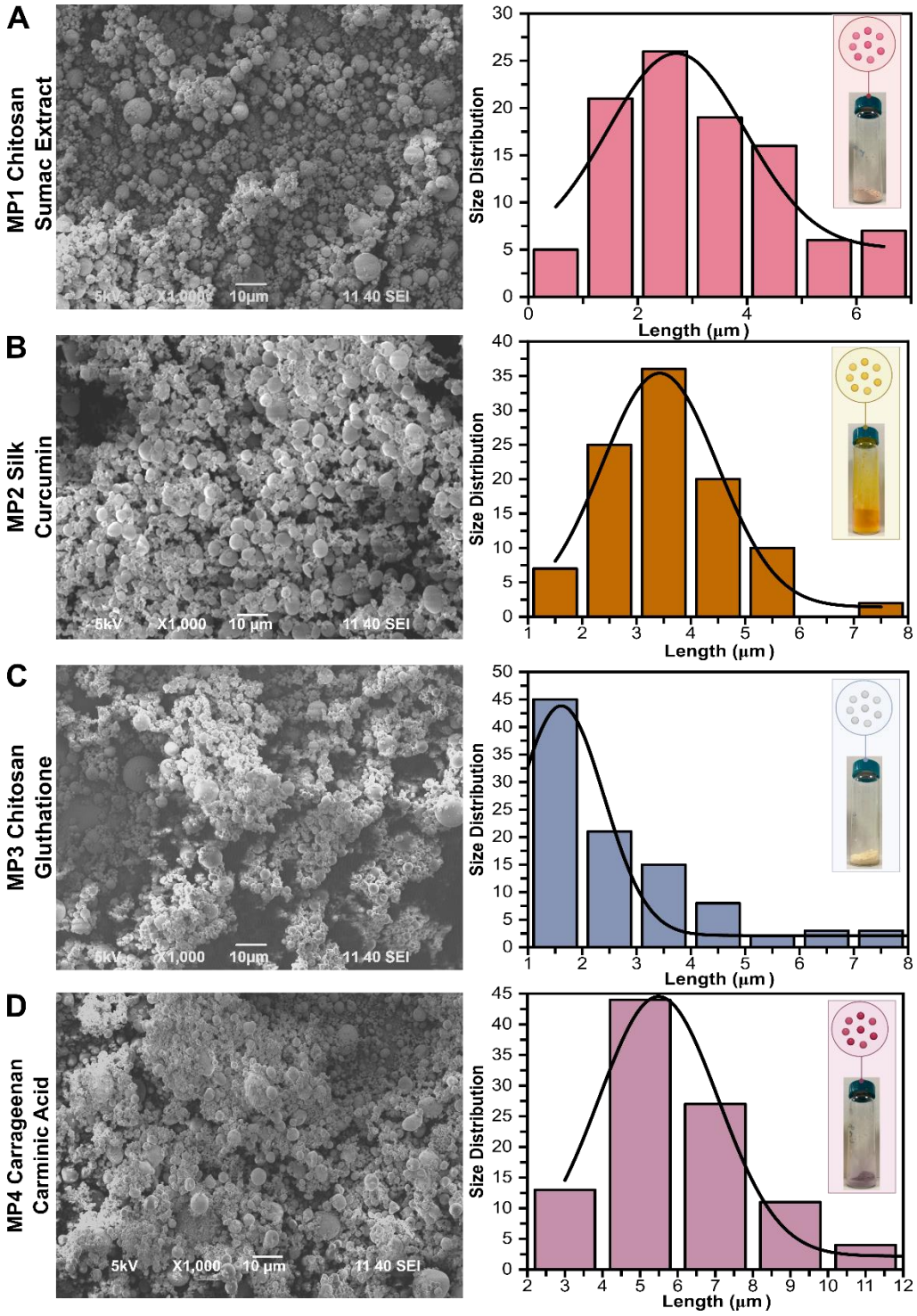

Figure 4.3 Morphological analysis and size distribution for each type of MPs. **A)** MP1; **B)** MP2; **C)** MP3; and **D)** MP4.

4.3.2 *In vitro* Reactive Oxygen Species (ROS) scavenging assay

To evaluate the antioxidant capacity of both free compounds and loaded microparticles, the Amplex™ Red Hydrogen Peroxide/Peroxidase assay was performed as described in the Materials and Methods section. By monitoring the kinetics of interaction between 500 μg of each microparticle type and H_2O_2 in solution, the final percentage of neutralized H_2O_2 was calculated (**Figures 4.4A–D** and **4.5A–D**). In all cases, initial fluorescence values - reflecting the H_2O_2 concentration - were markedly lower than the control (H_2O_2 alone), which remained almost constant throughout the experiment (~1.5E8 ± 2.2E6). All microparticles' fluorescence values decreased progressively, reaching their minimum after 120 h of interaction. The lowest fluorescence signal was observed for MP1 (1.0E7 ± 7.9E5), corresponding to nearly complete H_2O_2 neutralization (~100%). MP2, MP3, and MP4 reached slightly higher fluorescence values (1.5E7 ± 2.2E6; 1.8E7 ± 1.2E6; and 1.8E7 ± 2.3E6, respectively), translating into ~90%, 80%, and 75% H_2O_2 neutralization, thus confirming a strong antioxidant capacity, particularly with extended incubation times.

In contrast, kinetic experiments were not necessary for free antioxidant compounds. As shown in **Figure 4.5E**, fluorescence values were already substantially lower than the control at 175 μg of material, with mean values of 3.5E6 ± 3.0E6 for sumac extract (scavenger 1), 2.5E6 ± 4.2E6 for curcumin (scavenger 2), 6.5E6 ± 1.1E6 for reduced L-glutathione (scavenger 3), and 1.5E5 ± 2.3E4 for carminic acid (scavenger 4). In all cases, H_2O_2 was completely neutralized (~100%), as further confirmed in **Figure 4.5F**.

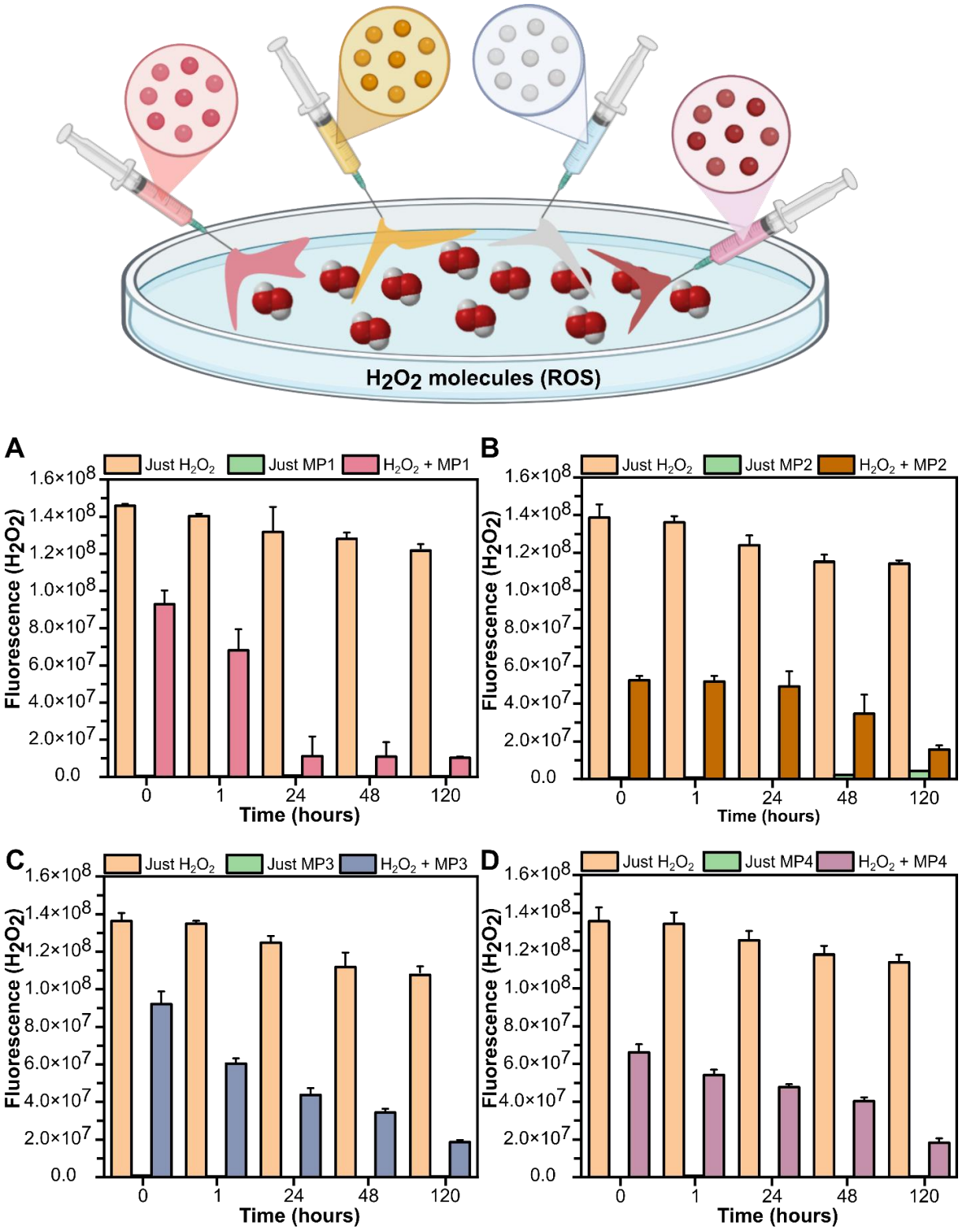

Figure 4.4 Kinetic *in vitro* Reactive Oxygen Species (ROS) scavenging activity of each MPs type**. A)** MP1; **B)** MP2; **C)** MP3; and **D)** MP4.

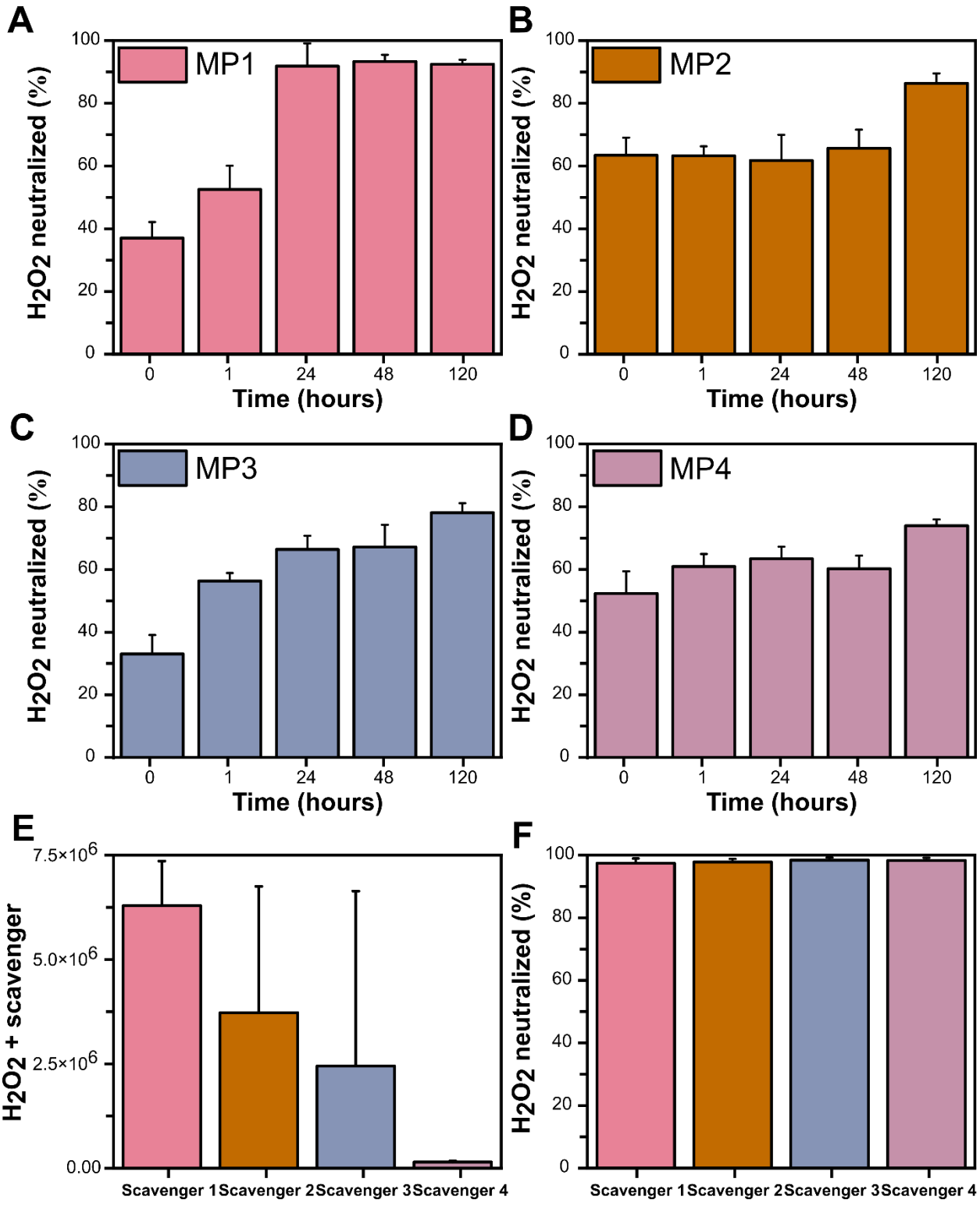
A
MP1
H2O2 neutralized (%)
Time (hours)
B
MP2
H2O2 neutralized (%)
Time (hours)
C
MP3
H2O2 neutralized (%)
Time (hours)
D
MP4
H2O2 neutralized (%)
Time (hours)
E
H2O2 + scavenger
Scavenger 1
Scavenger 2
Scavenger 3
Scavenger 4
F
H2O2 neutralized (%)
Scavenger 1
Scavenger 2
Scavenger 3
Scavenger 4

Figure 4.5 Results of the in vitro ROS scavenging activity test for loaded microparticles and free antioxidant compounds. The percentage of H_2O_2 neutralized over time is shown for **A)** MP1, **B)** MP2, **C)** MP3, and **D)** MP4. Panels **E)** and **F)** report fluorescence values and the corresponding percentage of H_2O_2 neutralization achieved by the free antioxidant compounds.

4.3.3 Symbiodinium – microparticles interaction in liquid

Cellular growth

The interaction between microparticles (MPs) and Symbiodinium algae was assessed by monitoring dinoflagellate growth over 14 days in the presence of different material concentrations. OD measurements and growth curves are shown in **Figure 4.6 A-D** and revealed a positive growth trend for *Breviolum psygmophilum*, suggesting a potential beneficial effect of all microparticle types, even at the highest tested concentration (100 µg). Notably, algal growth increased with rising MP concentrations, particularly during the exponential phase. This effect was consistent across all formulations, but was most pronounced for MP3 and MP4, where the highest concentration yielded a maximum cell density of ~4.0×10^6 compared with the control (~2.0×10^6), consisting of algae cultured without microparticles.

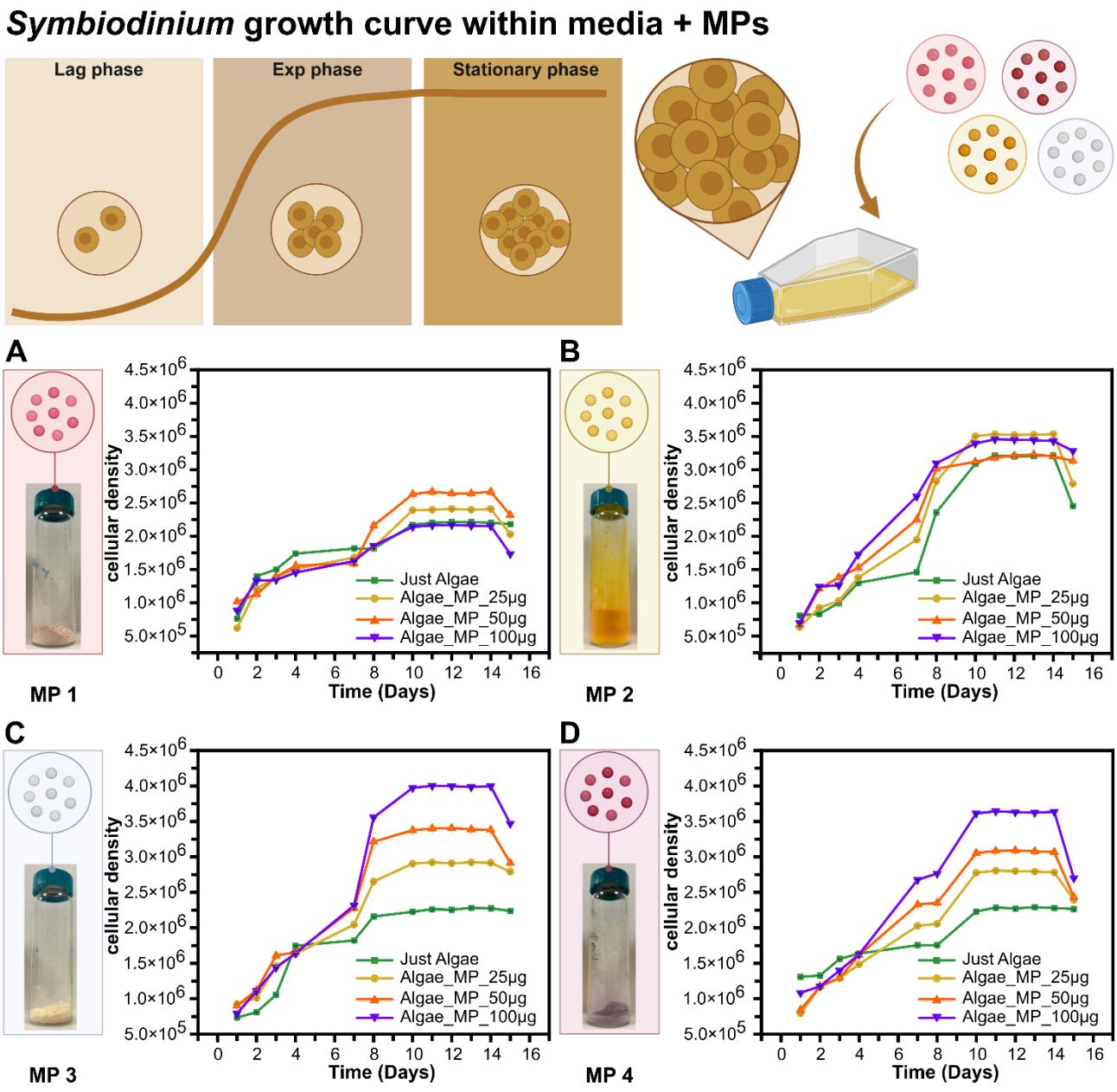

Figure 4.6 Cellular growth of Symbiodinium algae in liquid culture within ASP8A media enriched without MPs (CTRL) and with each type of MPs. **A)** MP1; **B)** MP2; **C)** MP3; and **D)** MP4.

4.3.4 Imaging PAM – Maximum Quantum Yield and Electron Transport Rate (ETR) Curves

Imaging-PAM analysis of *Breviolum psygmophilum* cultures grown with and without MPs was performed after 24 h, 48 h, 7 days, and 14 days to assess potential effects of the materials on algal photosynthetic activity. Maximum quantum yield (Fv/Fm) was measured (**Figure 4.7A–D**), and no significant changes were observed. Fv/Fm values remained comparable to the initial measurements for all microparticle types (~0.27–0.30), indicating stable photosynthetic performance throughout the experiment.

Encouraged by the positive effects of microparticles on algal growth, ETR curves were recorded after 14 days to further evaluate their impact. Since exposing algae to increasing light intensities until photoinhibition can slightly damage dinoflagellate cells, measurements were performed at the two-week time point to minimize interference with growth. As shown in **Figures 4.8A–D**, control samples (algae without MPs) exhibited the typical ETR profile of Symbiodiniaceae: minimal fluorescence at the start, a progressive increase to a maximum, a short plateau, and a final decline as photoinhibition occurred. In contrast, cultures treated with MPs displayed broader curves, indicating a delayed onset of photoinhibition and suggesting enhanced thermal tolerance. This effect was concentration-dependent and particularly pronounced for MP3 and MP4, where higher MP levels corresponded to wider curves. Overall, these findings support the hypothesis that MPs may improve dinoflagellate resilience to high-light stress and could potentially be applied to engineer Symbiodiniaceae strains more resistant to environmental challenges such as coral bleaching.

4.3.5 Chlorophyll *a* extraction

Chlorophyll *a* extraction was carried out on samples following light exposure during the ETR experiment. The results, reported in **Figure 4.9**, should be interpreted with caution, as light

exposure may have partially damaged the cells and thus affected reliability. To account for this, a second extraction was performed on parallel cultures grown under identical conditions but not exposed to light, with results shown in **Figure 4.8E**. In the "damaged" cultures, higher concentrations of MPs were associated with increased chlorophyll *a* content for MP1, MP3, and MP4, but not for MP2. By contrast, in the "healthy" samples, chlorophyll *a* content increased consistently with MP concentration across all formulations. The highest values were observed at 100 µg MPs, reaching ~6 µg per 10^6 cells compared with ~4 µg per 10^6 cells in the control cultures (algae only).

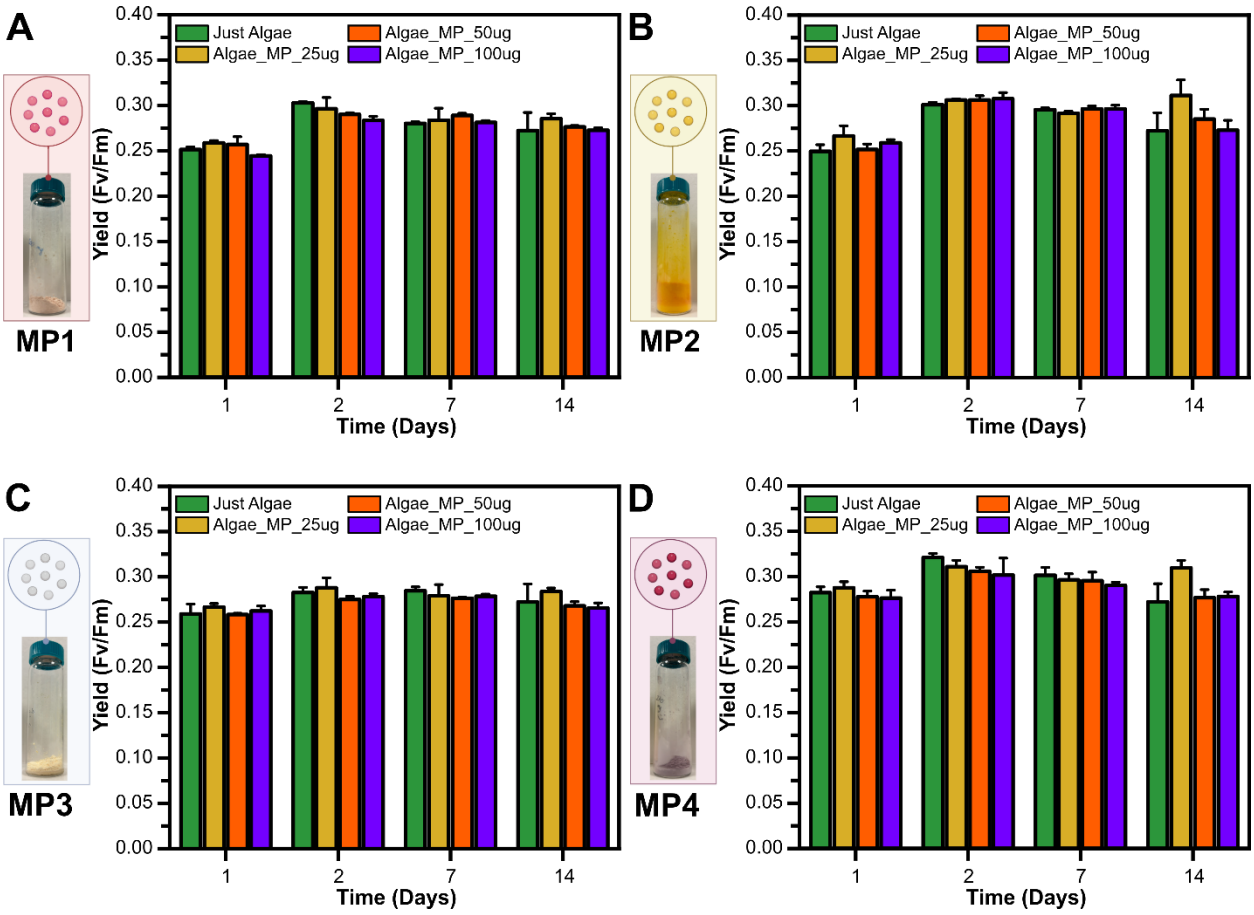

Figure 4.7 Fv/Fm values from Imaging PAM analysis for each type of MPs. **A)** MP1; **B)** MP2; **C)** MP3; and **D)** MP4.

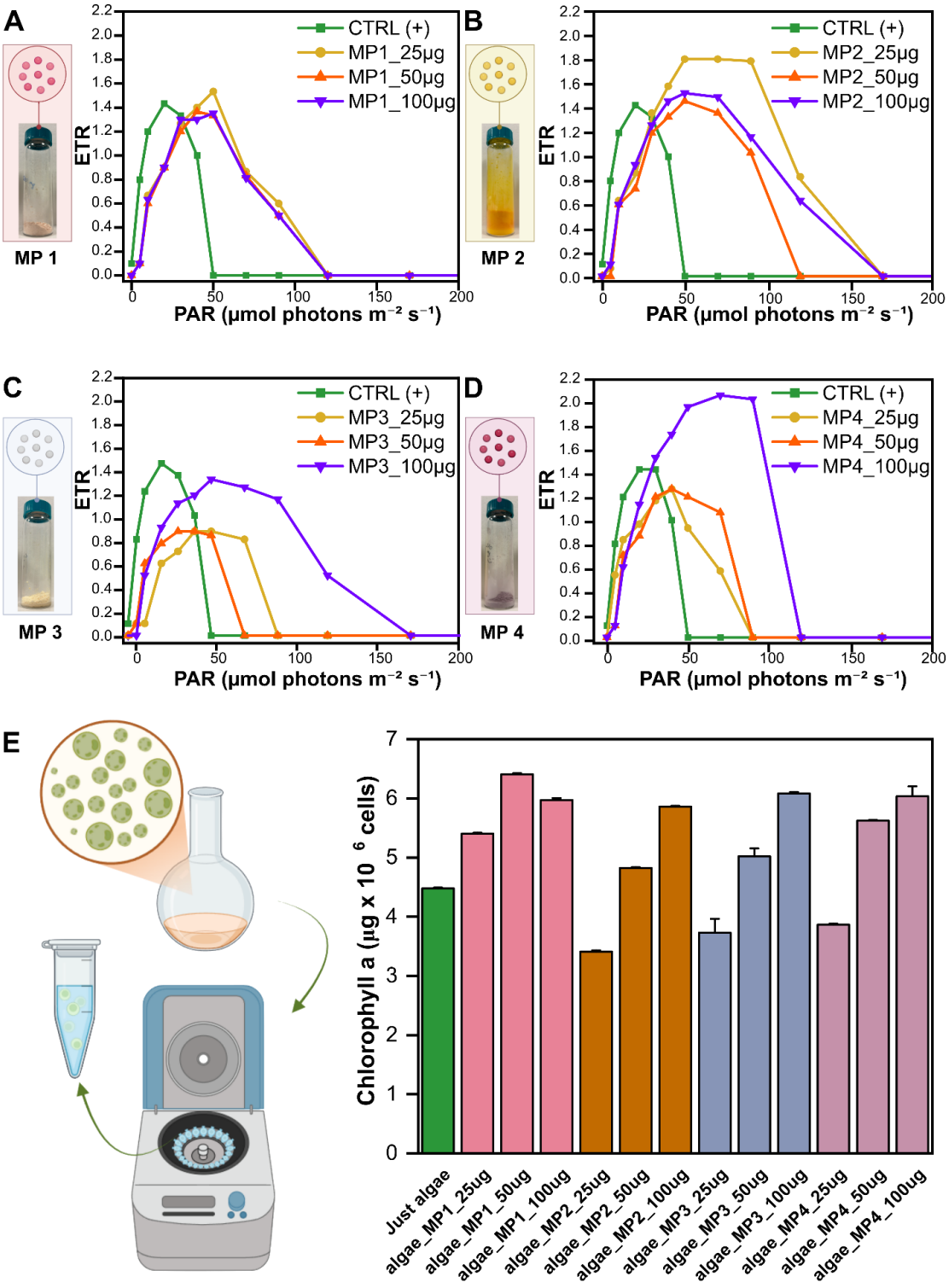

Figure 4.8 Electron Transport Rate (ETR) curves of symbiodinium algae grown within ASP8A media enriched with each type of MPs. **A)** MP1; **B)** MP2; **C)** MP3; and **D)** MP4. **E)** chlorophyll a content within algae (CTRL +) and algae grown with different concentrations of MPs.

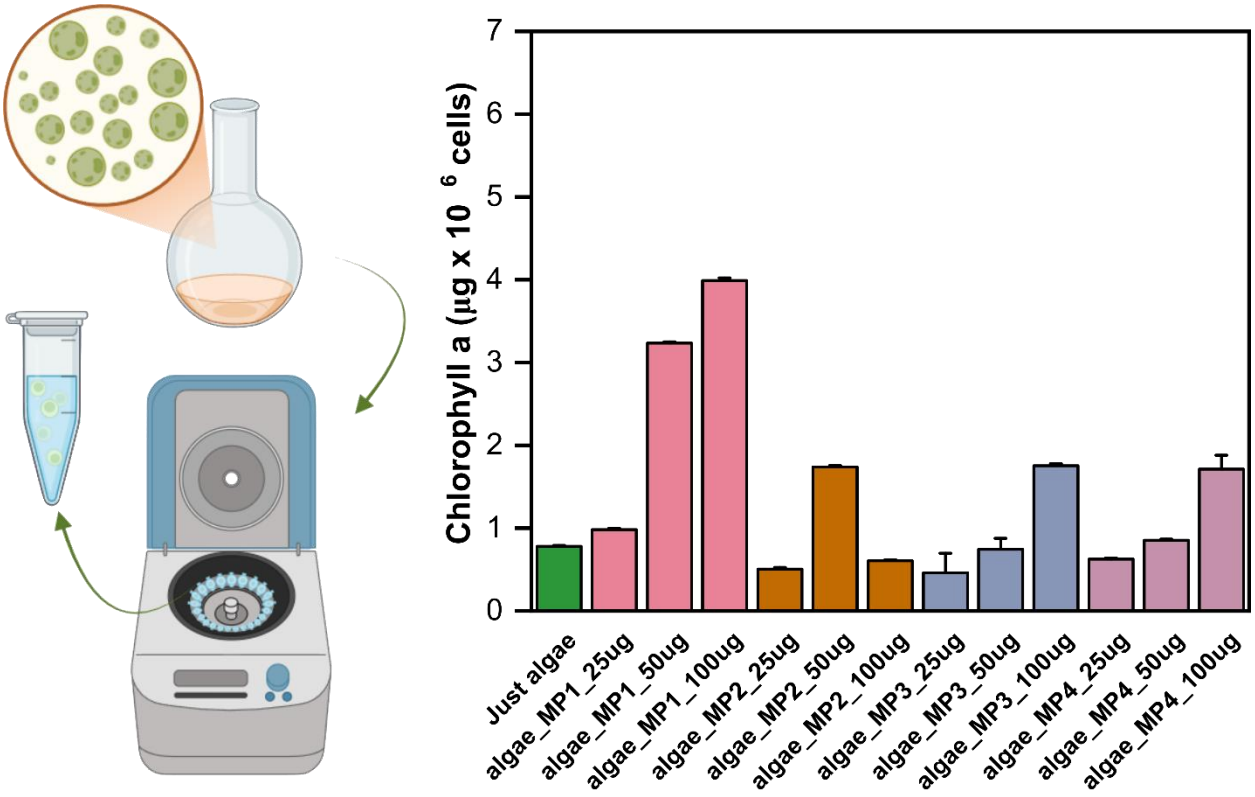

Figure 4.9 Chlorophyll *a* extraction performed on Symbiodinium algae grown with and without MPs and then exposed to the light of the ETR curves experiment.

4.3.6 Symbiodinium - microparticles interaction in hydrogel

Figure 4.10 provides a schematic representation of the flat-slab 3D bioprinting technique employed to fabricate the hyaluronic acid hydrogel scaffold. This approach allowed for the precise deposition of bioinks containing the different microparticle formulations. The bioinks used and the resulting hydrogel scaffolds after 14 days of incubation for each microparticle type are shown in **Figures 4.11A–D**. In all cases, the hydrogel can be clearly observed at the bottom of the well-plate, where it retained its structure throughout the culture period. Notably, the hydrogels displayed a characteristic brownish coloration, attributable to the presence of algae incorporated within the system, further confirming the successful embedding of the cells into the

scaffold matrix. This visual evidence supports the stability of the bioprinted constructs and their capacity to host living microalgae in a structured 3D environment.

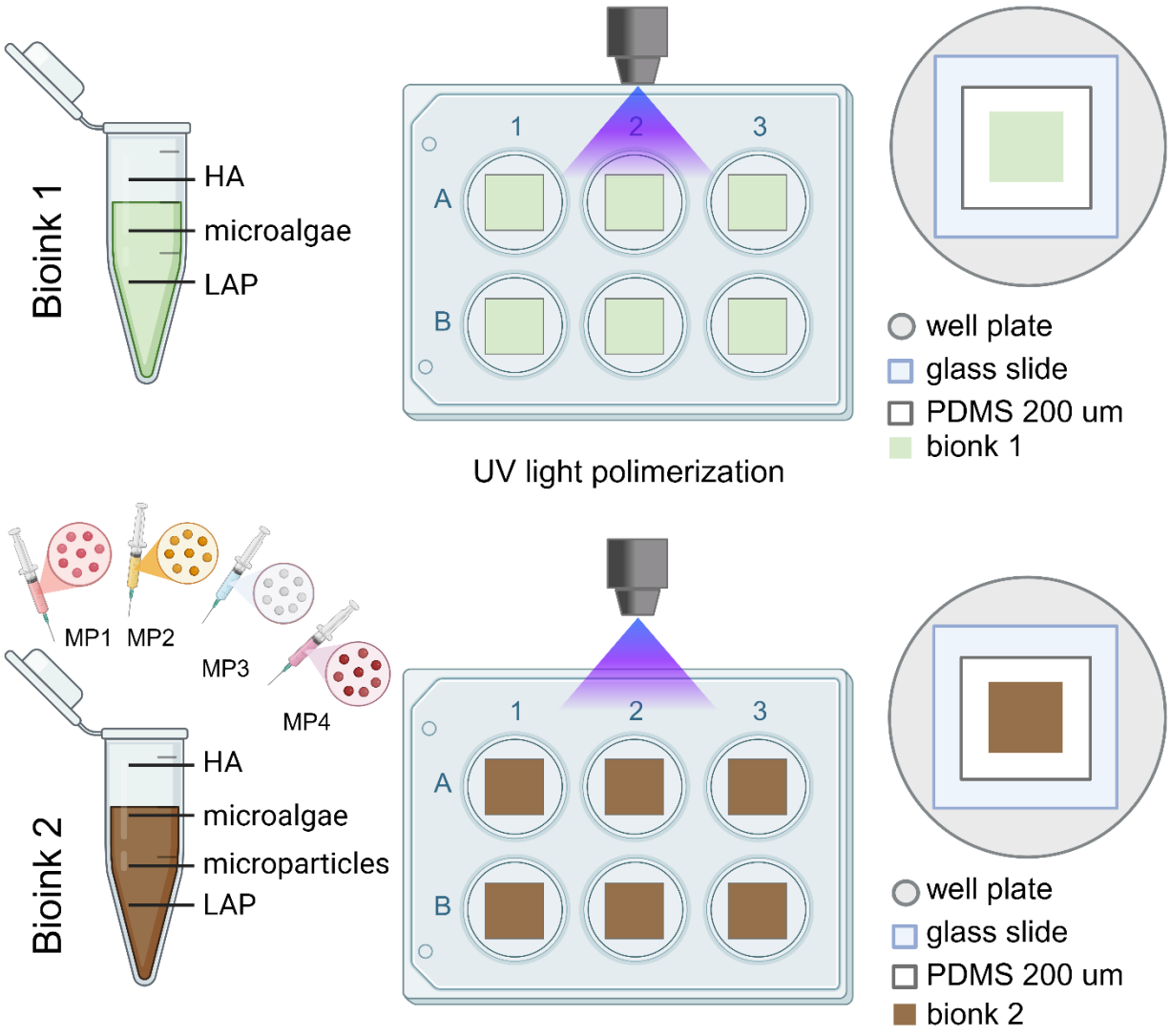

Figure 4.10 Schematic representation of flat-slab 3D bioprinting technique used for hydrogel scaffold development.

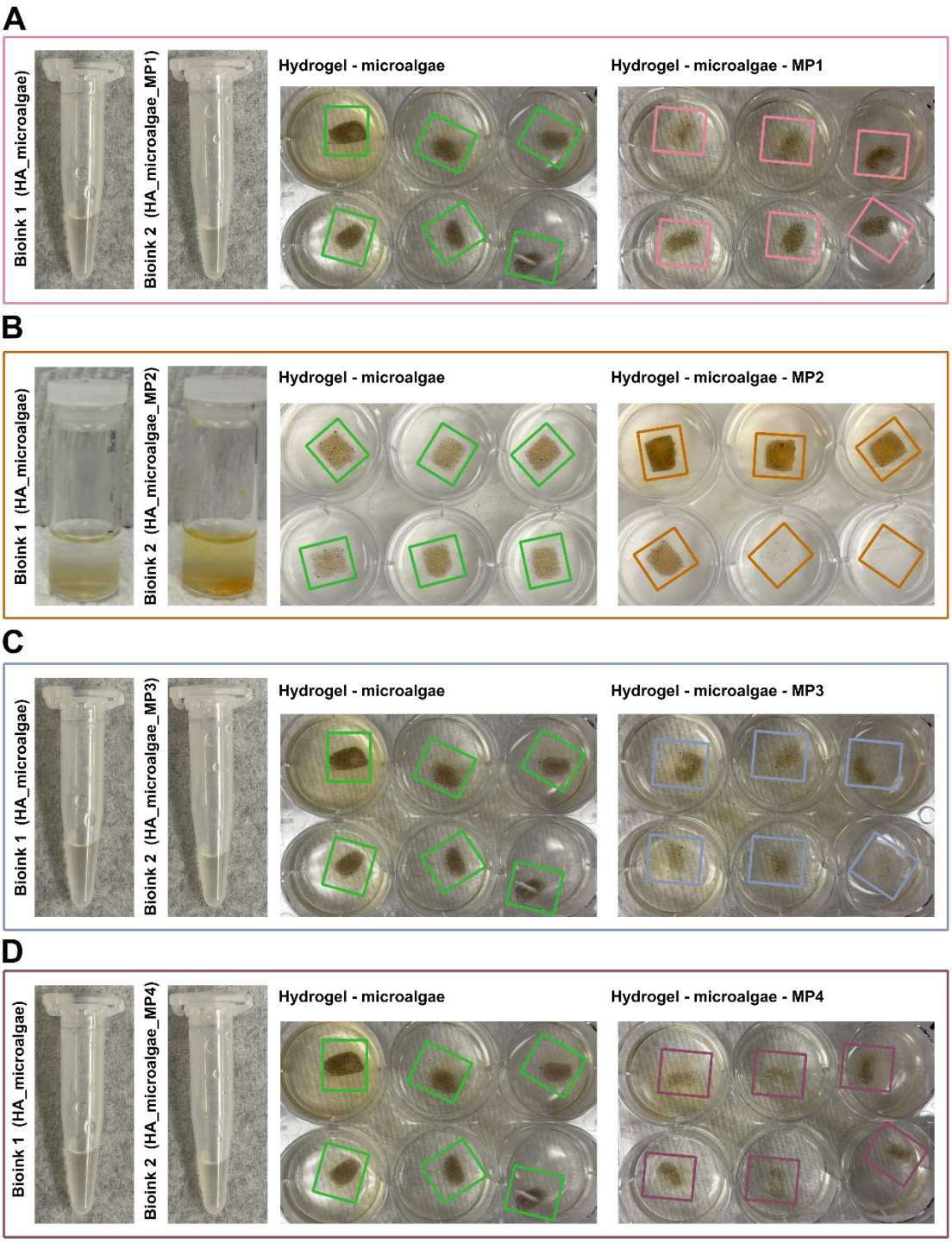

Figure 4.11 Bioinks used for flat-slab 3D bioprinting technique and relative appearance of Symbiodinium hydrogel scaffolds without MPs and with each type of MPs**.** A) MP1; B) MP2; C) MP3; and D) MP4.

4.3.7 Imaging PAM – Maximum Quantum Yield

Similar to the experiments investigating the interaction between Symbiodinium and microparticles in liquid culture, Fv/Fm measurements were performed for all microparticle types in the 3D hydrogel scaffolds, particularly 24 hours after UV-light exposure required by the bioprinting process. This approach allowed for the assessment of potential algal recovery after light exposure and the evaluation of any protective effect provided by the microparticles.

Following printing, the hydrogel scaffolds were maintained for three days in an incubator at 25°C under 100 PAR on a gentle shaker. Fv/Fm measurements were then collected on day 4 and subsequently every two days until day 15, as shown in **Figure 4.12A-D**. MP1, MP3, and MP4 exhibited a similar pattern: no detectable yield was observed 24 hours after printing, and Fv/Fm values were initially lower in microparticle-loaded scaffolds compared with the control scaffolds containing algae only. A gradual recovery occurred by day 13, with Fv/Fm values reaching 0.424 ± 0.02, 0.431 ± 0.02, and 0.436 ± 0.02 for MP1, MP3, and MP4, respectively, compared with 0.375 ± 0.028 in the control.

Interestingly, MP2 showed a distinct trend. Fv/Fm values were low immediately after 24 hours in MP2-loaded scaffolds (0.116 ± 0.03), while control scaffolds showed no decline. However, MP2 scaffolds displayed a steady increase in Fv/Fm throughout the experiment, ultimately achieving the highest values among all conditions. Overall, the experiment demonstrated sustained Fv/Fm values in Symbiodinium-microparticle hydrogel scaffolds up to day 15, at this point, algal density may have begun to limit growth. The superior performance of MP2 suggests a potential protective effect of these microparticles during light exposure. All the values for MP1, MP2, MP3, and MP4 for the entire experiment duration are reported in **Figure 4.13**.

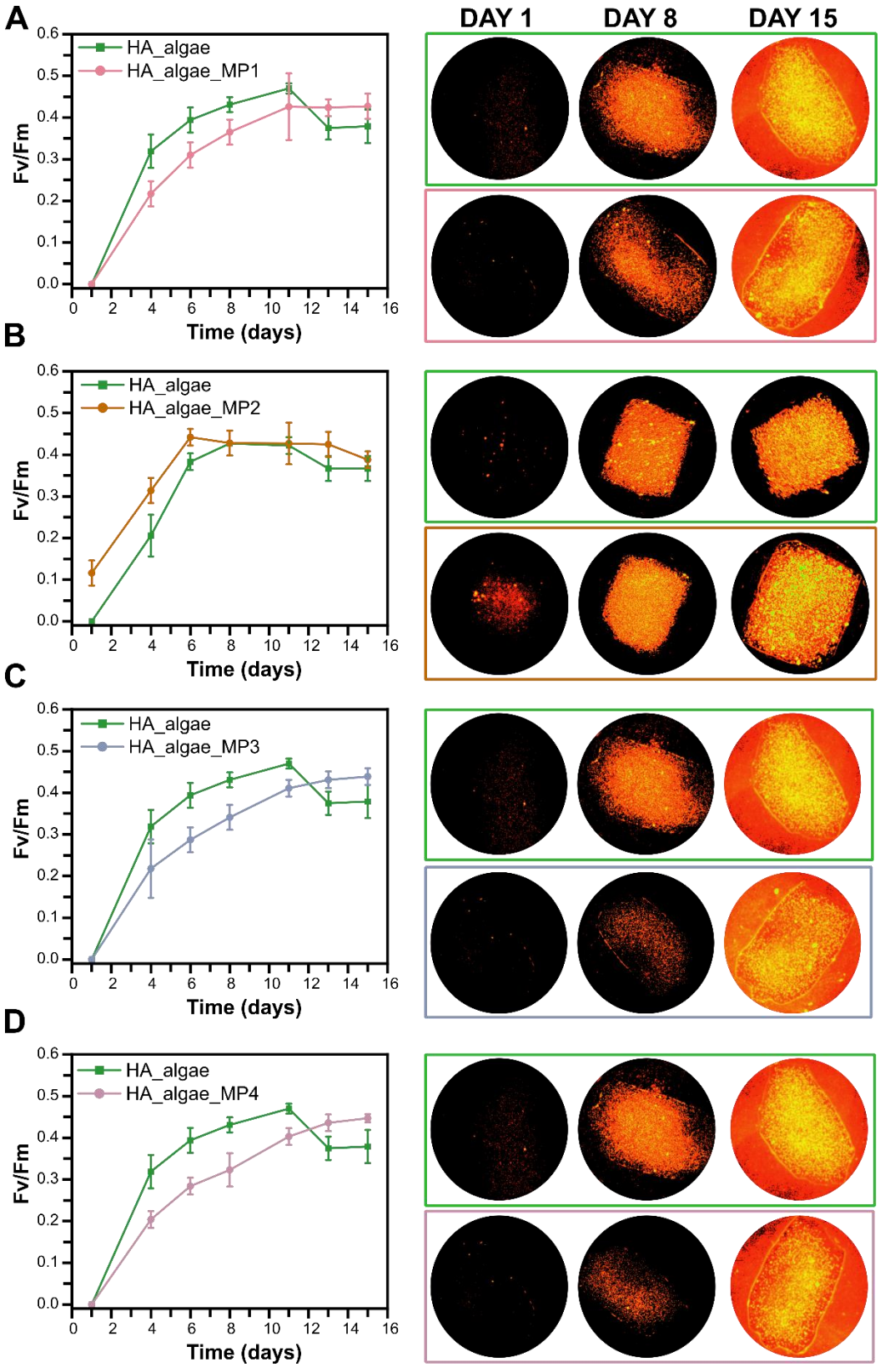
A
B
C
D
DAY 1
DAY 8
DAY 15
HA_algae
HA_algae_MP1
HA_algae_MP2
HA_algae_MP3
HA_algae_MP4
Fv/Fm
Time (days)
0.0
0.1
0.2
0.3
0.4
0.5
0.6
0
2
4
6
8
10
12
14
16

Figura 4.12 Imaging PAM results expressed as quantum maximum yield (Fv/Fm) and relative appearance at day 1, 8, and 15 for empty and MPs-relative loaded hydrogels. **A)** Symbiodinium-hydrogel scaffold with and without MP1; **B)** Symbiodinium-hydrogel scaffold with and without MP2; **C)** Symbiodinium-hydrogel scaffold with and without MP3; **D)** Symbiodinium-hydrogel scaffold with and without MP4.

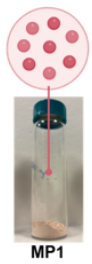

Mean Fv/Fm	HA – algae	HA – algae - MPs
Day 1	0.00 ± 0.00	0.00 ± 0.00
Day 4	0.319 ± 0.04	0.217 ± 0.03
Day 6	0.394 ± 0.03	0.310 ± 0.03
Day 8	0.431 ± 0.018	0.365 ± 0.03
Day 11	0.470 ± 0.012	0.426 ± 0.08
Day 13	0.375 ± 0.028	0.424 ± 0.02
Day 15	0.379 ± 0.004	0.427 ± 0.03

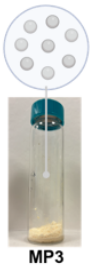

Mean Fv/Fm	HA – algae	HA – algae - MPs
Day 1	0.00 ± 0.00	0.00 ± 0.00
Day 4	0.319 ± 0.04	0.218 ± 0.07
Day 6	0.394 ± 0.03	0.287 ± 0.03
Day 8	0.431 ± 0.018	0.341 ± 0.03
Day 11	0.470 ± 0.012	0.411 ± 0.02
Day 13	0.375 ± 0.028	0.431 ± 0.02
Day 15	0.379 ± 0.004	0.439 ± 0.02

Mean Fv/Fm	HA – algae	HA – algae - MPs
Day 1	0.00 ± 0.00	0.116 ± 0.03
Day 4	0.206 ± 0.05	0.314 ± 0.03
Day 6	0.383 ± 0.02	0.442 ± 0.02
Day 8	0.427 ± 0.01	0.428 ± 0.03
Day 11	0.422 ± 0.02	0.427 ± 0.05
Day 13	0.367 ± 0.03	0.425 ± 0.03
Day 15	0.367 ± 0.03	0.388 ± 0.02

Mean Fv/Fm	HA – algae	HA – algae - MPs
Day 1	0.00 ± 0.00	0.00 ± 0.00
Day 4	0.319 ± 0.04	0.204 ± 0.02
Day 6	0.394 ± 0.03	0.284 ± 0.02
Day 8	0.431 ± 0.018	0.323 ± 0.04
Day 11	0.470 ± 0.012	0.403 ± 0.02
Day 13	0.375 ± 0.028	0.436 ± 0.02
Day 15	0.379 ± 0.004	0.447 ± 0.01

Figure 4.13 Imaging PAM results expressed as Fv/Fm across 14 days of experiment for "empty" and MPs-loaded Symbiodinium hydrogel scaffolds. **A)** MP1, **B)** MP2, **C)** MP3, and **D)** MP4.

4.3.8 *In vivo* Bleaching Simulation Experiment

Diving PAM - Effective Quantum Yield

Imaging-PAM results for Symbiodinium–MP2 hydrogel scaffolds indicated that silk microparticles loaded with curcumin were the most promising candidates for protecting algae from light stress during a bleaching event. Based on this, a new 3D bioprinted Symbiodinium–MP2 hydrogel scaffold was developed to simulate a bleaching scenario within the incubator. Both positive and negative controls were included: the positive control consisted of

Symbiodinium hydrogel scaffolds maintained under normal conditions (25°C and 100 PAR) for the entire experiment, while the negative control comprised Symbiodinium hydrogel scaffolds exposed to elevated temperatures to simulate bleaching.

To assess the potential protective effect of MP2 on algal photosystem II during the simulated bleaching, effective quantum yield Y(II) was measured using Diving-PAM instruments. This setup allowed continuous monitoring without interfering with light or temperature conditions in the incubator. Measurements were collected daily (**Figure 4.14A**). Positive control scaffolds maintained stable Y(II) values throughout the experiment (~0.7 ± 0.02). In contrast, Y(II) values in both the negative control and Symbiodinium–MP2 hydrogel scaffolds decreased as temperature increased, reaching minimum values of ~0.11 ± 0.03 and ~0.22 ± 0.03, respectively, after 10 hours at 31°C. Notably, the MP2-treated scaffolds consistently exhibited higher Y(II) values than the negative control, suggesting a partial protective effect against thermal and light stress.

4.3.9 *In vivo* Reactive Oxygen Species (ROS) scavenging assay

In parallel with Diving-PAM measurements, Amplex™ Red Hydrogen Peroxide/Peroxidase assays were performed daily on all samples, including the H_2O_2 control. Results are shown in **Figure 4.14B.** No H_2O_2 production was detected in any sample before day 5, when the temperature reached the peak of 31°C. After 7 hours of exposure, measurable H_2O_2 levels were observed, with ~0.70 ± 0.07 µmol in Symbiodinium hydrogel scaffolds without MP2 and ~0.15 ± 0.05 µmol in Symbiodinium–MP2 hydrogel scaffolds. After 10 hours, the highest H_2O_2 concentrations were recorded, reaching ~1.05 ± 0.05 µmol and ~0.40 ± 0.03 µmol, respectively. Beyond this point, both Y(II) and H_2O_2 were no longer detectable, suggesting that the algae were likely no longer viable.

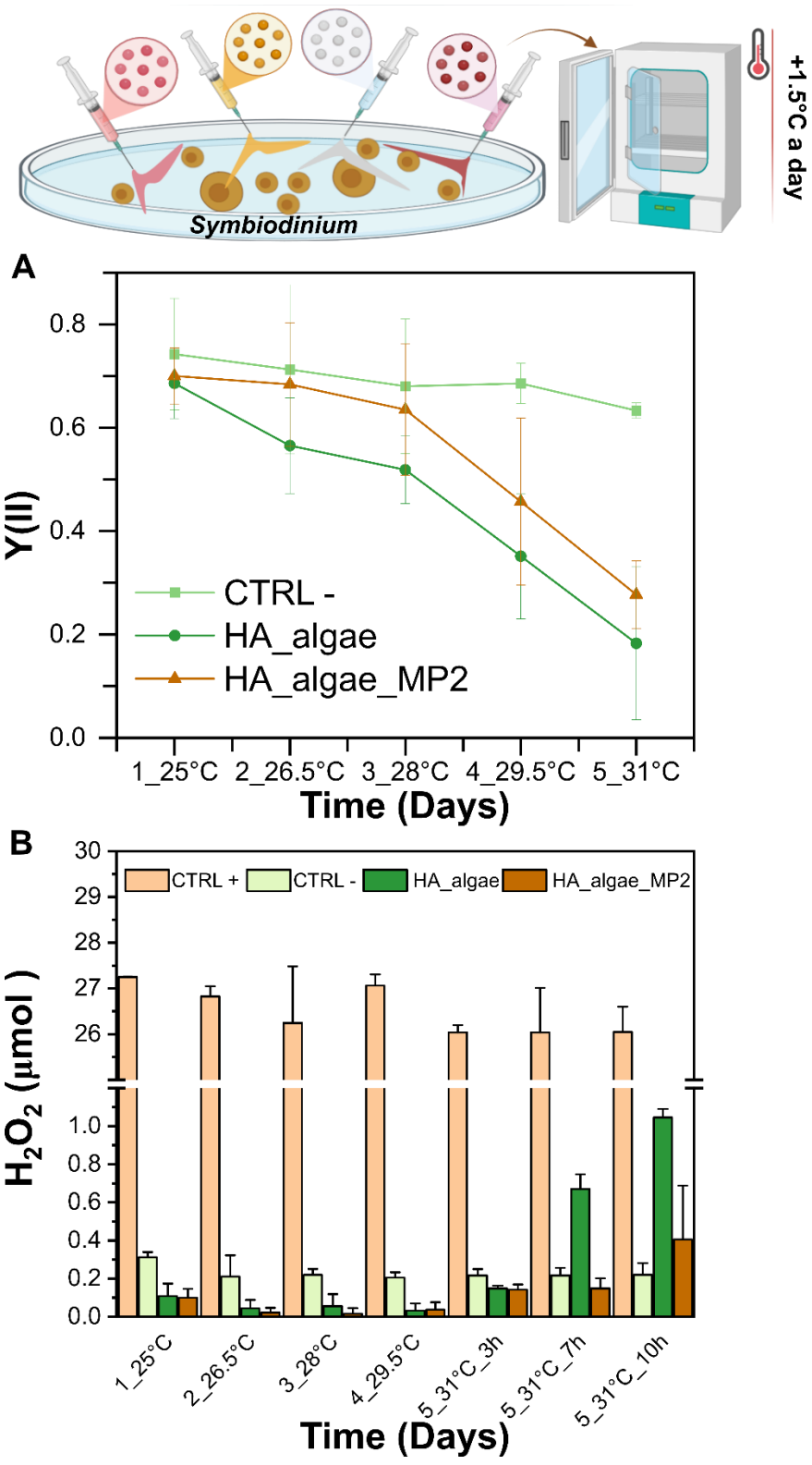
Symbiodinium
+1.5°C a day
A
Y(II)
0.0
0.2
0.4
0.6
0.8
CTRL -
HA_algae
HA_algae_MP2
1_25°C
2_26.5°C
3_28°C
4_29.5°C
5_31°C
Time (Days)
B
H2O2 (µmol)
CTRL +
CTRL -
HA_algae
HA_algae_MP2
26
27
28
29
30
1.0
0.8
0.6
0.4
0.2
0.0
1_25°C
2_26.5°C
3_28°C
4_29.5°C
5_31°C_3h
5_31°C_7h
5_31°C_10h
Time (Days)

Figure 4.14 Diving PAM and in vivo ROS scavenging activity for empty and MP2-loaded Symbiodinium hydrogel scaffolds. **A)** Diving PAM results expressed as effective quantum yield Y(II) for Symbiodinium-hydrogel scaffolds with and without MP2 exposed to higher temperature and Symbiodinium-hydrogel scaffolds kept at normal conditions (CTRL+). **B)** *In vivo* Reactive Oxygen Species (ROS) scavenging activity of MP2 in Symbiodinium-hydrogel scaffolds exposed to higher temperatures compared to Symbiodinium-hydrogel scaffolds without MP2 exposed to higher temperatures; Symbiodinium-hydrogel scaffolds kept at normal conditions (CTRL-); and H2O2 from the Amplex™ Red Kit (CTRL+).

4.4 Discussion and conclusions

Spray-dried antioxidant microparticles (MPs) were successfully fabricated using different natural antioxidant compounds and polymeric carriers, and classified as MP1, MP2, MP3, and MP4.

All formulations displayed a rounded morphology and stable size (from ~3 to ~6 µm diameter), consistent with spray-drying outcomes, with minor variations depending on the raw materials employed. In the first phase of the study, the microparticles were tested on liquid cultures of *Breviolum psygmophylum*. Even at the highest concentration (100µg/mL), MPs promoted higher cellular growth, while no significant differences were observed in photosynthetic efficiency (Fv/Fm). Nevertheless, increases in chlorophyll *a* content and broader electron transport rate curves suggested an overall positive effect of MPs on algal ecophysiology.

These improvements likely come from the encapsulated antioxidants, which may act as supplemental nutrients, enhancing algal growth and resilience. *In vitro* assays further assessed the ROS-scavenging efficacy of both MPs and free antioxidants, supporting their potential application as anti-bleaching agents.

When encapsulated within hyaluronic acid hydrogel scaffolds, Symbiodiniaceae showed accelerated growth even without MPs' presence, confirming the hydrogel's biocompatibility.

Anyway, when encapsulated with MP2, algae exhibited rapid recovery even after 24 hours post-3D-bioprinting and light exposure. This protective effect of curcumin-loaded silk MPs was further validated *in vivo*, where ROS production was significantly higher in controls compared to MP2-Symbiodinium-hydrogel scaffolds exposed to increasing temperatures. Beyond bleaching mitigation, this strategy points toward the possibility of engineering Symbiodiniaceae with natural bioactive compounds to enhance their resilience. Antioxidants thus appear to function not only as ROS scavengers but also as metabolic supplements, strengthening algal growth and stress tolerance.

In conclusion, spray-dried antioxidant MPs encapsulated within hyaluronic acid hydrogel scaffolds provide a scalable, low-cost drug delivery system capable of controlled release. This platform offers potential as both a preventive tool during heat-wave preparation and a first-aid solution for engineered algal reimplantation during bleaching events, making a significant step toward innovative and sustainable coral conservation strategies.

Chapter 5: Conclusions

5.1 Contribution of this thesis

As initially aimed, an effective drug delivery system for the treatment and/or prevention of coral bleaching was developed using approaches and materials that were as natural as possible, both in composition and technique. The use of eco-friendly and low-cost raw materials made all the technologies presented 100% biodegradable and environmentally compatible with the marine ecosystem. Furthermore, the confirmed biocompatibility with corals represents a key feature of the proposed systems, making them ideal candidates for coral reef treatment in the context of climate change.

The first two projects – the underwater three-layered film system and the protein-based microparticles for corals – provided significant results regarding the use of various polymers as matrices to ensure a continuous and controlled drug release over time. These systems demonstrated tangible benefits for corals, as evidenced by the *in vivo* coral bleaching simulation conducted at the Genoa Aquarium. Both components were highly effective in enhancing coral tolerance to heat stress. The molecular effects of curcumin on the enzymatic system, chlorophyll content, and zooxanthellae density were critical in preventing bleaching in treated corals compared to controls.

Moreover, the ease of administration of the microparticles, the practical handling of the underwater film system, and their stability underwater make these systems ideal prototypes for coral treatment in various contexts, from closed aquarium systems to open ocean environments.

These outcomes were instrumental in integrating the components into a single, effective drug delivery system, achieved in project 3. In this phase, microparticles were efficiently encapsulated within a hydrogel matrix, allowing even more precise control over drug release. When placed in direct contact with coral symbiodiniaceae, the microparticles significantly improved the ecophysiological condition of zooxanthellae, offering a potential preventive measure and an

effective post-bleaching therapy. Additionally, using different polymers and diverse natural antioxidant compounds demonstrated the system's adaptability to specific needs, further enhancing its value in coral reef restoration efforts. Techniques such as spray drying and 3D bioprinting proved the feasibility of scalable manufacturing methods, strengthening the balance between cost-effectiveness and performance.

Finally, *in vivo* tests conducted on both *Breviolum psygmophilum* Symbiodiniaceae and *Stylophora pistillata* corals using all developed technologies were essential in validating the original hypothesis of this PhD project: to develop advanced sustainable materials to protect and heal reefs from coral bleaching events.

Aligned with the United Nations Sustainable Development Goals (SDGs) of the 2030 Agenda, all the presented techniques directly contributed to at least three goals: SDG 6 (Clean water and Sanitation), SDG 12 (Responsible Consumption and Production), and SDG 14 (Life Below Water), representing timely and impactful solutions for sustainability-driven initiatives.

5.2 List of conferences, activities, and publications

List of Publications

1. Zych, A., Contardi, M., **Rinaldi, C.**, Scribano, V., Isa, V., Kossyvaki, D., ... & Montano, S. (2024). Underwater Quick-Hardening Vegetable Oil-Based Biodegradable Putty for Sustainable Coral Reef Restoration and Rehabilitation. *Advanced Sustainable Systems*, *8*(9), 2400110.

   Abstract:

   A new biodegradable epoxidized soybean oil acrylate (ESOA)/zein-based coral putty has been developed as an eco-friendly alternative to commercial concrete for the transplantation of new coral colonies in the reef.

2. Viola, F. A., Maksimovic, K., Cataldi, P., **Rinaldi, C.**, Stucchi, E., Melloni, F., ... & Caironi, M. (2024). All-organic transistors printed on a biodegradable and bioderived substrate for sustainable bioelectronics. *Materials Today Bio*, *29*, 101274.

   Abstract:

   The use of biopolymers such as polyhydroxybutyrate (PHB) as sustainable substrates for all-organic field effect transistors (OFETs) is here investigated as a solution for eco-friendly printed bioelectronics. Based on results, these biodegradable devices offer potential applications in biomedical and food packaging sectors, addressing the growing problem of electronic waste.

3. Trojanowska, D. J., Zych, A., Sganga, S., Tirelli, N., Boventi, M., **Rinaldi, C.**, ... & Perotto, G. (2025). Upgrading keratin into a moldable bioplastic. *Matter*, *8*(4).

Abstract:

This study introduces a sustainable method to create hard, flexible, and moldable bioplastics from keratin-rich wool waste by chemically modifying keratin through a thiol-based Michael-type addition. This approach highlights the potential of reprogrammed proteins as eco-friendly alternatives to conventional plastics.

4. Scribano, V., Contardi, M., **Rinaldi, C.**, Isa, V., Fiorentini, F., Ceseracciu, L., ... & Athanassiou, A. (2025). Eco-friendly active film and sealant for underwater drug delivery to diseased corals. *One Earth*, *8*(7).

   Abstract:

   An eco-friendly underwater drug-delivery system to treat bacterial infections in corals is proposed here. By combining a hydrophilic antibiotic film with a hydrophobic bio-based sealant, this system delivers antibiotics directly to coral tissue, marking a significant advance in managing coral disease outbreaks and protecting reef ecosystems.

5. Corigliano, G., Isa, V., Annese, V. F., **Rinaldi, C.**, Summa, M., Bertorelli, R., ... & Athanassiou, A. (2025). Active Biopaste for Coral Reef Restoration. *Advanced Materials*, 2502078.

   Abstract:

   The bio-based, conductive bicomponent paste described here is designed for coral transplantation and anchoring, supporting mineral accretion technology (MAT) to significantly accelerate coral growth. Its stable electrical properties and eco-friendly composition make it a versatile and sustainable alternative for coral restoration in both aquaria and natural reefs.

6. Hamed, S., Ibba, P., Altana, A., **Rinaldi, C.**, Lugli, P., Petti, L., ... & Cataldi, P. (2025). Plant-Based Electrodes for Bioimpedance Readings of Fruit. *Advanced Electronic Materials*, e00109.

   Abstract:

   This study develops sustainable electronic conductors by transforming tomato plant waste into biodegradable, conductive materials through integration with graphene nanoplatelets in bio-based latex matrices. These materials show promise as eco-friendly electrodes for bioimpedance sensing, offering a circular economy solution to reduce both electronic and agricultural waste.

7. Fadda, M., Lenzuni, M., Contardi, M., Brovero, F., **Rinaldi, C.**, Scribano, V., ... & Athanassiou, A. (2025). Biocompatible and Biodegradable Plant-Based Burn Dressings: A Sustainable Approach for Skin Regeneration. *ACS Sustainable Chemistry & Engineering*.

   Abstract:

   This study introduces sustainable skin burn dressings made from naturally derived materials like zein, lignin, and PVP, incorporating the antioxidant rutin for therapeutic benefits. By combining environmental sustainability with medical performance, this work advances eco-friendly solutions aligned with UN Sustainable Development Goals for burn care.

8. **Rinaldi, C.**, Contardi, M., Perotto, G., Scribano, V., Ravelli, L., Isa, V., …& Athanassiou, A. Engineering Silk Microparticles in Coral Bleaching Treatment: Bioinspired Underwater Vehicles for Curcumin Delivery. Under Review on *One Earth*.

   Abstract:

   This study explores the use of curcumin-loaded silk-based microparticles (cur-silk MPs) to protect corals from thermal stress caused by climate change. The microparticles effectively

deliver curcumin into corals, offering a targeted, biocompatible, promising therapy to mitigate coral bleaching and support reef health.

9. **Rinaldi, C.**, Contardi, M., Isa, V., Corigliano, C., Ravelli, L., Scribano, V., …& Athanassiou, A. Directional and Tunable Underwater Release of Curcumin Through a Three-layered Film System to Enhance Thermal Stress Resistance in Corals. Submitted to *Advanced Materials*.

   Abstract:

   This study introduces a sustainable, biocompatible three-layered film for controlled underwater delivery of curcumin to corals, aimed at reducing thermal stress-induced bleaching. The film releases antioxidant curcumin gradually through a nanocarrier system, effectively improving coral health. This easy-to-apply system shows promise for scalable coral conservation in both aquaria and natural reef settings.

Conferences and Poster Sessions:

Poster Session, October 10th, 2023, SC3 Science for Climate Change Challenges. Poster Title: "*Silk Microparticles in Coral Bleaching Treatment: Vehicles for Curcumin Delivery*".

Poster Session, November 30th, 2023, 25th anniversary of the University of Milano-Bicocca: Visions of the Future. Poster Title: "*Silk Microparticles in Coral Bleaching Treatment: Vehicles for Curcumin Delivery".*

Conference - Oral Presentation, July 2nd - 5th, 2024, European Coral Reef Symposium ECRS. Presentation Title: "*Biodegradable Underwater Films and Silk Microparticles as Vehicles for Curcumin Delivery in Coral Bleaching Treatment*".

Summer School MAF-WORLD COST – **Oral Presentation**, September 18th 2025. Presentation Title: "Engineering Silk Microparticles in Coral Bleaching Treatment: Bioinspired Underwater Vehicles for Curcumin Delivery".

Disciplinary Courses (TOT 8 CFU):

Title: "**New Materials and Technologies Applicable in the Marine Environment**"; Lecturer: Marco Contardi; Academic Year: 2022/2023; 1 CFU.

Title: "**Maritime Space and Globalization: Economic and Environmental Questions**"; Lecturer: Giulio Mellinato; Academic Year: 2022/2023; 2 CFU.

Title: "**Technologies for the Analysis of Contamination in the Marine Environment**"; Lecturer: Francesco Saliu; Academic Year: 2022/2023; 1 CFU

Title: "**Ecology of Tropical Marine Fish**"; Lecturer: Davide Seveso; Academic Year: 2022/2023; 1 CFU.

Title: "**Network Analysis for Ecologists**"; Lecturer: Giovanni Strona; Academic Year: 2022/2023; 2 CFU.

Title: "**Polar Questions and the Law of the Sea**"; Lecturer: Ilaria Tani; Academic Year: 2022/2023; 1 CFU.

Interdisciplinary Courses (TOT 3 CFU):

Title: "**Basic of Biobased Processes and Biorefineries**"; Lecturer: Paola Branduardi; Academic Year: 2022/2023; 1 CFU.

Title: "**Cultural Aspects of the Climate Crisis: Meanings, Denials, and Desires of Environmental Relatedness**"; Lecturer: Mauro Van Aken; Academic Year: 2022/2023; 1 CFU.

Title: "**Surfing the Academic Job Market: How to Publish in High Impact International Journals**", Lecturer: Marco Brambilla; Academic Year: 2022/2023; 1 CFU.

Third Mission – Communication Activities (TOT 40h):

Event "**Ocean Film Festival**"; November 26th, 2022; 6 hours.

Event "**IIT for the Schools**" – Elementary School LeMarcelline; May 26th, 2023; 8 hours.

Event "**IIT Family and Friends**"; June 21st, 2023; 8 hours.

Event "**OrientaMenti Genova**"; November 17th, 2023; 6 hours.

Event "**IIT for the Schools**" – Elementary School Brignole Sale; December 19th, 2023; 8 hours.

Event "**Open Day IIT**"; December 20th, 2023; 8 hours.

Event "**IIT for the schools**" – Istituto Comprensivo Casella; February 23rd, 2024; 8 hours.

Event “**IIT for the schools**” – Richeri School; May 31st, 2024; 8 hours.

Event “**OrientaMenti LaSpezia**”; June 4th, 2024; 6 hours.

Event “**IIT Family & Friends**”; June 25th, 2024; 8 hours.

Extracurricular Activities:

Internal Placement at the Italian Institute of Technology (IIT) within the Communication Directorate – Project Title: “IIT goes social”; From January 2nd, 2024, to April 21st, 2024; Supervisors: Valentina Polini (head of social media manager) and Dr. Giuliano Greco (Director of Communication and External Relations IIT).

Workshop attendance: “How to Write a Scientific Paper”; Organizer: Ana Helena Dias Francesconi; March 27-28th, 2023.

Talent Show “FameLab: science in 3 minutes”; April 13th, 2023, and May 8th, 2024; twice awarded the 'Audience Award.

High Tech Entrepreneurship Program THE GeNiUS – 2024 Edition; University of Genova – Université Cote d’Azur – Fondazione Istituto Italiano di Tecnologia; February 2nd – April 19th, 2024; 3rd place winner at the Pitch Competition.

Mobility Program:

SCRIPPS Institution of Oceanography – University of San Diego, California; period abroad from January 15th, 2025, to July 15th, 2025; Coral Reef Ecophysiology & Engineering Group; Supervisor: Dr. Daniel Wangpraseurt.

5.3 Recommendations for future work

The following recommendations are suggested for future research to further evaluate and optimize the drug delivery systems proposed in this thesis for coral bleaching prevention and treatment.

The underwater three-layered film system, together with the protein-based microparticles, could be further customized and tested under real environmental conditions, followed by long-term monitoring to assess their stability, efficacy, and ecological impact.

In addition, more scalable fabrication approaches could be explored for future material production, such as the use of extruders or other industrial and processing machinery.

Finally, the 3D bioprinted hydrogel scaffolds containing both microparticles and microalgae could be investigated as post-bleaching therapeutic systems. The presence of microparticles appeared to enhance the overall ecophysiology of the microalgae, resulting in engineered *Symbiodiniaceae* with higher thermal tolerance. Since coral bleaching ultimately leads to the loss of zooxanthellae, providing this bioengineered tool could promote a faster reacquisition of symbiotic microalgae, thereby supporting the recovery of the entire coral organism.

References

1. Sobha, T. R., Vibija, C. P. & Fahima, P. Coral Reef: A Hot Spot of Marine Biodiversity. in *Conservation and Sustainable Utilization of Bioresources* 171–194 (Springer Nature, 2023). doi:10.1007/978-981-19-5841-0_8.
2. Connell, J. H. Diversity in Tropical Rain Forests and Coral Reefs. *Science* **199**, 1302–1310 (1978).
3. Terry P. Hughes *et al.* Coral reefs in the Anthropocene. *Nature* **546**, 82–90 (2017).
4. Costanza, R. *et al.* Changes in the global value of ecosystem services. *Glob. Environ. Change* **26**, 152–158 (2014).
5. Eddy, T. D. *et al.* Global decline in capacity of coral reefs to provide ecosystem services. *One Earth* **4**, 1278–1285 (2021).
6. Sheppard, C., Davy, S., Pilling, G. & Graham, N. *The Biology of Coral Reefs*. (Oxford University Press, 2017). doi:10.1093/oso/9780198787341.001.0001.
7. LaJeunesse, T. C. *et al.* Systematic Revision of Symbiodiniaceae Highlights the Antiquity and Diversity of Coral Endosymbionts. *Curr. Biol.* **28**, 2570-2580.e6 (2018).
8. Muller-Parker, G., D'Elia, C. F. & Cook, C. B. Interactions Between Corals and Their Symbiotic Algae. in *Coral Reefs in the Anthropocene* (ed. Birkeland, C.) 99–116 (Springer Netherlands, Dordrecht, 2015). doi:10.1007/978-94-017-7249-5_5.
9. Barlow, J. *et al.* The future of hyperdiverse tropical ecosystems. *Nature* **559**, 517–526 (2018).

10. Baker, A. C., Glynn, P. W. & Riegl, B. Climate change and coral reef bleaching: An ecological assessment of long-term impacts, recovery trends and future outlook. *Estuar. Coast. Shelf Sci.* **80**, 435–471 (2008).
11. Phinney, J. T. *Coral Reefs and Climate Change: Science and Management*. (American Geophysical Union, 2006).
12. Spalding, M., Ravilious, C. & Green, E. P. *World Atlas of Coral Reefs*. (University of California Press, 2001).
13. Riegl, B., Bruckner, A., Coles, S. L., Renaud, P. & Dodge, R. E. Coral Reefs. *Ann. N. Y. Acad. Sci.* **1162**, 136–186 (2009).
14. Sun, H. *et al.* New insights into microbial and metabolite signatures of coral bleaching. *Sci. Total Environ.* **892**, 164258 (2023).
15. Brandt, M. E. & McManus, J. W. Disease incidence is related to bleaching extent in reef-building corals. *Ecology* **90**, 2859–2867 (2009).
16. Comte, A. & Pendleton, L. H. Management strategies for coral reefs and people under global environmental change: 25 years of scientific research. *J. Environ. Manage.* **209**, 462–474 (2018).
17. Davy SK, Allemand D, Weis VM. Cell Biology of Cnidarian-Dinoflagellate Symbiosis. *Cell Biol. Cnidarian-Dinoflag. Symbiosis* **Microbiol Mol Biol Rev 76**, (2012).
18. Weis, V. M. Cellular mechanisms of Cnidarian bleaching: stress causes the collapse of symbiosis. *J. Exp. Biol.* **211**, 3059–3066 (2008).

19. Lesser, M. P. Coral Bleaching: Causes and Mechanisms. in *Coral Reefs: An Ecosystem in Transition* (eds Dubinsky, Z. & Stambler, N.) 405–419 (Springer Netherlands, Dordrecht, 2011). doi:10.1007/978-94-007-0114-4_23.

20. Hoegh-Guldberg, O. Climate change, coral bleaching and the future of the world's coral reefs. *Mar. Freshw. Res.* **50**, 839–866 (1999).

21. Houlbrèque, F. & Ferrier-Pagès, C. Heterotrophy in Tropical Scleractinian Corals. *Biol. Rev.* **84**, 1–17 (2009).

22. Oakley, C. A. & Davy, S. K. Cell Biology of Coral Bleaching. in *Coral Bleaching: Patterns, Processes, Causes and Consequences* (eds van Oppen, M. J. H. & Lough, J. M.) 189–211 (Springer International Publishing, Cham, 2018). doi:10.1007/978-3-319-75393-5_8.

23. Fabricius, K. Coral Reefs: An Ecosystem in Transition. in 493–505 (2011). doi:10.1007/978-94-007-0114-4_28.

24. Triggers, cascades, and endpoints: connecting the dots of coral bleaching mechanisms - Helgoe - 2024 - Biological Reviews - Wiley Online Library. https://onlinelibrary.wiley.com/doi/10.1111/brv.13042.

25. Downs, C. A. *et al.* Oxidative stress and seasonal coral bleaching. *Free Radic. Biol. Med.* **33**, 533–543 (2002).

26. Nielsen, D. A., Petrou, K. & Gates, R. D. Coral bleaching from a single cell perspective. *ISME J.* **12**, 1558–1567 (2018).

27. van Oppen, M. J. H. & Lough, J. M. Synthesis: Coral Bleaching: Patterns, Processes, Causes and Consequences. in *Coral Bleaching: Patterns, Processes, Causes and*

Consequences (eds van Oppen, M. J. H. & Lough, J. M.) 343–348 (Springer International Publishing, Cham, 2018). doi:10.1007/978-3-319-75393-5_14.

28. Nielsen, D. A. & Petrou, K. Lipid stores reveal the state of the coral-algae symbiosis at the single-cell level. *ISME Commun.* **3**, 29 (2023).
29. Reimer, J. D. *et al.* The Fourth Global Coral Bleaching Event: Where do we go from here? *Coral Reefs* **43**, 1121–1125 (2024).
30. National Oceanic and Atmospheric Administration. NOAA Confirms 4th Global Coral Bleaching Event. *National Oceanic and Atmospheric Administration* https://www.noaa.gov/news-release/noaa-confirms-4th-global-coral-bleaching-event (2024).
31. Sully, S., Hodgson, G. & van Woesik, R. Present and future bright and dark spots for coral reefs through climate change. *Glob. Change Biol.* **28**, 4509–4522 (2022).
32. Donner, S. D., Heron, S. F. & Skirving, W. J. Future Scenarios: a Review of Modelling Efforts to Predict the Future of Coral Reefs in an Era of Climate Change. in *Coral Bleaching: Patterns, Processes, Causes and Consequences* (eds van Oppen, M. J. H. & Lough, J. M.) 159–173 (Springer, Berlin, Heidelberg, 2009). doi:10.1007/978-3-540-69775-6_10.
33. Latham, J., Kleypas, J., Hauser, R., Parkes, B. & Gadian, A. Can marine cloud brightening reduce coral bleaching? *Atmospheric Sci. Lett.* **14**, 214–219 (2013).
34. Peixoto, R. S. *et al.* The critical role of coral reef restoration in a changing world. *Nat. Clim. Change* **14**, 1219–1222 (2024).

35. Bayraktarov, E. *et al.* Motivations, success, and cost of coral reef restoration. *Restor. Ecol.* **27**, 981–991 (2019).

36. Boström-Einarsson, L. *et al.* Coral restoration - A systematic review of current methods, successes, failures and future directions. *PloS One* **15**, e0226631 (2020).

37. Wangpraseurt, D. *et al.* Bioprinted Living Coral Microenvironments Mimicking Coral-Algal Symbiosis. *Adv. Funct. Mater.* **32**, 2202273 (2022).

38. Zych, A. *et al.* Underwater Quick-Hardening Vegetable Oil-Based Biodegradable Putty for Sustainable Coral Reef Restoration and Rehabilitation. *Adv. Sustain. Syst.* **8**, 2400110 (2024).

39. Scribano, V. *et al.* Eco-friendly active film and sealant for underwater drug delivery to diseased corals. *One Earth* **8**, 101356 (2025).

40. Corigliano, G. *et al.* Active Biopaste for Coral Reef Restoration. *Adv. Mater.* **37**, 2502078 (2025).

41. Santoro, E. P. *et al.* Coral microbiome manipulation elicits metabolic and genetic restructuring to mitigate heat stress and evade mortality. *Sci. Adv.* **7**, eabg3088 (2021).

42. Montalbetti, E. *et al.* Manganese Benefits Heat-Stressed Corals at the Cellular Level. *Front. Mar. Sci.* **8**, (2021).

43. Moreira, G. R. M. *et al.* Enhancing coral photosynthesis: The power of manganese-alginate gels. *J. Trace Elem. Med. Biol.* **89**, 127675 (2025).

44. Adepu, S. & Ramakrishna, S. Controlled Drug Delivery Systems: Current Status and Future Directions. *Molecules* **26**, 5905 (2021).

45. Roger, L. M., Russo, J. A., Jinkerson, R. E., Giraldo, J. P. & Lewinski, N. A. Engineered nanoceria alleviates thermally induced oxidative stress in free-living Breviolum minutum (Symbiodiniaceae, formerly Clade B). *Front. Mar. Sci.* **9**, (2022).

46. Contardi, M. *et al.* Biodegradable Zein-Based Biocomposite Films for Underwater Delivery of Curcumin Reduce Thermal Stress Effects in Corals. *ACS Appl. Mater. Interfaces* **15**, 33916–33931 (2023).

47. Nardo, L., Andreoni, A., Bondani, M., Másson, M. & Hjorth Tønnesen, H. Studies on curcumin and curcuminoids. XXXIV. Photophysical properties of a symmetrical, non-substituted curcumin analogue. *J. Photochem. Photobiol. B* **97**, 77–86 (2009).

48. Kaur, K., Al-Khazaleh, A. K., Bhuyan, D. J., Li, F. & Li, C. G. A Review of Recent Curcumin Analogues and Their Antioxidant, Anti-Inflammatory, and Anticancer Activities. *Antioxidants* **13**, 1092 (2024).

49. dos Santos, V. L. S. *et al.* Layer-by-layer assembly: A versatile approach for tailored biomedical films and drug delivery. *J. Drug Deliv. Sci. Technol.* **91**, 105243 (2024).

50. He, M., Zhu, L., Yang, N., Li, H. & Yang, Q. Recent advances of oral film as platform for drug delivery. *Int. J. Pharm.* **604**, 120759 (2021).

51. Li, L., Ni, R., Shao, Y. & Mao, S. Carrageenan and its applications in drug delivery. *Carbohydr. Polym.* **103**, 1–11 (2014).

52. Ngouémazong, E. D., Christiaens, S., Shpigelman, A., Van Loey, A. & Hendrickx, M. The Emulsifying and Emulsion-Stabilizing Properties of Pectin: A Review. *Compr. Rev. Food Sci. Food Saf.* **14**, 705–718 (2015).

53. Muxika, A., Etxabide, A., Uranga, J., Guerrero, P. & de la Caba, K. Chitosan as a bioactive polymer: Processing, properties and applications. *Int. J. Biol. Macromol.* **105**, 1358–1368 (2017).

54. Tortorella, S. *et al.* Zein as a versatile biopolymer: different shapes for different biomedical applications. *RSC Adv.* **11**, 39004–39026 (2021).

55. Jahed, V., Zarrabi, A., Bordbar, A. & Hafezi, M. S. NMR (1H, ROESY) spectroscopic and molecular modelling investigations of supramolecular complex of β-cyclodextrin and curcumin. *Food Chem.* **165**, 241–246 (2014).

56. Jiang, L. *et al.* Preparation and characterization of curcumin/β-cyclodextrin nanoparticles by nanoprecipitation to improve the stability and bioavailability of curcumin. *LWT* **171**, 114149 (2022).

57. Martínez-Guerra, J. *et al.* On the Curcumin and β-Cyclodextrin Interaction in Aqueous Media. Spectrophotometric and Electrochemical Study. *ChemElectroChem* **9**, e202101534 (2022).

58. La Notte, L. *et al.* Fully-sprayed flexible polymer solar cells with a cellulose-graphene electrode. *Mater. Today Energy* **7**, 105–112 (2018).

59. La Notte, L. *et al.* Sprayed organic photovoltaic cells and mini-modules based on chemical vapor deposited graphene as transparent conductive electrode. *Carbon* **129**, 878–883 (2018).

60. Fadda, M. *et al.* Antioxidant coatings from elastomeric vinyl acetate-vinyl laurate copolymers with reduced bacterial adhesion. *Prog. Org. Coat.* **168**, 106883 (2022).

61. Voolstra, C. R. *et al*. Standardized short-term acute heat stress assays resolve historical differences in coral thermotolerance across microhabitat reef sites. *Glob. Change Biol.* **26**, 4328–4343 (2020).

62. Jeffrey, S. W. & Humphrey, G. F. New spectrophotometric equations for determining chlorophylls *a*, *b*, *c*1 and *c*2 in higher plants, algae and natural phytoplankton. *Biochem. Physiol. Pflanz.* **167**, 191–194 (1975).

63. Veal, C., Carmi, M., Fine, M. & Hoegh-Guldberg, O. Increasing the accuracy of surface area estimation using single wax dipping of coral fragments. *Coral Reefs* **29**, (2010).

64. Isa, V. *et al*. Physical and cellular impact of environmentally relevant microplastic exposure on thermally challenged *Pocillopora damicornis* (Cnidaria, Scleractinia). *Sci. Total Environ.* **918**, 170651 (2024).

65. Louis, Y. *et al*. In hospite Symbiodinium photophysiology and antioxidant responses in Acropora muricata on a coast-reef scale: implications for variable bleaching patterns. *Symbiosis* **68**, (2016).

66. Vance, P. G., Keele, B. B. & Rajagopalan, K. V. Superoxide dismutase from Streptococcus mutans. Isolation and characterization of two forms of the enzyme. *J. Biol. Chem.* **247**, 4782–4786 (1972).

67. Bergmeyer, H.U. Methods of Enzymatic Analysis. *ScienceDirect* https://www.sciencedirect.com/book/9780123956309/methods-of-enzymatic-analysis (1974).

68. Aebi, H. Catalase in vitro. in *Methods in Enzymology* vol. 105 121–126 (Academic Press, 1984).

69. Hayes, J. D. & Strange, R. C. Glutathione S-transferase polymorphisms and their biological consequences. *Pharmacology* **61**, 154–166 (2000).

70. Wang, Y., Oberley, L. W. & Murhammer, D. W. Antioxidant defense systems of two lipidopteran insect cell lines. *Free Radic. Biol. Med.* **30**, 1254–1262 (2001).

71. Gérard-Monnier, D. *et al.* Reactions of 1-methyl-2-phenylindole with malondialdehyde and 4-hydroxyalkenals. Analytical applications to a colorimetric assay of lipid peroxidation. *Chem. Res. Toxicol.* **11**, 1176–1183 (1998).

72. Prado-Fernández, J., Rodríguez-Vázquez, J. A., Tojo, E. & Andrade, J. M. Quantitation of κ-, ι- and λ-carrageenans by mid-infrared spectroscopy and PLS regression. *Anal. Chim. Acta* **480**, 23–37 (2003).

73. Güzel, M. & Akpınar, Ö. Valorisation of fruit by-products: Production characterization of pectins from fruit peels. *Food Bioprod. Process.* **115**, 126–133 (2019).

74. Mireles, L. K., Wu, M.-R., Saadeh, N., Yahia, L. & Sacher, E. Physicochemical Characterization of Polyvinyl Pyrrolidone: A Tale of Two Polyvinyl Pyrrolidones. *ACS Omega* **5**, 30461–30467 (2020).

75. Kolev, T. M., Velcheva, E. A., Stamboliyska, B. A. & Spiteller, M. DFT and experimental studies of the structure and vibrational spectra of curcumin. *Int. J. Quantum Chem.* **102**, 1069–1079 (2005).

76. Nikolic, V. *et al.* Photostability of piroxicam in the inclusion complex with 2-hydroxypropyl-β-cyclodextrin. *Hem. Ind.* **68**, 107–116 (2014).

77. Demir, D., Öfkeli, F., Ceylan, S. & Bölgen, N. Extraction and Characterization of Chitin and Chitosan from Blue Crab and Synthesis of Chitosan Cryogel Scaffolds. *J. Turk. Chem. Soc. Sect. Chem.* **3**, (2016).

78. Corradini, E. *et al.* Recent advances in food-packing, pharmaceutical and biomedical applications of zein and zein-based materials. *Int. J. Mol. Sci.* **15**, 22438–22470 (2014).

79. Byler, D. M. & Susi, H. Examination of the secondary structure of proteins by deconvolved FTIR spectra. *Biopolymers* **25**, 469–487 (1986).

80. Navarra, G. *et al.* Heat- and pH-induced BSA conformational changes, hydrogel formation and application as 3D cell scaffold. *Arch. Biochem. Biophys.* **606**, 134–142 (2016).

81. Erickson, D. P. *et al.* Corn zein undergoes conformational changes to higher β-sheet content during its self-assembly in an increasingly hydrophilic solvent. *Int. J. Biol. Macromol.* **157**, 232–239 (2020).

82. Xie, F. Biopolymer-Based Multilayer Films and Coatings for Food Preservation: an Update of the Recent Development. *Curr. Food Sci. Technol. Rep.* **1**, 1–12 (2023).

83. Li, D., Wang, J., Guo, Z., Li, J. & Shuai, J. Pectin gels cross-linked by Ca2 +: An efficient material for methylene blue removal. *J. Mol. Liq.* **238**, 36–42 (2017).

84. Wurm, F., Rietzler, B., Pham, T. & Bechtold, T. Multivalent Ions as Reactive Crosslinkers for Biopolymers-A Review. *Mol. Basel Switz.* **25**, 1840 (2020).

85. Chaichi, M., Badii, F., Mohammadi, A. & Hashemi, M. Water resistance and mechanical properties of low methoxy-pectin nanocomposite film responses to

interactions of Ca2+ ions and glycerol concentrations as crosslinking agents. *Food Chem*. **293**, 429–437 (2019).

86. Keppeler, S., Ellis, A. & Jacquier, J. C. Cross-linked carrageenan beads for controlled release delivery systems. *Carbohydr. Polym*. **78**, 973–977 (2009).
87. Li, L., Zhao, J., Sun, Y., Yu, F. & Ma, J. Ionically cross-linked sodium alginate/κ-carrageenan double-network gel beads with low-swelling, enhanced mechanical properties, and excellent adsorption performance. *Chem. Eng. J.* **372**, 1091–1103 (2019).
88. Mohamadnia, Z., Zohuriaan-Mehr, M. J., Kabiri, K., Jamshidi, A. & Mobedi, H. Ionically cross-linked carrageenan-alginate hydrogel beads. *J. Biomater. Sci. Polym. Ed.* **19**, 47–59 (2008).
89. Cataldo, S., Crea, F., Gianguzza, A., Pettignano, A. & Piazzese, D. Solubility and acid-base properties and activity coefficients of chitosan in different ionic media and at different ionic strengths, at T = 25 °C. *J. Mol. Liq*. **148**, 120–126 (2009).
90. Miyaji, K. *et al*. Biodegradation of various forms of cellulose and chitin in natural waters with different salinity. *Polym. Degrad. Stab.* **215**, 110423 (2023).
91. Tsuji, H. & Suzuyoshi, K. Environmental degradation of biodegradable polyesters 1. Poly(ε-caprolactone), poly[(R)-3-hydroxybutyrate], and poly(L-lactide) films in controlled static seawater. *Polym. Degrad. Stab.* **75**, 347–355 (2002).
92. Lesser, M. P. Oxidative stress in marine environments: biochemistry and physiological ecology. *Annu. Rev. Physiol*. **68**, 253–278 (2006).

93. Downs, C. A., Mueller, E., Phillips, S., Fauth, J. E. & Woodley, C. M. A molecular biomarker system for assessing the health of coral (Montastraea faveolata) during heat stress. *Mar. Biotechnol. N. Y. N* **2**, 533–544 (2000).

94. Montalbetti, E. *et al.* Mucilage-induced necrosis reveals cellular oxidative stress in the Mediterranean gorgonian *Paramuricea clavata*. *J. Exp. Mar. Biol. Ecol.* **559**, 151839 (2023).

95. Seveso, D., Louis, Y. D., Bhagooli, R., Downs, C. A. & Dellisanti, W. Editorial: The cellular stress response and physiological adaptations of corals subjected to environmental stressors and pollutants, volume II. *Front. Physiol.* **15**, 1473792 (2024).

96. Titlyanov, E., Titlyanova, T., Yamazato, K. & Van Woesik, R. Photo-acclimation dynamics of the coral Stylophora pistillata to low and extremely low light. *J. Exp. Mar. Biol. Ecol. - J EXP MAR BIOL ECOL* **263**, 211–225 (2001).

97. Bhagooli, R. & Hidaka, M. Photoinhibition, bleaching susceptibility and mortality in two scleractinian corals, Platygyra ryukyuensis and Stylophora pistillata, in response to thermal and light stresses. *Comp. Biochem. Physiol. A. Mol. Integr. Physiol.* **137**, 547–555 (2004).

98. Levy, O. *et al.* Molecular assessment of the effect of light and heterotrophy in the scleractinian coral Stylophora pistillata. *Proc. R. Soc. B Biol. Sci.* **283**, 20153025 (2016).

99. Boström-Einarsson, L. *et al.* Coral restoration in a changing world.

100. Ding, D.-S., Sun, W.-T. & Pan, C.-H. Feeding of a Scleractinian Coral, Goniopora columna, on Microalgae, Yeast, and Artificial Feed in Captivity. *Animals* **11**, 3009 (2021).

101. Hii, Y.-S., Soo, C.-L. & Liew, H.-C. Feeding of scleractinian coral, Galaxea fascicularis, on Artemia salina nauplii in captivity. *Aquac. Int.* **17**, 363–376 (2009).

102. Tian, Z. *et al.* Silkworm Cocoon: Dual Functions as a Traditional Chinese Medicine and the Raw Material of Promising Biocompatible Carriers. *Pharmaceuticals* **17**, 817 (2024).

103. Afzal, O. *et al.* Nanoparticles in Drug Delivery: From History to Therapeutic Applications. *Nanomaterials* **12**, 4494 (2022).

104. Ezike, T. C. *et al.* Advances in drug delivery systems, challenges and future directions. *Heliyon* **9**, (2023).

105. Pignatelli, C. *et al.* Electrospun silk fibroin fibers for storage and controlled release of human platelet lysate. *Acta Biomater.* **73**, 365–376 (2018).

106. Hu, X., Kaplan, D. & Cebe, P. Determining Beta Sheet Crystallinity in Fibrous Proteins by Thermal Analysis and Infrared Spectroscopy. *Macromolecules* **39**, 6161–6170 (2006).

107. Rockwood, D. N. *et al.* Materials fabrication from Bombyx mori silk fibroin. *Nat. Protoc.* **6**, 1612–1631 (2011).

108. Mitropoulos, A. N. *et al.* Synthesis of Silk Fibroin Micro- and Submicron Spheres Using a Co-Flow Capillary Device. *Adv. Mater.* **26**, 1105–1110 (2014).

109. Pham, D. T. & Tiyaboonchai, W. Fibroin nanoparticles: a promising drug delivery system. *Drug Deliv.* **27**, 431–448 (2020).

110. Drummy, L. F., Phillips, D. M., Stone, M. O., Farmer, B. L. & Naik, R. R. Thermally induced alpha-helix to beta-sheet transition in regenerated silk fibers and films. *Biomacromolecules* **6**, 3328–3333 (2005).

111. Borgert, C. J., Fuentes, C. & Burgoon, L. D. Principles of dose-setting in toxicology studies: the importance of kinetics for ensuring human safety. *Arch. Toxicol.* **95**, 3651–3664 (2021).

112. Siebeck, U., Logan, D. & Marshall, N. CoralWatch – a flexible coral bleaching monitoring tool for you and your group. *Proc. 11th Int. Coral Reef Symp.* **1**, (2008).

113. Ji, Y. *et al.* DFT-Calculated IR Spectrum Amide I, II, and III Band Contributions of *N* -Methylacetamide Fine Components. *ACS Omega* **5**, 8572–8578 (2020).

114. Kossyvaki, D. *et al.* Highly Porous Curcumin-Loaded Polymer Mats for Rapid Detection of Volatile Amines. *ACS Appl. Polym. Mater.* **4**, 4464–4475 (2022).

115. Montalbetti, E. *et al.* Short-term microplastic exposure triggers cellular damage through oxidative stress in the soft coral Coelogorgia palmosa. *Mar. Biol. Res.* **18**, 1–14 (2022).

116. Emanet, M. *et al.* Sumac (Rhus coriaria) Extract-Loaded Polymeric Nanosheets Efficiently Protect Human Dermal Fibroblasts from Oxidative Stress. *ACS Appl. Bio Mater.* **5**, 5901–5910 (2022).

117. Manda-Hakki, K. & Hassanpour, H. Effect of L-glutathione treatment on biochemical properties, antioxidant capacity and antioxidant enzymes activity in strawberry fruits during storage. *Heliyon* **10**, (2024).

118. Bayer, G., Shayganpour, A., Zia, J. & Bayer, I. S. Polyvinyl alcohol-based films plasticized with an edible sweetened gel enriched with antioxidant carminic acid. *J. Food Eng.* **323**, 111000 (2022).

119. Boilard, A. *et al.* Defining Coral Bleaching as a Microbial Dysbiosis within the Coral Holobiont. *Microorganisms* **8**, 1682 (2020).

120. Wangpraseurt, D. *et al.* Bionic 3D printed corals. *Nat. Commun.* **11**, 1748 (2020).

121. Contardi, M. *et al.* Treatment of Coral Wounds by Combining an Antiseptic Bilayer Film and an Injectable Antioxidant Biopolymer. *Sci. Rep.* **10**, 988 (2020).

122. Yuwen Chen, Jiumeng Zhang, Xuan Liu, Shuai Wang, Jie Tao, Yulan Huang, Wenbi Wu, Yang Li, Kai Zhou, Xiawei Wei, Shaochen Chen, Xiang Li, Xuewen Xu, Ludwig Cardon, Zhiyong Qian, and Maling Gou. Noninvasive in vivo 3D bioprinting. https://www.science.org/doi/10.1126/sciadv.aba7406 (2020) doi:10.1126/sciadv.aba7406.

123. Kosaraju, S. L., D'ath, L. & Lawrence, A. Preparation and characterisation of chitosan microspheres for antioxidant delivery. *Carbohydr. Polym.* **64**, 163–167 (2006).

124. Tomoda, K. *et al.* Preparation and properties of carrageenan microspheres containing allopurinol and local anesthetic agents for the treatment of oral mucositis. *Colloids Surf. B Biointerfaces* **71**, 27–35 (2009).

125. Obaidat, R. M., Alnaief, M. & Mashaqbeh, H. Investigation of Carrageenan Aerogel Microparticles as a Potential Drug Carrier. *AAPS PharmSciTech* **19**, 2226–2236 (2018).

126. Petersen, L.-E. *et al.* Photodegradation of a bacterial pigment and resulting hydrogen peroxide release enable coral settlement. *Sci. Rep.* **13**, 3562 (2023).

127. Ozgur Karakuzu, Cruz, M. R., Liu, Y. & Garsin, D. A. Amplex Red Assay for Measuring Hydrogen Peroxide Production from Caenorhabditis elegans. *Bio-Protoc.* **9**, (2019).